Removal of fusion-relevant deposits from metallic surfaces using low-temperature plasmas

David Richard Shaw

Doctor of Philosophy

University of York

Physics

September 2018

Abstract

Optical diagnostics on fusion devices are important for both research and real time control. All of these diagnostics depend on reflective optics in the form of metallic mirrors. Etching and re-deposition during fusion operation from the beryllium inner wall onto the mirrors can cause severe degradation in the reflectivity. Using the mirror as the powered electrode to form a capacitively coupled plasma above the surface is seen as the most favourable method for recovery of the mirror reflectivity. The ions created within the plasma can bombard the surface and remove the deposit.

This method has been tested experimentally in various ways and in various geometries and has been proven to work in these cases. However, in order to optimise the system modelling efforts are carried out within this thesis. The Hybrid Plasma Equipment Model (HPEM) is configured to simulate the etching plasma and is benchmarked against experimental results. After successful benchmarking parameters are varied in an attempt to find optimum settings for the successful implementation of this method on ITER. Results concluding that individual mirrors require individual modelling efforts as trends cannot necessarily be applied to each mirror geometry.

A beryllium/argon/oxygen gas chemistry set is created to more accurately model the ITER environment which is compared with a published aluminium/argon/oxygen set. Aluminium is currently used as a proxy for beryllium in the majority of experimental work. They are shown to be dissimilar in their behaviour within a bulk Ar plasma which will have knock on effects for the etching process. The bulk plasma properties remain identical at low fractions of Be or Al.

Also presented is work involving understanding the mechanism behind modification of polypropylene using an atmospheric-pressure plasma jet. A two stage process is identified involving atomic oxygen from the jet and nitrogen from the surrounding atmosphere.

Contents

List of Tables

List of Figures

Acknowledgments

Although this thesis is a collection of work from only the last four years of my life, it also represents the completion of my 26 years in education. This final step could not have been completed without the support of so many people, some of whom are named here.

First I must thank Erik, my supervisor. I never saw myself doing a Ph.D and only applied for one on a whim, as everybody else on the MSc was doing it. After the interview Erik offered me the position and I've never looked back; it is with his guidance that I have made it to the end of this journey with something to show for it. Even though I was taken on as an experimentalist and had to be formed into a computational researcher, he trusted me to learn and get the job done. It is this trust, even when I was useless at showing up for weekly supervision meetings, that means the most.

Moving from experiment to modelling was a difficult transition, but it was made all the easier through the assistance of Mark Kushner and his group at the Univeristy of Michigan, especially Juliusz, who kept me entertained during my visit, alongside Aram and Steve.

Within the York Plasma Institute I must thank the admin staff, past and present: Ruth, Kathryn, Jenni, Donna, Laurie, and Jo. They've always been there to help and are ever supportive, even when it means more work for them! I must apologise for the number of times I have handed something in late; the number of random parcels I have had delivered; numerous claims forms I have failed to fill in properly; and for not reading the handbook before asking a question.

The people in closest proximity to me during this Ph.D have been those occupying the same office space. Thanks to the Chemistry Hub reprobates of Andy West, Andy Hurlbatt, Martin, Joe, Hannah, John, and Sudha who moved with me to the new extension. As some left I gained Helen, Dave Meehan, Josh, Fred, Bhavin, and Michael. Everybody who has shared an office with me over this period has had to endure my sense of humour; thanks for taking it in your stride. Thanks also go to Andrew Gibson and Sandra, who often visited the office for a coffee, only to be distracted for hours. Thanks to Scott for being in the same building as me for 5 years and improving my pun library immensely. Also thanks to Phil and Dave Blackman, without whom I would not have learnt such life lessons as how to break into a house with a screwdriver, or the endless possibilities of the Raspberry pi. There are

also plenty of Ph.D students, post-docs, and staff at the YPI, not named here, but without whom I would not have had such an amazing experience. No thanks go to John Pasley who has been a constant source of irritation.

I must then thank those people who looked after me in the lab. Rich for his endless patience, knowledge, and willingness to help me do things that were questionable and potentially not even related to my work. Kari for teaching more than I ever needed to know about so many things and going above and beyond in solving my problems. I must also thank Mark from the workshop at Ellis Patents Ltd for manufacturing parts for me in an hour that the physics department hadn't even started after 6 weeks.

Outside of the office I must thank my friends Alex, Jared, and Flo who have endured many evenings of Dungeons and Dragons, me complaining at the pub, or out on the archery range. These are the things that have kept me sane and will be what I miss most about York when we all go our separate ways. Having mentioned archery; the club at York has been my distraction from work for the past 4 years. The experience of being involved in such a wonderful club with such brilliant people will always be a happy memory for me. I am especially grateful to the coaching support from Mick and Kath Fitzpatrick, who helped the club get to where it is (top of the league) and helped me along the coaching journey.

Coming to the end of my acknowledgements I must penultimately thank Sarah. She has been with me through everything mentioned above and without her I could not have reached the end of this journey. I would never have taken up archery, I would never have made it into uni before 10:30 am, and my Northern Irish accent would not be as refined as it is. I just hope that I have made as much of a positive impact on her life as she has, and continues to have, on mine.

Finally the biggest thanks are to my parents; Richard and Gill. For the past 29 years these two people have helped me become the person I am today. They supported me through my early academic failings and pushed me to get where I wanted to be, always believing in me. Every good decision I have ever made can be traced back to advice I have received from them and as such it has been invaluable. They are simply amazing and cannot be thanked enough.

Declaration

This thesis has not previously been accepted for any degree and is not being concurrently submitted in candidature for any degree other than Doctor of Philosophy of the University of York. This thesis is the result of my own investigations, except where otherwise stated. All other sources are acknowledged by explicit references.

In this body of work some measurements of samples were taken by fellow Ph.D student David Meehan. These are declared in the appropriate place alongside the measurements in chapter 5. Chapter 8 is previously-published material from Plasma Science Sources and Technology [1]. The introduction to this chapter includes a breakdown of the work from the authorship of the paper but in summary; aside from one set of measurements the paper is entirely my own work.

Chapter 1

Introduction

1.1 Motivation

Currently under construction at Cadarache, in the South of France, is ITER (Latin for "the way" and also known as the International Thermonuclear Experimental Reactor) [2]. ITER is to be the world's largest magnetic confinement fusion reactor and is shown schematically in figure 1.1. Fusion is the binding of light particles such as hydrogen into heavier particles such as helium to release energy, it is the process that powers the Sun and hopefully a step towards meeting the energy needs of the world. In magnetic confinement fusion a hydrogen (deuterium and tritium) gas is heated to the point of ionisation, at which point it forms a plasma (defined in detail in chapter 2). This plasma is further heated to over 100 million degrees Celsius and is confined using magnetic fields, forcing the particles to interact and fuse, producing a helium nucleus (an alpha particle) and a high-energy neutron per reaction. The helium comes away with an energy of 3.5 MeV and the neutron with 14.1 MeV. This high-energy neutron is not affected by the magnetic fields as it has no charge, thus it can freely escape confinement and interact with the walls of the device, which are dense enough to slow down the neutron and convert that energy into heat, which is then used to generate electricity.

Within the reactor diagnostic tools must be used for both real-time control and experimental investigation of the plasma. The main optical systems on a reactor, such as ITER, are Thomson scattering, interferometers, and polarimeters. To protect these systems from the high neutron flux of the reactor, complicated labyrinths form the optical pathways through shielding blocks [3]. The optical component closest to the plasma in these shielding blocks is

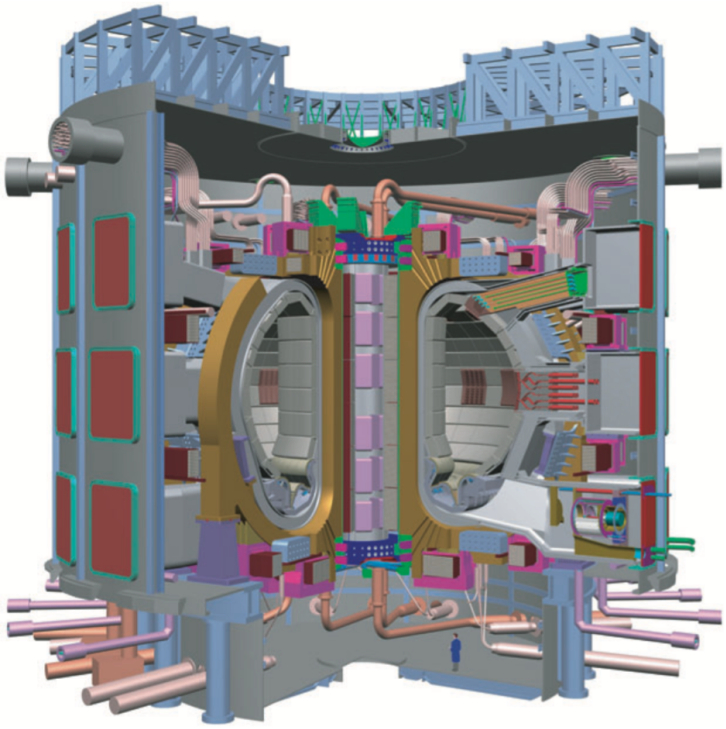

Figure 1.1: A cutaway of the ITER fusion device [2]

called the first mirror, and the current design for the optical path of one of the Thomson scattering devices can be seen in figure 1.2. These components are required to be mirrors rather than lenses as high levels of radiation lead to increased absorption in refractive optics [4].

These first mirrors, and some further inside the shielding labyrinth, undergo both erosion and deposition processes. The energetic particles formed by charge exchange within the plasma can bombard the mirrors and erode the surface. This same erosion process occurs on the nearby first wall and causes the deposition of this material on the mirrors. The performance of these mirrors is vital and their maintenance is therefore an essential challenge that we face. The wavelengths of interest fall between the vacuum UV (5 nm) to the far infra-red (118 μm) according to the list of ITER selected diagnostics [5]. To maintain optical properties the requirement is to sustain a surface roughness not exceeding $\sim$0.1 of the operating wavelength [6].

Experiments of long term erosion on reflectance of metal mirrors show that reflectivity can be easily maintained with either single crystal or small scale crystal structures. This has been shown to be true even after erosion of a layer $\sim 7\mu$m thick. However, deposition has a much greater effect on the reflectivity, with 10 - 20 nm of deposited material causing

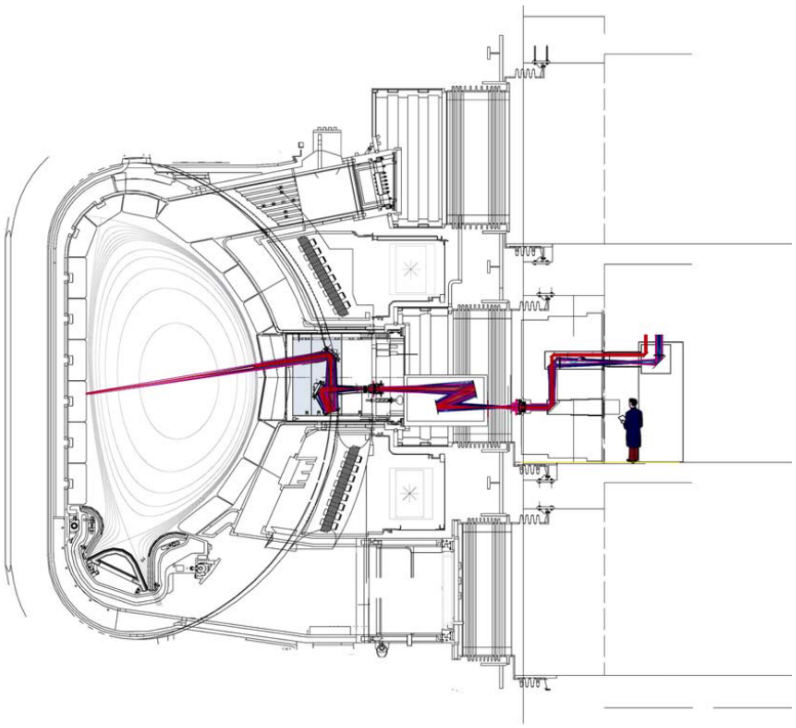

Figure 1.2: Schematic of the LIDAR (LIght Detection And Ranging) Thomson scattering system installed on an ITER equitorial port [3].

substantial degradation on reflectance [3, 6].

The first mirror test was carried out on the Joint European Torus (JET) in order to investigate ITER-relevant performance of metallic mirrors. JET is currently the world's largest fusion device and is being used as a test bed for some of the new technologies that will go on ITER. These tests were conducted in two phases from 2004 to 2009 during which JET had carbon walls [7]. ITER, in its most recent design, will have beryllium walls with a tungsten divertor, which is a change due to tritium retention being high in the carbon [8]. The choice to use beryllium is made as it is a low-Z material and, because of quasi-neutrality, the proton number of the ionised material is equal to the number of electrons that it needs to balance. This dilutes the fuel and limits reactions of D^+ and T^+, so a lower Z material is preferable to a higher one. The divertor is in the bottom of the reactor and can be constructed in a way that any eroded material doesn't make it into the plasma, so it can be constructed out of tungsten which can take a higher flux before erosion. Regardless of the wall material the need to remove depositions still remains, especially as the optical degradation has been shown to be very similar [9]. The proposed mirror materials are stainless steel, molybdenum, and the slightly lower-chemically-active rhodium-coated molybdenum mirrors.

It was proven that the main wall mirrors are dominated by erosion, however the divertor mirrors are dominated by deposition [10]. Mitigation techniques have been explored [11,12], but they have not proven able to eliminate deposit growth. There therefore is an effort towards development of reflectivity recovery procedures.

Surface morphology and reflectivity examination has shown that the optical properties of mirrors exposed in JET with carbon walls have been significantly degraded. This is mainly resulting from carbon deposition due to the range of hydrocarbon transport [13,14]. An interesting effect is that mirrors placed closer to the plasma, within the main chamber, retained more reflectivity than those hidden in recesses further away from the plasma [7]. In more recent times mirrors have been exposed to ITER like wall scenarios and, as stated earlier, the depositions are very similar. The amount of deposited material is less, as is the layer thickness, but the extent is very similar [9].

Surface profiling of the exposed mirrors from the JET ITER Like Wall (JET-ILW, the beryllium and tungsten wall discussed previously) scenarios shows some interesting features. This can be seen in the Heavy Ion Elastic Recoil Detection Analysis (HIERDA) in figure 1.3. The interface between materials is shown to be fairly broad ($\sim$50 nm), however this is not solely down to inter-diffusion of components during their life in a harsh environment; it is also error from the large beam size and impingement angle of the HIERDA device. Surface imperfections would have an impact on the pattern in the deposit surface interface. In figure 1.3 it can also be shown that the main components are beryllium, carbon, nitrogen, oxygen, and deuterium, but they have very different profiles. Each profile matches the life cycle of the mirror within the device. For example, the oxygen has two maxima: one at the surface, and one at the interface. These are most likely associated with the absorption on the exposed surface, and from the initial installation. Only the region between the two maxima can be associated with oxygen deposition during plasma operation. The beryllium profile is the least interesting, showing that it is high and uniform. The carbon deposit is high during the initial exposure to the JET-ILW, but is much lower at smaller depths. This initial carbon content is attributed to the previous carbon wall, and some carbon introduction from CO_2 leaks during non-operation. The reduction in carbon content is in line with spectroscopy measurements taken during the same phase of operation [15]. Nitrogen depositions increase towards the deposit surface and reflect H-mode operation associated with N_2 impurities from gas puffing. Deuterium has a varied profile, but shows low concentration. The most interesting feature

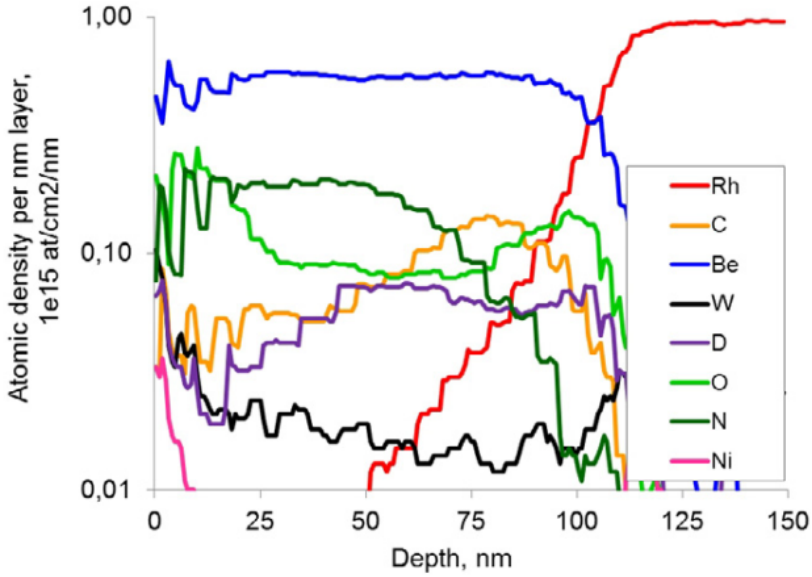

Figure 1.3: HIERDA depth profiles of co-deposited elements on an Rh-coated mirror from the inner divertor, receeded 1.5 cm into the wall taken as published from [9].

is the tungsten profile which, although low, rises in a very irregular pattern. There is also a sharp increase at the surface which corresponds to a jump in JET heating power towards the end of operation. At this sharp increase there is also the introduction of nickel, which could be attributed to antennae damage or inconel cladding tiles. This could indicate that metals are appearing sporadically, causing extra heat deposition, increased sputtering, or even evaporation. This then allows deposition of neutrals in the shadowed regions.

Methods of reflectivity recovery are being attempted from multiple angles. One main issue is the need to recover the mirrors in situ. ITER not only has a much harsher environment during operation than current devices, but will also have a more demanding operation. The intention is for the machine to have a high duty cycle (∼25%) for long periods of time [3]. During this time the device will become contaminated and activated, this will require all maintenance to be done via remote handling. Even without the contamination, the massive deposition rates on the mirrors mean that even periodic exchange of mirrors would be of limited use, or fully impractical.

Cleaning via laser pulse was investigated on mirrors exposed during the carbon wall experiments on JET [16]. A scanning laser system with a wavelength of 1064 nm, spot size diameter of 150 μm, pulse length of 120 ns, and a repetition rate of 20 kHz was used. The fluence of the laser was varied and repeatedly scanned over the same area. Damage thresholds

for the laser on the molybdenum and stainless steel mirrors were calculated and tested prior to deposit removal and showed that the molybdenum mirrors were more resistant to laser damage. The experiment then attempted removal of deposits using relatively safe laser fluences for the mirror materials. It was found that the recovery of the reflectivity was more successful on the molybdenum mirrors, possibly due to the higher fluence used. However, it is impossible to say whether this is as a result of removing more deposit, or causing less damage to the surface. Both mirror materials were found to have a higher recovered reflectivity in the infrared spectrum. Analysis of the most improved surfaces showed that removal of the final 0.02 μm of deposit was difficult, even after repeated scanning which caused significant surface damage (shown in figure 1.4). More important, for the ITER scenario, is that the remaining deposit was found to be mainly beryllium. For this method to be successful the laser parameters need further investigation and then optimisation. This will be challenging, as each deposit will have a different composition, thickness, density, and adhesion and will, therefore, require specific settings.

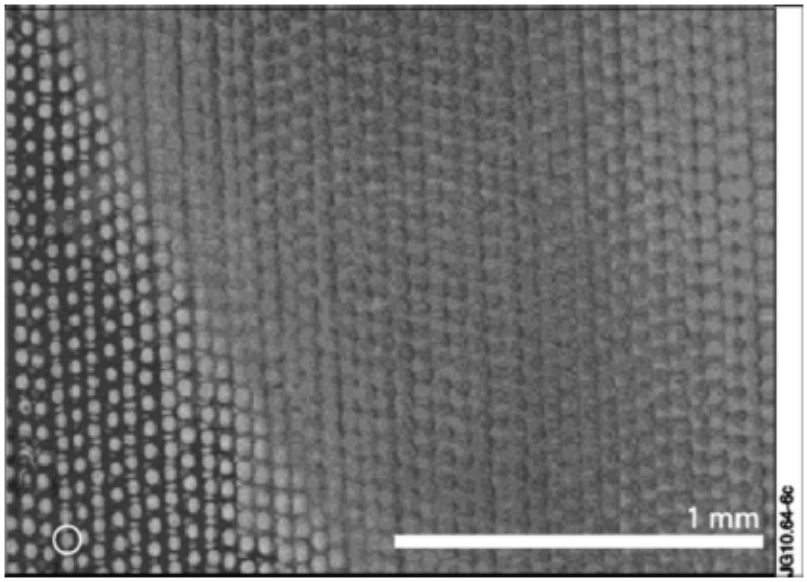

Figure 1.4: SEM image of laser damage to a molybdenum mirror. Each individual circle is a single laser pulse [16]

Deposition cleaning via two mechanical methods have been proposed and tested on mirrors exposed in JET [10]. These tests, although ex situ, allow clarification on the ability of mechanical methods to recover high reflectivity. The first method reviewed used ultrasound cleaning in an organic solvent, giving mixed results. They ranged from no noticeable effect,

to full restoration of reflectivity. On average 30-50% of visible spectrum reflectivity was recovered, and 50-90% of infrared. This is due to longer wavelengths being less sensitive to surface imperfections; similar to the previous attempts via laser pulse discussed earlier [16]. The ultrasound cleaning does give a fairly good indication of the adherence of the co-deposits to the surface, which is useful for investigation into further mechanical methods. The second method investigated was polishing using 1 μm diamond paste; carried out incrementally with the mirror reflectivity being tested after every two minutes of polishing. The results showed full reflectivity being restored to the mirrors after 30 minutes of treatment and can be seen in figure 1.5. Overall the polishing process was very successful for the molybdenum mirrors, however it is completely impractical. Even if a method could be devised for in-situ polishing, the cleaning conditions must be set for each individual mirror. The polishing process also proved too rough for the Rh coated mirrors and led to disintegration of the surface.

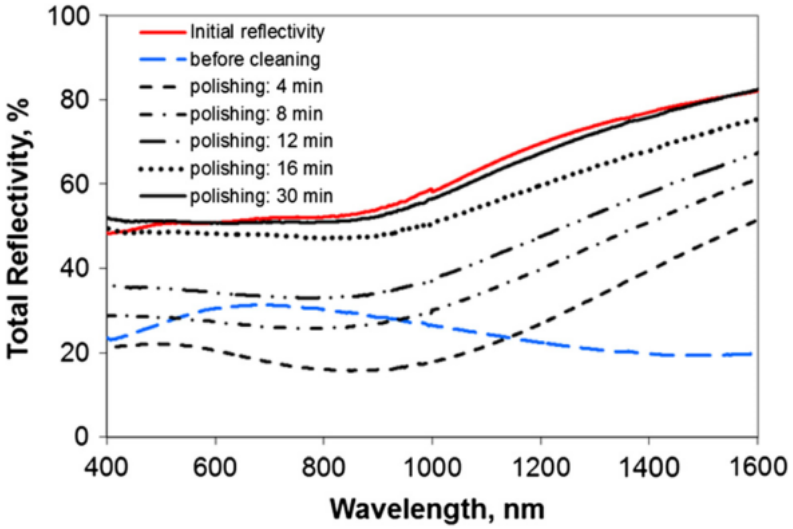

Figure 1.5: Recovery of reflectivity using a polishing process with 1 μm diamond paste on a molybdenum mirror exposed on the outer wall of JET [10]

Plasma sputtering is foreseen as another method that could be implemented to remove main wall deposits. With tests proving that plasma cleaning can remove aluminium oxide (a beryllium proxy [17]) from mirrors [18], research has been done on the performance of this method in ITER-like conditions [19]. Some of this work has involved using an external plasma source to create ions, which are then attracted to the mirror using a bias voltage. This method was abandoned as it performed poorly with insulating films and would require installation of the plasma source at all mirror locations. The current design uses the mirror

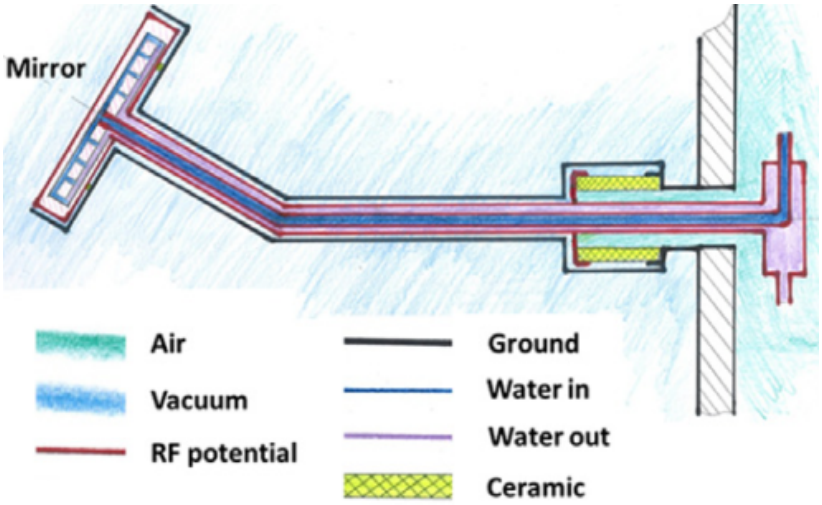

Figure 1.6: Schematic of the first insulating solution for implementation of the RF discharge cleaning method on ITER first mirror [19]

as the powered electrode in a CCP (Capacitively Coupled Plasma). This design is one that is seen to be the most promising prospect for installation on ITER and methods for implementation of this have been proposed, as can be seen in figures 1.6 and 1.7.

Using the mirror as a CCP in this way has been through a successful experimental proof of concept campaign by Moser at the University of Basel in Switzerland [20]. This has not delved deeply into actual implementation but has investigated the initial idea in some detail. A brief summary of the results is that the CCP method works in all tested cases with there being a direct link in the etch rate and the ion energy, which is controlled using the substrate bias. For the removal of deposits the most effective gas for etching was found to be Ar at $\sim$ 230 eV, as it produced a fast etch rate in comparison to other gasses such as He or D, even with these lighter gasses at $\sim$ 630 eV. Although it is said that lower energy Ar was tested and did not produce good results, the data is unavailable in the published work [20]. A large number of deposits were removed of various components in multiple reactors which makes comparisons and thus conclusions difficult.

In this thesis an investigation will be carried out into the feasibility of modelling the plasma cleaning method proposed to go on ITER. It is clear that experiments cannot be carried out for every mirror geometry as each will be different and require an analogous experiment. By using a model the plasma parameters could be optimised for each mirror, giving the most efficient etch, and with as little damage to the mirrors as possible. The investigation will use the HPEM (Hybrid Plasma Equipment Model) which will be set up

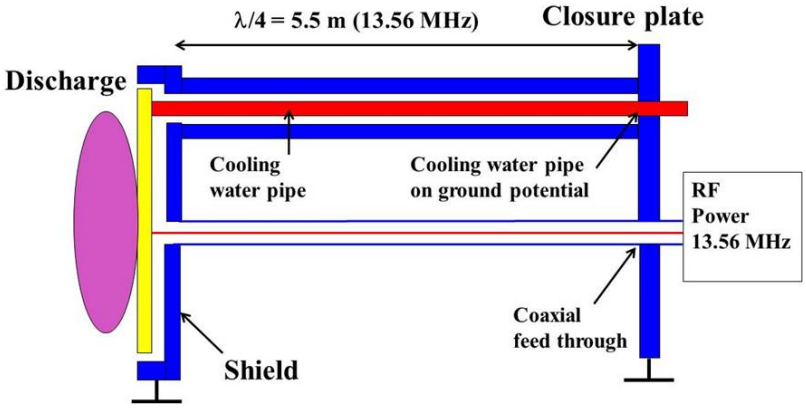

Figure 1.7: Schematic of the $\lambda/4$ stop band filter installation for the RF discharge cleaning method [21]

to simulate deposition removal carried out experimentally at York, and then be used to investigate further variables in other geometries. The setup of the model will include the implementation of an Ar/O/Al gas chemistry, the creation of an Al/O surface chemistry, and the creation of a Ar/Be/O gas chemistry.

1.2 Outline

This thesis is set out as follows:

Chapter 2 is a theoretical background to the fundamental plasma physics that is key in the work presented. A focus is given to capacitively-coupled plasmas, the plasma sheath, and its involvement in the process of plasma etching.

Chapter 3 discusses modelling methods within low-temperature plasma physics. The choices that must be made when deciding on a modelling approach are given and applied to this work. The hybrid model being used is then presented, along with some governing parameters and boundary conditions. The gas phase and surface chemistry reaction sets are also given.

Chapter 4 presents the experimental methods conducted at York. A description of the experimental geometry and the experimental parameters used for both deposition and erosion of Al_2O_3 is given. Results of the deposition are then presented. The atmospheric

pressure plasma jet is described and some motivation for its use given.

Chapter 5 is a benchmark of the modelling with published literature and experimental work conducted in York.

Chapter 6 presents some further modelling work with a focus towards ITER, using comparisons with previously published results from another group, and a simplification of the model geometry for parameter optimisation.

Chapter 7 discusses the generation of a beryllium gas chemistry for use within the model and presents some initial results.

Chapter 8 is a standalone chapter showing published work into surface modification of polymer films using the effluent of an atmospheric pressure plasma jet. It shows the impact of atomic oxygen from the APPJ on the surface of polypropylene, causing an increase in the hydrophilicity of the plastic.

Chapter 9 brings together the conclusions of this study and details an outlook to possible future endeavours.

Chapter 2

Plasma fundamentals

For the details of the work presented in this thesis to be understood, an initial knowledge of plasma physics is required. There must be some understanding of the general theories, the techniques used to model a simple plasma, and the difficulties faced within this process. This chapter covers the basics that should provide an understanding of those that follow. If more information is desired then the reader is directed towards more comprehensive works, for example [22, 23]

2.1 The definition of a plasma

It is often said that plasma is the fourth state of matter. By adding energy you can turn a solid into a liquid, and a liquid into a gas. When energy is added to a gas the electrons can detach from the nucleus in a process called ionisation. Most gases exhibit a small degree of ionisation but for it to be considered a plasma it must be a quasi-neutral collection of charged and neutral particles that exhibit collective behaviour [23].

2.1.1 Collective behaviour

In a gas at atmospheric pressure and room temperature, a neutral particle will drift until it collides with another particle and a transfer of momentum takes place. These collisions fully control the motion of the particles within the gas as the neutral particles do not feel any influence from any electromagnetic fields. Energy may be input into the system through sound waves or any other physical bombardment that relies on collisions. In a plasma; charged particles form local concentrations of net positive or negative charge that create

electric fields. The motion of charges also causes currents to flow which form magnetic fields. These fields have non-local interactions with other charged particles within the plasma and will have an effect on their motion. Thus we can define collective behaviour as the long-range interactions of charged particles through the Coulomb force.

2.1.2 Quasi-neutrality

Quasi-neutrality is the ability of the plasma to appear neutral on a macroscopic scale. However, this is not quite as simple as it sounds. In order to properly define this term we must first define the Debye length. If we inserted a sphere of positive charge into a plasma, in the local area the electrons would be mobilised to the sphere due to their significantly lower mass than that of the positive ions. A cloud of electrons would form around the positive sphere and shield the rest of the plasma from its effects. The Debye length, λ_D, is the distance at which the effects of the positive charge are effectively screened by the cloud of electrons. It can be defined as:

$$\lambda_D \equiv \left(\frac{\epsilon_0 k_b T_e}{n e^2} \right)^{\frac{1}{2}} \tag{2.1}$$

In (2.1), ϵ_0 is the permittivity of free space, k_b is Boltzmann's constant, T_e is the electron temperature in Kelvin, n is the plasma density, and e is the electric charge. It can be seen that the Debye length is dependent on the temperature of the electrons. This is because electrons with a high enough thermal energy on the edge of the cloud may escape the electrostatic force from the potential well. This decreases the effectiveness of the shielding and thus increases the Debye length.

In order for Debye shielding to take place there must be a consideration for the number of particles available to form the cloud. It is axiomatic that there must be a sufficient number of charges present around the sphere of positive charge to successfully shield it. Thus the plasma parameter, the number of electrons contained within sphere of radius λ_D, gives a good indication of whether collisions or electrostatics are the dominant forces within a plasma and can be defined as:

$$N_D = \frac{4}{3} \pi n \lambda_D^3 \tag{2.2}$$

We are now in a position to say: If the overall dimensions of a plasma system are significantly greater than that of the Debye length, and there are sufficient charges within

the region ($N_D \ggg 1$), then any local net charge will be shielded on a length scale much smaller than that of the system. Thus there will be no electric field associated with the macroscopic system, but there may be fields on a microscopic scale in certain areas. The system can now be called quasi-neutral. Thus we can say that the plasma density, n, used in equations (2.1) and (2.2), is such that there are approximately equal numbers of positive and negative charges on a macroscopic scale.

2.1.3 Low-temperature plasmas

Plasmas exist is many forms. From astrophysical bodies such as nebulae and stars, to those created on earth in the pursuit of nuclear fusion. In this work the studies will focus on low-temperature or non-thermal plasmas where the degree of ionisation is very low ($< 1\%$), and the low-mass particles and high-mass particles are not in thermal equilibrium. One way of creating these plasmas is using high-frequency, time-varying electric fields, which cause the electrons to be heated and ionise surrounding particles. The high-mass particles cannot react sufficiently quickly due to their high inertia and, therefore, do not significantly heat up. This allows these plasmas to be used for many applications where the chemistry created by the electrons of a few eV can be exploited in a room-temperature background gas (~ 0.03 eV).

The work presented here has used plasma systems within two pressure ranges. The main body of work has been done with low-pressure plasmas that will run within the ITER environment. Research on these types of plasmas has been done over many decades, as it is industrially relevant for computer chip manufacture. However, the limitations imposed by the ITER environment force new applications and areas of study to be developed. Some work has also been done with an atmospheric-pressure plasma source which is used primarily in biomedical applications. For this work both systems are Capacitively-Coupled Plasmas (CCP), the fundamentals of which are discussed within this chapter to form a basis of understanding of the results shown later.

2.2 Etching mechanisms

Plasma etching has been studied in great detail as the technology responsible for producing microprocessors [24], and as a replacement for wet etching using solvents. Plasma etching

can be split into two types; chemical and physical. Physical etching is also called sputtering and involves bombardment of a substrate by ions which impact the material with sufficient energy to displace and eject surface atoms [25]. This process is greatly improved through biasing the powered electrode, the surface on which the substrate is placed, in order to increase ion energy, which is the key control parameter. How this occurs will be discussed in section 2.3.1.4. Chemical etching uses the chemistry of the plasma to react with the surface and produce volatile products which are then swept away with the gas flow.

It is important to understand the stage of the process in which the plasma etching is used. The dry etching process is first described in Penn 1979 [26]: An Si substrate has an SiO_2 layer deposited on its surface which subsequently has a photoresist layer deposited on top. The photoresist is hardened by radiation (usually UV) through an optical mask and the softer areas removed through a bake and develop process. In the bake the volatile components of the photoresist are driven away at different rates in the exposed and unexposed areas, resulting in thinning in the unexposed areas. In the develop process a plasma is used to remove a layer of the photoresist across the entire surface and therefore expose sections of the SiO_2. This forms a photoresist mask that will etch at a slower rate to the SiO_2 and thus can hide sections to form the architecture required.

A need to reduce chemical waste was a driving force behind the progress of plasma etching [26,27]. By using plasmas in the process instead of wet chemicals the costs associated with purchasing and disposing of the industrial solvents are eliminated. Highly reactive gasses are still required for the etching process but management of these is much easier and more cost effective. Chemical etching was originally done in a radial flow reactor where the substrates were placed on the grounded electrode with the RF applied to the upper electrode [28]. Physical and chemical sputtering were then investigated in parallel, through the introduction of reactive gasses into a physical sputtering apparatus by Hosokawa *et al.*, to investigate increased etch rates [29].

2.3 Capacitively coupled plasmas

CCPs are usually formed between two parallel plate electrodes where one electrode is grounded and the other is powered by a high voltage. In all of the following work the voltage is within the Radio Frequency (RF) range, because 13.56 MHz and its harmonics are reserved frequen-

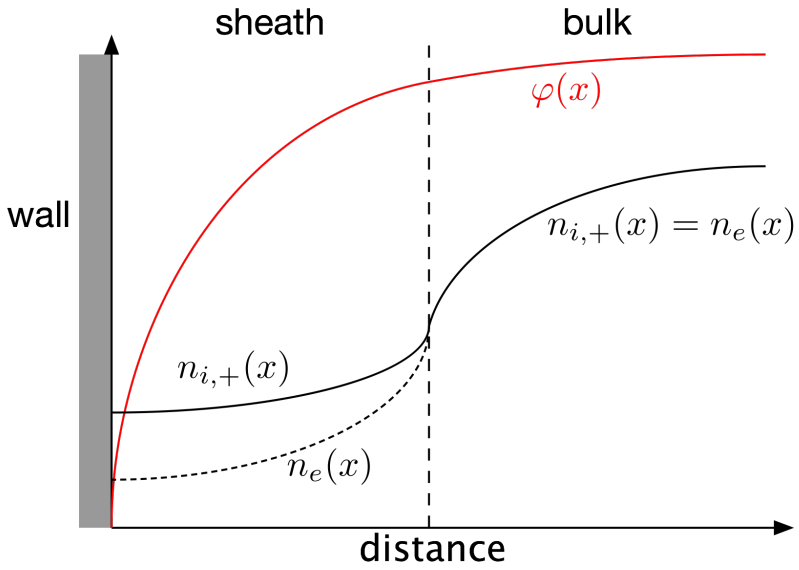

Figure 2.1: Schematic of charged particle densities (electrons, n_e, and positive ions, $n_{i,+}$) and the resultant potential in the plasma sheath (φ).

cies for industrial use. The high frequency, in low pressure, accelerates free electrons which ionise the background gas. These released electrons are then in turn accelerated, continuing the process until the point where the definition of a plasma is met.

2.3.1 Plasma sheath

Consider a plasma, powered by some external entity, confined within a grounded vessel. Where a plasma meets the bounding walls the ions and electrons will recombine and be lost. As the electrons have significantly lower mass than the ions they will have greater velocity and will reach the wall faster. This leaves a thin region of net positive volume charge density causing a potential valley, which is positive in the plasma but zero at the wall, as shown in figure 2.1. It accelerates any ion that enters the region towards the wall, and maintains itself so as to reflect most electrons back into the plasma such that the flux of ions and electrons to the wall is equal, i.e. the net conduction current through this space is zero. This region is called the sheath.

Now consider a plasma confined between two electrodes; one grounded and one powered by an RF supply as shown in figure 2.2. In this configuration the electrodes are separated by a distance, d, and the plasma has a width, w. Between the plasma and the electrodes exist the sheaths of varying thickness, $s_a(t)$ and $s_b(t)$, as the plasma oscillates between the two electrodes. The sheaths expand and contract over one RF cycle such that the plasma

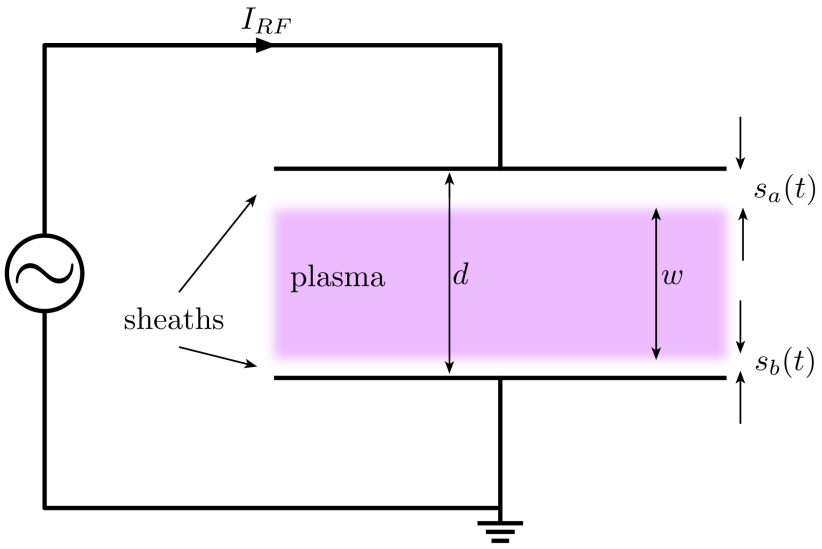

Figure 2.2: A simple schematic of a symmetrical RF CCP.

width stays the same. For simplification it can be assumed that n_e is zero within the sheath. This is a good approximation if the electron Debye length is much smaller than the average sheath width, $\vec{s}$, which is true if T_e is much less than the DC voltage across the sheath. As the edge of the sheath denotes the edge of the quasi-neutral plasma it must be that, at the plasma edge of the sheath and within the bulk plasma, $n_e = n_i$.

The analysis can now be taken in multiple directions through either the homogeneous model or the inhomogeneous model. The latter, as the name would suggest, has n_i decreasing from the plasma to the wall due to their acceleration, as shown in figure 2.1. The analytical solution to this model is a very involved process and the reader is directed towards Lieberman (1988) for detailed calculations [30]. The homogeneous model assumes that the n_i is uniform and constant in time throughout both the sheath and the plasma bulk. This approach is less physically accurate in comparison with the inhomogeneous model, but it does suffice for the purposes of this explanation. The following derivations for this model are given in more detail in Lieberman and Lichtenberg (2005) [22].

The current flowing through the two sheaths is made up of displacement current and conduction current. Conduction current is a classic description of current describing the flow of charges in a circuit under the influence of an electric field. It is mainly carried by electrons in a discharge. Displacement current is not really a current, although it shares the same units, as it does not involve movement of particles, but is a time-varying electric field.

2.3.1.1 Displacement current

Poisson's equation gives the electric field $\mathbf{E} = \hat{x}E$ within sheath "a" as

$$\frac{dE}{dx} = \frac{en_{i,e}}{\epsilon_0} \tag{2.3}$$

where $x \leq s_a(t)$. Which when integrated gives

$$E(x,t) = \frac{en_{i,e}}{\epsilon_0}(x - s_a(t)) \tag{2.4}$$

At $s(t)$, where the sheath meets the bulk plasma, $E \approx 0$ due to the continuous nature of the field at the boundary, and the small electric fields present in the plasma (as explained in section 2.1.2). The displacement current from sheath "a" into the plasma is defined as

$$I_{ap}(t) = \epsilon_0 A \frac{\partial E}{\partial t} \tag{2.5}$$

where A is the cross-sectional area of the sheath, which is also the surface area of the electrode. We can substitute (2.4) into (2.5) to get

$$I_{ap}(t) = -en_{i,e}A\frac{ds_a}{dt} \tag{2.6}$$

This shows a linear relation between the oscillation of the sheath boundary and the applied current, which can now be set as $I_{RF} = I\cos\omega t$, where $\omega = 2\pi f$ and is the angular frequency (rad/s). It is inserted into (2.6) and the resulting equation integrated to obtain

$$s_a = \vec{s} - s_0 \sin\omega t \tag{2.7}$$

where

$$s_0 = \frac{I}{en_{i,e}\omega A} \tag{2.8}$$

and is the amplitude of the oscillation about $\vec{s}$. The voltage across the sheath is the integral of the electric field across the sheath as such

$$V_{ap}(t) = \int_0^{s_a} E dx = -\frac{en_{i,e}s_a^2}{2\epsilon_0} \tag{2.9}$$

This shows the voltage is not linearly related to the oscillation of the sheath boundary. It is also therefore not linearly related to the applied current. By inserting in s_a from (2.7) into (2.9) the following is obtained

$$V_{ap} = -\frac{en_{i,e}}{2\epsilon_0}\left(\vec{s}^2 + \frac{1}{2}s_0^2 - 2\vec{s}s_0\sin\omega t - \frac{1}{2}s_0^2\cos 2\omega t\right) \tag{2.10}$$

which gives us a second harmonic in the voltage with a constant average value.

Moving on to sheath "b" the process can be repeated to give

$$I_{bp}(t) = -en_{i,e}A\frac{ds_b}{dt} \tag{2.11}$$

with a subsequent voltage of

$$V_{bp} = -\frac{en_{i,e}s_b^2}{2\epsilon_0} \tag{2.12}$$

Current within the system must be conserved so $I_{bp} = -I_{ap}$. Adding (2.6) and (2.11) and integrating the result gives

$$s_a + s_b = 2\vec{s} \tag{2.13}$$

proving that $w = d - 2\vec{s}$ as shown in figure 2.2. As for sheath "a" the applied current is inserted as $I_{bp} = I_{RF} = I\cos\omega t$ into (2.11) and integrated to obtain

$$s_b = \vec{s} + s_0\sin\omega t \tag{2.14}$$

which is in turn input into (2.12) to give

$$V_{bp} = -\frac{en_{i,e}}{2\epsilon_0}\left(\vec{s}^2 + \frac{1}{2}s_0^2 + 2\vec{s}s_0\sin\omega t - \frac{1}{2}s_0^2\cos 2\omega t\right) \tag{2.15}$$

Taking V_{bp} (2.15) from V_{ap} (2.10) gives the combined voltage across the two sheaths as

$$V_{ab} = \frac{en_{i,e}\vec{s}}{\epsilon_0}(s_b - s_a) \tag{2.16}$$

where s_a, (2.7), and s_b, (2.14), can be substituted into (2.16) to conclude with a linear voltage response to the applied current:

$$V_{ab} = \frac{2en_{i,e}\vec{s}s_0}{\epsilon_0}\sin\omega t \tag{2.17}$$

2.3.1.2 Conduction current

The conduction current, as previously mentioned, is the flow of charged particles through the sheath. It has also been stated that the sheath thickness $\vec{s}$ is determined by a balance of flux of ions and electrons. The assumption has been made that the ions respond to the time-averaged potentials, and thus we can assume that there is a constant flow of ions through the sheath. This flow will carry a steady current

$$\vec{I_i} = en_{i,e}u_B A \tag{2.18}$$

in which u_B is the loss velocity set at the Bohm velocity. As the net flux of ions and electrons must be zero, and n_e has been set to approximately zero in the sheath, the thickness of the sheath $s_a(t)$ must be zero at some stage during the RF cycle. This would allow electrons to pass to the electrode in an instant, and maintain the net flux. Therefore, the average sheath thickness $\vec{s}$ must be equal to the amplitude of the sheath oscillation s_0 in order for the sheath thickness to become zero. Therefore

$$\vec{s} = s_0 = \frac{I}{en_{i,e}\omega A} \tag{2.19}$$

For the two sheaths this results in (2.10) and (2.15) becoming

$$V_{pa} = \frac{en_{i,e}s_0^2}{2\epsilon_0}(1 - \sin\omega t)^2 \tag{2.20}$$

and

$$V_{pb} = \frac{en_{i,e}s_0^2}{2\epsilon_0}(1 + \sin\omega t)^2 \tag{2.21}$$

Now circuit theory relates the capacitance to the voltage as $q(t) = CV(t)$. Differentiating this where $V(t) = V_{ab}(t)$ from (2.17) shows

$$\frac{dq}{dt} = I = C\frac{2en_{i,e}\vec{s}s_0}{\epsilon_0}\omega\cos\omega t \tag{2.22}$$

which we can further simplify by using I_{RF} and (2.19) to find a linear sheath capacitance

$$C = \frac{\epsilon_0 A}{2s_0} \tag{2.23}$$

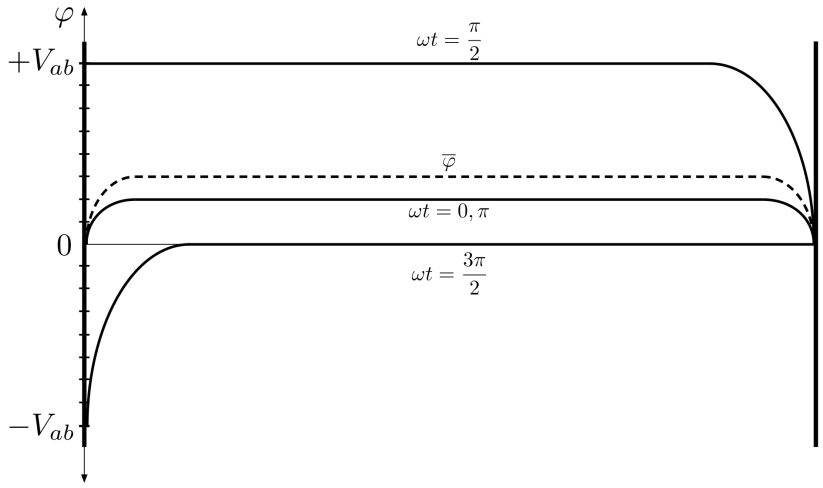

Figure 2.3: The spatial variation in potential φ between symmetric electrodes of a CCP at different times during the RF cycle. The time averaged potential $\vec{\varphi}$ is also shown.

This is an important result as it relates the capacitance to the cross-sectional area of the sheath and therefore the surface area of the electrode. The variation of the potential between symmetrical electrodes in this example is shown in figure 2.3.

2.3.1.3 Electrode self bias

Consider an asymmetrical device where the grounded electrode is larger than the powered electrode. The sheaths in this system can now be modelled as capacitors. Circuit theory states that $V = I/C$ which can be used with equation (2.23) to give

$$V = \frac{2s_0}{\epsilon_0 A} \int I dt \tag{2.24}$$

where continuity of current is maintained. This relationship shows that the voltage drop across the sheaths is inversely proportional to their capacitance and surface area; the smaller the surface area of the electrode the smaller the capacitance and thus the larger the voltage drop. With large asymmetry almost all the RF potential can be corrected by the larger sheath on the smaller electrode, which can cause ions to impact the surface with energies near to the RF amplitude. The variation in the potential between the electrodes of an asymmetric discharge can be seen in figure 2.4. This is the "self bias" of the system, which is key in physical etching applications due to the increased ion energy caused by their acceleration through the larger sheath.

Another method of biasing an electrode is to float the powered electrode through the

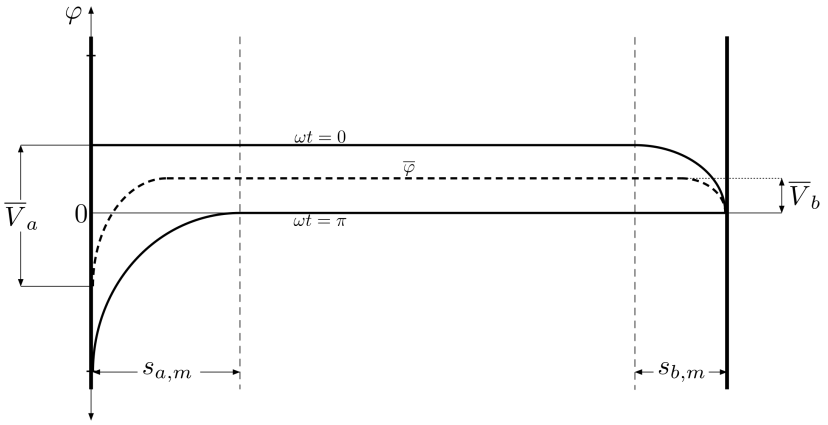

Figure 2.4: The spatial variation in potential φ between asymmetric electrodes of a CCP, where the grounded electrode (b) is bigger than the powered electrode (a), at two different times during the RF cycle. The time-averaged potential $\vec{\varphi}$ and the maximum widths of the sheaths, $s_{a,m}$ and $s_{b,m}$, are also shown. The bias voltage in this case is $\vec{V}_b - \vec{V}_a$.

use of a "blocking" capacitor [31]. By placing a capacitor between the electrode and the power supply the AC current can still reach the electrode, but when the initial electrons are incident on the surface they cannot flow to ground through the power supply as the DC current cannot pass the capacitor. This sets up an additional DC component across the electrodes that increases the ion energy beyond that of the RF amplitude. In general most plasmas will have asymmetry, as the grounded area of the majority of vessels is much greater than that of their powered electrodes. Due to the increase in energy that can be achieved through the placing of a blocking capacitor both methods are usually used concurrently, especially in plasma etching applications.

2.3.1.4 Ion energy distribution functions

In etching applications it is the voltage drop across the sheath that dictates the ion energies and therefore is an important control parameter. Understanding the sheath dynamics is essential in order to optimise and control the etching process. In the case of this work the ion energies must be high enough to eject a particle from the surface deposit but low enough not to damage the underlying mirror. The ions are not simply mono-energetic, but distribute themselves by energy depending on the plasma parameters. Any parameter which increases the pressure or the sheath width will increase the number of collisions experienced by ions within the sheath, and decrease the average ion energy through a shift in the Ion Energy Distribution Function (IEDF).

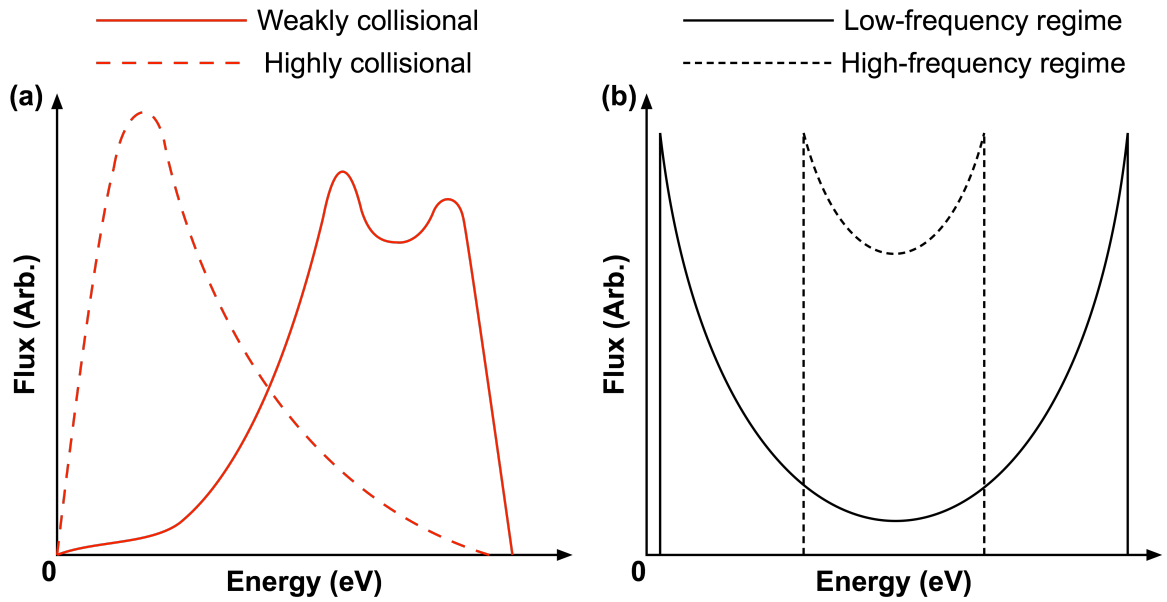

Figure 2.5: Typical IEDFs at various parameters. (b) shows IEDFs for collisionless sheaths. For the weakly collisional line in (a) and both lines in (b) the dip between the bimodal peaks represents the average sheath potential. For the low-frequency regime in (b) the bimodal peaks are at the sheath maximum and minimum potential. The weakly collisional IEDF is also shifted slightly along the energy axis for clarity, this is usual when there is a bias on the surface

The collisions of the fast-moving ions with the relatively stationary neutrals can either be simply scattering or involving charge exchange. In both processes the ion will impact the neutral and transfer some energy while undergoing a change in trajectory. The result of scattering is a still-relatively-fast ion and a slow neutral. However, if there is a charge-exchange collision the ion will also neutralise whilst the initial neutral will ionise, resulting in a slow-moving ion and a relatively-fast-moving neutral. The slow-moving ion will be partially through the sheath and will be accelerated from where the collision took place, thus it will not reach the same velocity as ions that did not undergo collisions. This results in a significant decrease in ion energies at the surface due to charge-exchange collisions. Figure 2.5 shows IEDFs for collisionless, weakly-collisional, and highly-collisional sheaths.

In a collisionless sheath, usually found in pressures below 7.5 mTorr (1 Pa), the mean free path of the ions will be greater than the average sheath width. If the transit time of the ion across the sheath is much smaller than the RF period then the discharge is said to be in a low-frequency regime, where the ions can respond instantaneously to the sheath voltage. This means that the phase of the RF cycle at which the ions enter the sheath has a major impact on the velocity of the ion when it reaches the surface. As the voltage varies most

slowly at the maximum and minimum sheath voltages, more ions are accelerated through the sheath at these points than at any other time during the cycle. This gives the IEDF a bimodal structure, which is seen in figure 2.5.

Most RF CCPs operate in a higher-frequency mode where the ion transit time is greater than the RF period. The ions, due either to greater mass or higher RF frequencies, cannot respond instantaneously; taking multiple RF cycles to cross the sheath, and the phase at which they enter the sheath is not so important in determining their energy when they contact the electrode. This narrows the bimodal structure and can lead to a single peak.

IEDFs are crucially important for etching and it is clear that the plasma parameters can dramatically alter their structure. It is therefore a requirement to understand the plasma in order to control the IEDF, and subsequently etching.

Chapter 3

Plasma modelling

3.1 Modelling low-temperature plasmas

Experimental plasma physics is able to measure a vast range of plasma properties, however it has not reached a stage where the full characterisation of low-temperature plasmas is possible. While experimental approaches are developed the gaps in knowledge can be filled through the modelling of specific processes. This is especially true when considering certain parameter variations that are difficult to change experimentally, such as geometry.

Restrictions on the model that can be used generally depend on the information that is required in terms of the amount and the accuracy. Both of these are bounded by the computing power and memory available. If the requirements are for only general trends from a simplified system then an analytical model using a range of assumptions can be utilised. This type of model uses very broad assumptions and outputs simple descriptions of processes or properties which can be useful to interpret experimental results. The simplicity of these models can make them quick and easy to run and thus they are able to complete multiple runs over a parameter space in a relatively short period of time. If this simple description does not suffice then numerical models, which use less assumptions, can be implemented. The most accurate numerical method of modelling a plasma would be one that keeps track of every particle in a system, resolves all interactions, and subsequently tracks the products of those interactions. However, a typical system may have $\sim 10^{21}$ particles which makes this impossible due to memory and computational complexity limitations.

The rest of this section will discuss numerical models as particle-based systems, fluid-based systems, and finally hybrid systems. The hybrid system utilises a combination of

particle and fluid systems and is the method being used within this work.

3.1.1 Particle methods

An approximation that is used in particle systems is to lump together groups of particles into macro-particles that represent 10^5 to 10^9 physical particles to reduce memory requirements [32–34]. These particles then have their motion determined by Newtonian laws, and collisions are stochastic, in both occurrence and type, in what is known as a Monte-Carlo Collision (MCC) scheme. This is still a large number of particles to deal with so a further approximation is made to split the system into cells of a few hundred macroparticles each, resulting in a scheme called Particle-In-Cell (PIC). PIC methods solve the equations of motion for individual macroparticles within the cell, whilst solving for magnetic and electric fields on a fixed grid of cells by averaging individual particle effects to the nearest cell boundary. By including the MCC scheme within this method the PIC-MCC simulation is created, which is a frequently used approach when dealing with non-equilibrium plasmas.

The major advantage of PIC-MCCs is the relatively small number of assumptions that need to be made. With direct treatment of particles and Maxwell's equations there is no requirement to make any assumptions about energy distribution functions. This method is still computationally expensive, and it can become more so in any situation where macroparticle numbers or the frequency of collisions are increased, such as through system pressure or complex chemistries. A good pressure range is considered to be 1-100 Pa where effects such as collisionless heating can be successfully predicted [35]. The high computational expense has led researchers to develop further methods to improve the speed of these codes [36–38], however they remain typically slower than fluid codes. This is not to say that PIC codes are not successfully used for the higher pressure regimes, even up to atmospheric [39–41].

3.1.2 Fluid methods

Fluid methods evolve the densities and fluxes of particles on a set of grid points. They are also known as continuum methods as they model the distributions, such as energies, densities, and velocities, as a continuous function. This is usually with a variation in time and one or more spatial dimensions [42–45]. These are obtained through the first three velocity moments of the Boltzmann equation, which give the conservation equations for mass, momentum, and energy [23]. This approach avoids the large amounts of memory required

when keeping track of individual particles or macroparticles, and can have relatively fast solution times in comparison with particle approaches. Parameters that would increase the complexity of a particle simulation, such as increased densities or chemistries, can also be included and studied within a reasonable time frame. One issue is that the assumption of a specific velocity based on the local electric field means that fluid models struggle to account for non-local particle kinetics. They are therefore suited to higher pressure systems where collision frequency is high; the distribution functions remain close to Maxwellian, and non-local effects are minimised. They are often used in the study of atmospheric pressure devices such as atmospheric-pressure plasma jets [46, 47].

3.1.3 Hybrid methods

Hybrid models are a combination of modelling methods, classically fluid and PIC. The philosophy of the hybrid code used in this work, the Hybrid Plasma Equipment Model (HPEM), is "to provide the maximum amount of "unprejudiced" physics that enables the user to choose the right processes for the right problem" (M. Kushner, personal communication, March 2016). This is an approach used by all hybrid codes, as the structure of the code depends on the physics being investigated. As a fluid code may not fully resolve some of the physics due to the assumptions being made, it might be that certain elements could be modelled more accurately using a PIC scheme; thus the two are convolved.

This is done through the implementation of computational modules that can address different processes, or the same process using alternative methods. The modules then pass information between each other in a hierarchical fashion where, regardless of method used, the output of one module can be read by the next. Which elements are represented by which method depends on the situation being simulated but it is possible to resolve all the important physics and keep the computation time below that of a purely particle approach.

3.2 The hybrid plasma equipment model

HPEM is a 2D modular plasma simulation code which incorporates a range of methods to simulate low-temperature plasma sources. This model was developed by Mark Kushner and his collaborators. A brief explanation of the code follows but a more detailed description can be found in [48] and [49]. The basic set up of the modules for this work is shown in

figure 3.1. The initial module of the code is the Electromagnetics Module (EMM), which takes inputs of currents, material properties of the geometry surrounding the plasma, and plasma conductivity to solve Maxwell's equations. The output of the EMM are the vector components and phase of the electric and magnetic fields. These are fed to the Electron Energy Transport Module (EETM), which in turn outputs the electron impact rate coefficients and sources derived from the solution to Boltzmann's equation. This can be done with a Monte Carlo approach, depending on the situation, but as is typical in hybrid modelling the method of calculating these outputs does not affect the modules by which they are being read. In turn these outputs go to the Fluid Kinetics Poisson Module (FKPM), which solves for electron, ion, and neutral transport, with associated fields using Poisson's equation. These can then be fed back into the EETM in order to converge the simulation towards a solution. At this point the source functions and electric fields can be taken by the Plasma Chemistry Monte Carlo Module (PCMCM), which outputs the energy distribution functions of the heavy particles specifically to be fed to the Surface Kinetics Module (SKM). This is where they can be used with an input surface chemistry file to give surface coverages, surface reaction probabilities, etch rates, and deposition rates, at all points along the plasma-surface boundary. Particles that leave the surface and enter the plasma can then be included in the calculations within the FKPM and evolved. More details as to the methods employed by this work within these modules are given in this chapter but, for a full description, the reader is directed towards [49–52].

3.2.1 Governing parameters

The equations that form the basis of the HPEM model, and specifically the FKPM, come from the first three velocity moments of the Boltzmann equation [22,23]. These conservation equations are given below in the absence of magnetic fields.

$$\frac{\partial n}{\partial t} + \vec{\nabla} \cdot (n\vec{u}) = S \tag{3.1}$$

$$mn\left[\frac{\partial \vec{u}}{\partial t} + (\vec{u} \cdot \vec{\nabla})\vec{u}\right] = \pm qn(\vec{E} - \vec{\nabla}p - mn\nu\vec{u}) \tag{3.2}$$

$$\vec{\nabla} \cdot \left(\frac{3}{2}p\vec{u}\right) = \frac{\partial}{\partial t}\left(\frac{3}{2}p\right)\Big|_c \tag{3.3}$$

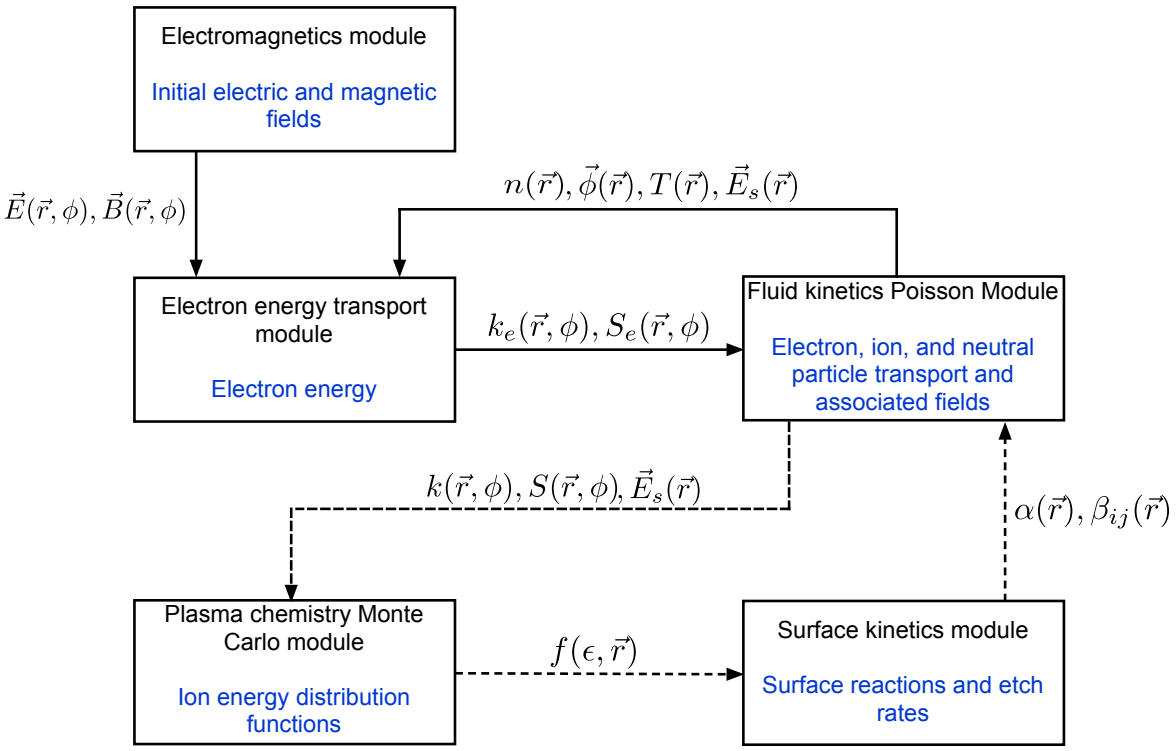

Figure 3.1: Flow chart showing the main modules of HPEM used in this work. The dotted path is only followed once the gas chemistry has reached a steady state. Symbols are defined in table 3.1.

In all of the above, $\vec{u}, m, \epsilon$, and q are the mean velocity, mass, mean energy, and charge of the specific species used in the calculation. p, ν, and $\vec{q}$ are the pressure, collision frequency, and heat flux within the fluid. Equation 3.1 describes the conservation of mass and is known as the *equation of continuity*. The right hand side is a source term that accounts for any mass gains or losses through particle collisions. Equation 3.2 is the *fluid equation of motion* and describes the conservation of momentum where the $\pm$ indicates the sign of the charge of the species in question. Equation 3.3 describes the conservation of energy with the right hand side accounting for collisional processes. These include ionisation, excitation, elastic scattering, and ohmic heating. The closure of this set of equations is done by Poisson's equation for the electric potential which is given below and where j refers to a single species.

$$\vec{\nabla}\Phi_s = -\frac{1}{\epsilon_0}\sum_j q_j n_j \tag{3.4}$$

Within HPEM there are choices on how to include these equations within the code. As with all codes these choices depend upon the computational efficiency and the range of

$(\epsilon, \vec{r}, \phi)$	dependence of energy, position, and phase in harmonic period (or time)	$f(\epsilon, \vec{r}, \phi)$	distribution function ($eV^{-3/2}$) in the gas phase or incident onto surfaces
$k_e(\vec{r}, \phi)$	electron impact rate coefficients ($cm^3 s^{-1}$)	$S_e(\vec{r}, \phi)$	electron impact source functions ($cm^{-3} s^{-1}$)
$k(\vec{r}, \phi)$	heavy particle collisional rate coefficients ($cm^3 s^{-1}$)	$S(\vec{r}, \phi)$	heavy particle collisional source functions ($cm^{-3} s^{-1}$)
$\vec{E}(\vec{r}, \phi), \vec{B}(\vec{r}, \phi)$	electromagnetic fields ($V cm^{-1}, G$)	$\vec{E}_s(\vec{r}, \phi), \vec{B}_s(\vec{r}, \phi)$	electrostatic and magnetostatic fields ($V cm^{-1}, G$)
$n(\vec{r})$	density (cm^{-3})	$\vec{\phi}(\vec{r})$	flux ($cm^{-2} s^{-1}$)
$T(\vec{r})$	temperature (K or eV)	$\alpha(\vec{r})$	reaction probabilities on surfaces
$\beta_{ij}(\vec{r})$	probability of species i incident on surface producing species j	$\Phi_s(\vec{r}, \phi)$	Electrostatic potential (V)

Table 3.1: Symbol convention used in the HPEM modules shown in figure 3.1

plasma phenomena and conditions that require simulation. In all cases the FKPM solves for conservation of mass but in the form shown in equation 3.5 where a flux term and a collisional rate term are included.

$$\frac{\partial n_{i,e}}{\partial t} = -\vec{\nabla}\vec{\phi}_{i,e} + \sum_j n_{i,e} n_j k_{(i,e)j} \tag{3.5}$$

There are multiple ways in which the flux term in equation 3.5 can be determined for the electrons. All of the simulations within this work have been done in a low-pressure regime of < 10 Pa. In this region there is known to be significant amounts of non-local electron heating in CCP sources [53]. This is a weakness of a fluid based approach and thus a Monte-Carlo scheme is used to give accurate results. How this is done is discussed later in this section. For the ions a fluid approach is still appropriate and the full momentum equation is used as

shown in equation 3.6.

$$\begin{aligned}\frac{\partial\vec{\phi_i}}{\partial t} =& -\frac{1}{m_i}\vec{\nabla}(n_i k_b T_i) + \frac{q_i}{m_i} n_i \vec{E} - \vec{\nabla}\cdot(n_i\vec{u}_i\vec{u}_i) \\ & - \sum_j \frac{m_j}{m_i + m_j} n_i n_j (\vec{u}_i - \vec{u}_j)\nu_{ij} + D_{ij}\end{aligned} \tag{3.6}$$

Here j is any second species and D accounts for momentum changes from collisions where the species identities change due to chemical reactions. ν_{ij} is the collision frequency and k_{ij} corresponds to the heavy particle rate coefficient between species i and j. m refers to the mass of the species resulting in $m_{ij}/m_i + m_j$ as the reduced mass of the two reacting species where $m_{ij} = m_i \times m_j$. $\vec{u}$ is velocity. The momentum equation takes the following form in the case of neutrals where there is no charge term but a viscosity tensor, $\overleftrightarrow{\nu_n}$, which takes into account the neutral gas flow.

$$\begin{aligned}\frac{\partial\vec{\phi_n}}{\partial t} =& -\frac{1}{m_n}\vec{\nabla}(n_n k_b T_n) - \vec{\nabla}\cdot(n_n\vec{u}_n\vec{u}_n) \\ & - \vec{\nabla}\cdot\overleftrightarrow{\nu_n} - \sum_j \frac{m_j}{m_n + m_j} n_n n_j (\vec{u}_n - \vec{u}_j)\nu_{nj} + D_{nj}\end{aligned} \tag{3.7}$$

A term is included in both equations which describes the momentum changes due to spatial variations in the fluid velocity, $\vec{\nabla}\cdot(n\vec{u}\vec{u})$. Each equation is also differentiated with respect to time. This is important in the low-pressure regimes on which this work is focussed as the collision frequency drops and the mean velocity a particle may reach before a collision increases. It is therefore necessary to take into account the temporal and spatial velocity gradients.

Energy conservation is done using the full energy equation, which is an expansion of equation 3.3 and is shown here for ions:

$$\begin{aligned}\frac{\partial(n_i c_i T_i)}{\partial t} =& \vec{\nabla}\kappa_i\vec{\nabla}T_i - p_i\vec{\nabla}\vec{u}_i - \vec{\nabla}(n_i\vec{u}_i c_i T_i) + \frac{n_i q_i^2}{m_i\nu_i}E_S^2 \\ & + \sum_j 3\frac{m_{ij}}{m_i + m_j} n_i n_j k_{ij} k_b (T_j - T_i) \\ & \pm \sum_j 3 n_i n_j k_{ij} k_b T_j\end{aligned} \tag{3.8}$$

In the above equation κ_i is the thermal conductivity, c_i is the heat capacity of the ion fluid, and ν_i is the total collisional momentum transfer frequency. In order the terms of

this equation refer to conduction, compressive heating, convection, heating by the electric field, heating through elastic collisions, and heating through inelastic collisions. Similarly the following equation is used for neutral particles:

$$\begin{aligned}\frac{\partial(n_n c_n T_n)}{\partial t} =& \vec{\nabla}\kappa_n\vec{\nabla}T_n - p_n\vec{\nabla}\vec{u}_n - \vec{\nabla}(n_n\vec{u}_n c_n T_n) \\ &+ \sum_j 3\frac{m_{nj}}{m_n + m_j} n_n n_j k_{nj} k_b (T_j - T_n) \\ &\pm \sum_j 3 n_n n_j k_{nj} k_b T_j\end{aligned} \tag{3.9}$$

As previously mentioned; in the pressure regime < 10 Pa there is a significant amount of non-local electron heating and thus a fluid momentum equation is insufficient [53, 54]. In order to effectively model this the electron Monte-Carlo Simulation (eMCS) in the EETM is used for electrons. This approach is as described in section 3.1.1, whereby pseudo particles are released from random numeric cells and their paths integrated in the electric fields produced by the FKPM. The pseudo particles are distributed in space according to the electron density, which is also generated by the FKPM. Electron collision rates are determined using inputs from the gas phase chemistry file and a time step that is based on calculated collision rate is randomly assigned. The pseudo particle is then integrated through that time step and the collision is stochastically determined to have occurred or not. If the collision is determined to have not occurred then the particle repeats the process through another time step. If the collision is determined to have occurred then the collision type and scattering angle are again randomly assigned. Over a number of RF cycles statistics on this process are gathered and an Electron Energy Distribution Function (EEDF) is output for each location. From this the electron impact rate and transport coefficients are calculated and passed back to the FKPM.

The solution of Poisson's equation closes the fluid equations, but solving 3.4 as it is would need to be done on a time step in order of the dielectric relaxation time. This could be as small as picoseconds which makes it computationally very expensive. The solution to this is to make an approximate prediction for densities of species at times in the future, which allows for larger time steps to be taken. This is done by recording recent historical values of fluxes and source functions which can then be numerically derived. Poisson's equation must

also include the surface interactions as

$$-\vec{\nabla}\cdot\epsilon\vec{\nabla}\Phi_s(t)=\sum_j q_j n_i(t+\Delta t)+\rho_s(t) \tag{3.10}$$

where ρ_s is the charge density within the surrounding materials.

$$\frac{d\rho_s(t)}{dt}=-\vec{\nabla}\cdot\left(\sum_j q_j\phi_{si}-\sigma_m\vec{\nabla}\Phi_s\right) \tag{3.11}$$

In this equation σ_m is the conductivity of materials facing the plasma. The two terms within the brackets represent the flux of charged species into the plasma facing materials and the current density within them. Then the prediction for densities in the future can be made as follows:

$$n(t+\Delta t)=n(t)+\Delta t\left(-\vec{\nabla}\cdot\left(\phi(t)+\delta t\frac{d\phi(t)}{dt}\right)+S(t)+\delta t\frac{dS(t)}{dt}\right) \tag{3.12}$$

The $d\phi(t)/dt$ and $dS(t)/dt$ terms are derivations from previous fluxes and source terms and, as with most processes within HPEM, this process is iterated upon until convergence is reached. The choices made here have been done so in order to output the most accurate physics possible, as the computing resources available have not limited this study with the computing time being reasonable. Further information and explanations of these processes, and others, can be found in [48].

Once convergence is reached with the multiple iterations of the above processes within the FKPM and EETM, the next step is the PCMCM. This takes the species source functions and the electric fields from the FKPM and conducts a similar method to that carried out by the eMCS and produces IEDFs. The IEDFs can be chosen to be calculated on any surface in contact with the plasma. Once again pseudo particles of the ions and neutrals are created within the mesh of the bulk plasma. Their spatial position is weighted by the source functions from the FKPM and their trajectories integrated through the electric field from the FKPM. Surface collisions are dealt with through interaction with the SKM. The collision frequency of a pseudo particle is, much like the eMCS, stochastically determined but based on the total collision frequency for all possible collisions. The rate coefficients for elastic heavy-particle collisions are calculated as hard-sphere collisions using Lennard-Jones parameters [55]. Much like the eMCS, the collisions are randomly determined to have happened or not, and the iteration is complete once all of the pseudo particles are exhausted

through losses to gas-phase or surface interactions. The incident angle and ion energy of pseudo particle collisions on surfaces data is being gathered for is recorded.

The final module used in this work is the SKM, which models the plasma-surface interface. In the case of surfaces that do not etch, the interactions are set simply where any wall interaction results in a neutralisation of the ion and reflection. For the surface for which etching reactions do take place, the surface sites are set to be chosen materials with a specific species coverage. This involves at least two materials with one as a base material, which has infinite depth, and a material in layers on top. It is this top material for which etching rates are calculated. Fluxes are then taken from the FKPM and the PCMCM which are used with a set of surface reaction mechanisms, of the form of equation 3.13, to calculate the number of populated sites and the thickness of the overlaying material with time.

$$A_g + B_s \xrightarrow{k_i} C_s + D_g + E_g \tag{3.13}$$

Where the subscripts g and s denote gas and surface phase species respectively. k_i is the reaction probability. After a specified length of time, long enough for a steady state to be achieved, the resulting coefficients α (the reaction probabilities on surfaces) and β_{ij} (the probability of species i incident on a surface producing species j) are fed back into the FKPM to be used as fixed-boundary conditions until the next call to the SKM. At this point the etching or deposition rates are recorded based on the surface coverage and reactive fluxes. The processes are further described and the SKM input reactions are given in chapter 3.2.4. A detailed explanation of the processes executed by this module can be found in [56, 57].

3.2.2 Model geometries

As a 2D code HPEM requires a 2D model geometry with three main geometries used in this work. The GEC cell geometry is based on the device used experimentally at York and is show in figure 3.2. The B-field chamber geometry is based on the device used experimentally in Basel by Moser, is shown in figure 3.3 and discussed in 6.1. Although referred to as the B-field geometry there is no simulation work presented, or experimental work compared with, that uses the magnetic fields. These geometries allow for comparison of the simulation with experiment, which will be discussed in the following chapters. A further simple geometry for ITER-relevant work is also used in four slight variations which is shown in figure 3.4 and

discussed in chapter 6. In order to reduce the computation time, HPEM utilises a cylindrical coordinate system with the axis of symmetry on the left hand side, shown as a dotted line in both figures. All geometries include a section referred to as the "wafer", which is the area of material defined as the deposit on the surface of the electrode. The term "wafer" is used for this area; there is no actual wafer. In the figures this wafer may appear to have a specific thickness but this is merely a single-mesh cell width from defining the geometry. The actual thickness of this wafer for the purpose of etching is input into the SKM and its material properties are input into the FKPM. The gas inlet and outlet in each geometry is an area of the metallic wall, defined as such, with the inlet having a set flow rate of gas set and the outlet maintaining a fixed pressure during the simulation. The positioning of these ports is not an exact copy of the reactors being modelled. However, the limited flow rates in both simulation and experiment means the gas flow will have negligible, if any, effect on the dynamics of the plasma and the validity of the comparison.

In these geometries there is no specific grounded electrode which is analogous to the experimental geometries and in the implementation of this method into ITER. This is unusual for most CCP experiments, where the area difference between the grounded and the powered electrode is used to control the bias voltage (as discussed in section 2.3.1.3). In this case the ground of the system is provided by the chamber walls, which means that the area of the powered electrode is much smaller than the grounded area. This gives rise to the maximum bias available, whereby nearly all of the RF potential is corrected by the powered electrode sheath, and thus gives the maximum ion energies.

3.2.3 Gas phase chemistry

ITER will have a tungsten divertor and beryllium walls. Tungsten is used for its low erosion rate under high neutral flux, and beryllium is used as a low-Z material and oxygen absorber, which improves plasma performance [58]. Both of these materials will be deposited on plasma facing mirrors during device operation, with tungsten being deposited mainly on mirrors in or around the divertor. As tungsten is resistant to erosion it is unlikely that large amounts will be deposited; $< 7.0 \times 10^{16}$ atoms cm^{-2} were found on mirrors in JET after a campaign with ITER like wall [9]. For this reason, coupled with a lack of experimental data, it has not been included in this work.

Beryllium is a low-Z material that will be the main deposition on first mirrors within

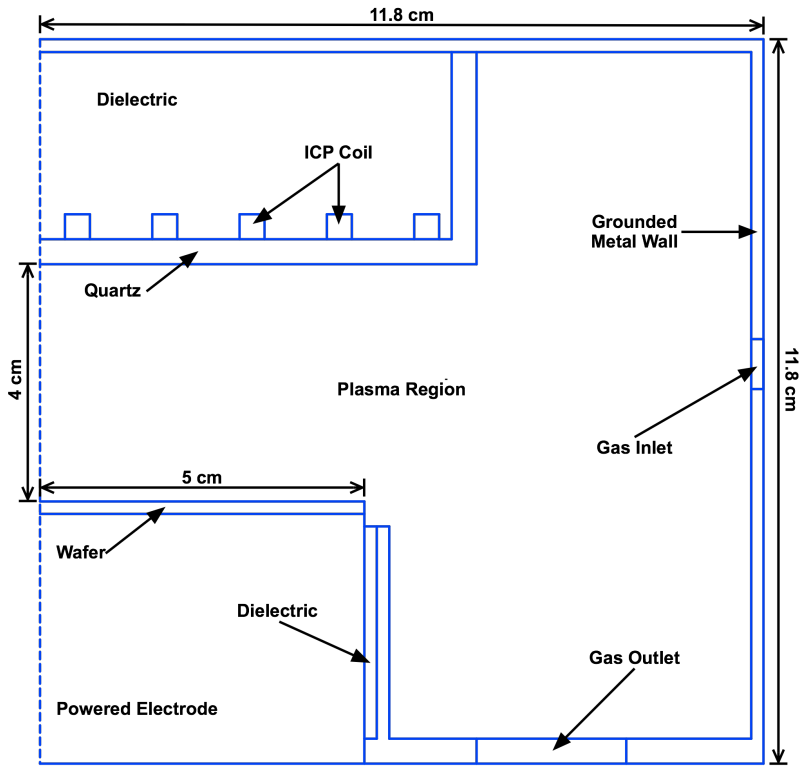

Figure 3.2: GEC geometry used in HPEM

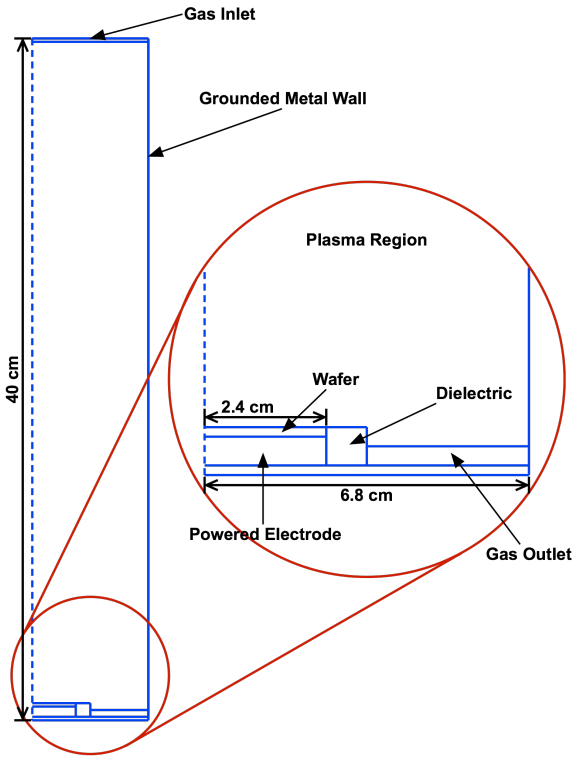

Figure 3.3: B-field geometry used with HPEM

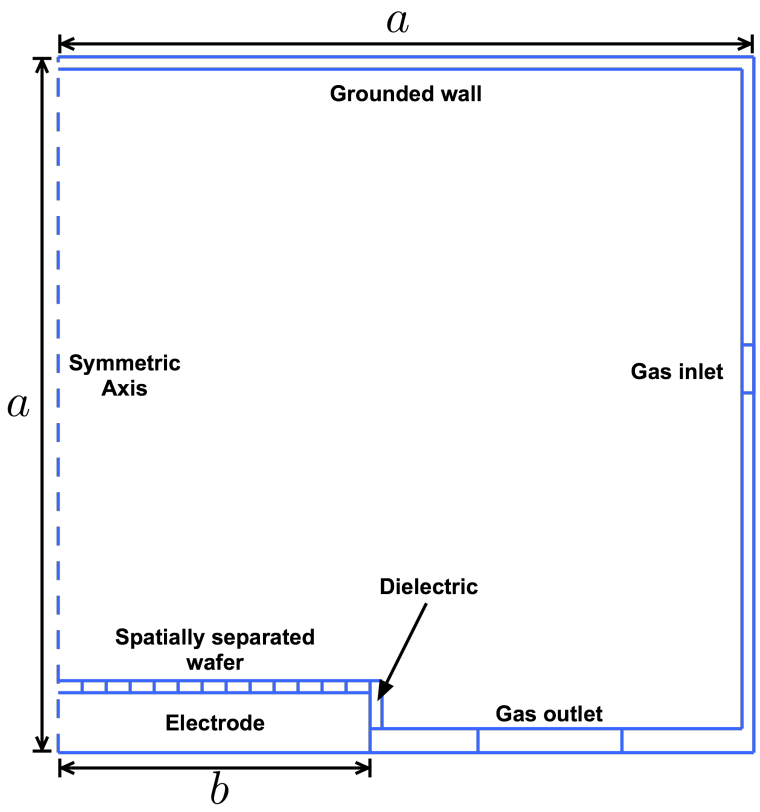

Figure 3.4: A simplified geometry used with HPEM. The height and width (a) are varied between simulations and are given in table 6.2 in a later section, the schematic shown is "geometry 1" as it shares its height and radius with the GEC geometry. Length b remains at 5.0 $\pm$ 0.6 cm for each simulation.

ITER. It is also toxic and cannot be used in many laboratories around the world, so experiments involving it are scarce. The majority of work in the field is being carried out using aluminium as a proxy. Marot et al. have shown that the similar electronegativity of both materials causes similar oxides and hydrides to form [17]. There is extremely limited experimental data available for beryllium sputtering rates as a result of argon ion bombardment, and even less for beryllium oxide. However it is known that in other gasses, such as deuterium, their threshold energies for sputtering (Be = 10 eV, BeO = 29 eV) are substantially lower than those for aluminium and aluminium oxide (Al = 36 eV, Al_2O_3 = 66 eV) [59]. In either case the sputtered material will be placed into the gas phase and a reaction mechanism must be available. For the majority of this work an argon, oxygen, and aluminium gas chemistry will be utilised, as the reactions are readily available in published work. This is not true for an argon, oxygen, and beryllium, where no full gas phase chemistry exists for beryllium. The following chapters will not therefore include beryllium, but it is later

discussed in chapter 7. The full gas chemistry used in the majority of this work is shown in table 3.2. The reaction set was provided by Mark Kushner and the set has been published and validated, both together and separately, in works such as [60–63]. It is important to point out that the Al and O are not input into the system via the inlet ports; a small amount starts within the reactor, as all species must have an initial mole fraction (10^{-7}) in the input file. These small initial amounts may remain in the system or may be swept out by the gas flow, but no more is added until the SKM is utilised to sputter the products from the surface.

Species:[a]		
Ar, $Ar(1s_5)$, $Ar(1s_4)$, $Ar(1s_3)$, $Ar(1s_2)$, $Ar(4p)$, $Ar(4d)$, Ar^+,Ar_2, Ar_2^*, Ar_2^+, O, O^+, O^-, O^*, $O(1s)$, O_2, O_{2V}, O_2^+, O_2^*, $O_2(^1\Delta)$, O_2^-, O_3, O_3^-, Al, Al^*, Al^{**}, Al^+, e		
Reaction	Rate coefficient[b]	Ref.
$e + Ar \leftrightarrow Ar + e$	$f\epsilon$	[64]
$e + Ar \leftrightarrow Ar(1s_5) + e$	$f\epsilon$	[65]
$e + Ar \leftrightarrow Ar(1s_4) + e$	$f\epsilon$	[65]
$e + Ar \leftrightarrow Ar(1s_3) + e$	$f\epsilon$	[65]
$e + Ar \leftrightarrow Ar(1s_2) + e$	$f\epsilon$	[65]
$e + Ar \leftrightarrow Ar(4p) + e$	$f\epsilon$	[65]
$e + Ar \leftrightarrow Ar(4d) + e$	$f\epsilon$	[65]
$e + Ar \rightarrow Ar^+ + e + e$	$f\epsilon$	[66]
$e + Ar(1s_5) \leftrightarrow Ar(1s_4) + e$	$f\epsilon$	[67]
$e + Ar(1s_5) \leftrightarrow Ar(1s_3) + e$	$f\epsilon$	[67]
$e + Ar(1s_5) \leftrightarrow Ar(1s_2) + e$	$f\epsilon$	[67]
$e + Ar(1s_5) \leftrightarrow Ar(4p) + e$	$f\epsilon$	[68]
$e + Ar(1s_5) \leftrightarrow Ar(4d) + e$	$f\epsilon$	[68]
$e + Ar(1s_5) \rightarrow Ar^+ + e + e$	$f\epsilon$	[69]
$e + Ar(1s_4) \leftrightarrow Ar(1s_3) + e$	$f\epsilon$	[67]
$e + Ar(1s_4) \leftrightarrow Ar(1s_2) + e$	$f\epsilon$	[67]
$e + Ar(1s_4) \leftrightarrow Ar(4p) + e$	$f\epsilon$	[68]
$e + Ar(1s_4) \leftrightarrow Ar(4d) + e$	$f\epsilon$	[68]
$e + Ar(1s_4) \rightarrow Ar^+ + e + e$	$f\epsilon$	[69]
$e + Ar(1s_3) \leftrightarrow Ar(1s_2) + e$	$f\epsilon$	[67]

$e + Ar(1s_3) \leftrightarrow Ar(4p) + e$	$f\epsilon$	[68]
$e + Ar(1s_3) \leftrightarrow Ar(4d) + e$	$f\epsilon$	[68]
$e + Ar(1s_3) \leftrightarrow Ar^+ + e + e$	$f\epsilon$	[69]
$e + Ar(1s_2) \leftrightarrow Ar(4p) + e$	$f\epsilon$	[68]
$e + Ar(1s_2) \leftrightarrow Ar(4d) + e$	$f\epsilon$	[68]
$e + Ar(1s_2) \rightarrow Ar^+ + e + e$	$f\epsilon$	[69]
$e + Ar(4p) \leftrightarrow Ar(4d) + e$	$f\epsilon$	[68]
$e + Ar(4p) \rightarrow Ar^+ + e + e$	$f\epsilon$	[69]
$e + Ar(4d) \rightarrow Ar^+ + e + e$	$f\epsilon$	[69]
$e + Ar^+ \rightarrow Ar(1s_5)$	$f\epsilon$	[63]
$e + Ar_2^* \rightarrow Ar_2^+ + e + e$	$9.0 \times 10^{-8} T_e^{-0.7} exp(-3.66/T_e)$	[70][c]
$e + Ar_2^* \rightarrow Ar + Ar + e$	1×10^{-7}	[70][c]
$e + Ar_2^+ \rightarrow Ar(1s_5) + Ar$	$2.69 \times 10^{-8} T_e^{-0.67}$	[71]
$e + Ar_2^+ \rightarrow Ar + Ar$	$2.69 \times 10^{-8} T_e^{-0.67}$	[71]
$e + O_2 \rightarrow O_2 + e$	$f\epsilon$	[72]
$e + O_2 \rightarrow O^- + O$	$f\epsilon$	[72]
$e + O_2 \leftrightarrow O_2^* + e$	$f\epsilon$	[72]
$e + O_2 \leftrightarrow O_2(^1\Delta) + e$	$f\epsilon$	[72]
$e + O_2 \rightarrow O + O + e$	$f\epsilon$	[72]
$e + O_2 \rightarrow O_2^+ + e + e$	$f\epsilon$	[72]
$e + O_2 \rightarrow O^+ + O + e + e$	$f\epsilon$	[73]
$e + O_2 \rightarrow O_{2V} + e$	$f\epsilon$	[72]
$e + O_{2V} \rightarrow O_{2V} + e$	$f\epsilon$	[72]
$e + O_{2V} \rightarrow O^- + O$	$f\epsilon$	[72]
$e + O_{2V} \rightarrow O_2 + e$	$f\epsilon$	[72]
$e + O_{2V} \leftrightarrow O_2^* + e$	$f\epsilon$	[72]
$e + O_{2V} \leftrightarrow O_2(^1\Delta) + e$	$f\epsilon$	[72]
$e + O_{2V} \rightarrow O + O + e$	$f\epsilon$	[72]
$e + O_{2V} \rightarrow O_2^+ + e + e$	$f\epsilon$	[72]
$e + O_{2V} \rightarrow O^+ + O + e + e$	$f\epsilon$	[72]
$e + O_2^* \rightarrow O_2^* + e$	$f\epsilon$	[74]
$e + O_2^* \rightarrow O^- + O$	$f\epsilon$	[75]

$e + O_2^* \leftrightarrow O_2(^1\Delta) + e$	$f\epsilon$	[76]
$e + O_2^* \rightarrow O + O + e$	$f\epsilon$	[72]
$e + O_2^* \rightarrow O_2^+ + e + e$	$f\epsilon$	[72]
$e + O_2^* \rightarrow O^+ + O + e + e$	$f\epsilon$	[72]
$e + O_2(^1\Delta) \rightarrow O_2(^1\Delta) + e$	$f\epsilon$	[74]
$e + O_2(^1\Delta) \rightarrow O^- + O$	$f\epsilon$	[72]
$e + O_2(^1\Delta) \rightarrow O + O + e$	$f\epsilon$	[72]
$e + O_2(^1\Delta) \rightarrow O_2^+ + e + e$	$f\epsilon$	[72]
$e + O_2(^1\Delta) \rightarrow O^+ + O + e + e$	$f\epsilon$	[72]
$e + O \rightarrow O + e$	$f\epsilon$	[77]
$e + O \leftrightarrow O^* + e$	$f\epsilon$	[78]
$e + O \leftrightarrow O(1s) + e$	$f\epsilon$	[78]
$e + O \rightarrow O^+ + e + e$	$f\epsilon$	[78]
$e + O^* \rightarrow O^* + e$	$f\epsilon$	[78]
$e + O^* \rightarrow O^+ + e + e$	$f\epsilon$	[78]
$e + O(1s) \rightarrow O(1s) + e$	$f\epsilon$	[79]
$e + O(1s) \rightarrow O^+ + e + e$	$f\epsilon$	[79]
$e + O_3 \rightarrow O_3 + e$	$f\epsilon$	[80]
$e + O_3 \rightarrow O^- + O_2$	$f\epsilon$	[81]
$e + O_3 \rightarrow O_2^- + O$	$f\epsilon$	[82]
$e + O_3 \rightarrow O_2 + O + e$	$f\epsilon$	[82]
$e + O_3 \rightarrow O_2^+ + O + e + e$	$f\epsilon$	[82]
$e + O_3 \rightarrow O^+ + O^- + O + e$	$f\epsilon$	[82]
$e + O_2^+ \rightarrow O + O$	$f\epsilon$	[72]
$e + O^+ \rightarrow O^*$	$5.3 \times 10^{-12} T_e^{-0.5}$	[83]
$e + O_2^- \rightarrow O_2 + e + e$	$f\epsilon$	[84]
$e + O^- \rightarrow O + e + e$	$2 \times 10^{-18} T_e^{-0.5} exp^{-3.4/T_e}$	[85]
$e + e + Ar^+ \rightarrow Ar(1s_5) + e$	$5.12 \times 10^{-27} T_e^{-4.5} cm^6 s^{-1}$	[83]
$e + e + O^+ \rightarrow O^* + e$	$5.12 \times 10^{-27} T_e^{-4.5} cm^6 s^{-1}$	[83]
$e + O_2 + M \rightarrow O_2^- + M$	$f\epsilon$	[83]
$e + O_2^* + M \rightarrow O_2^- + M$	$f\epsilon$	[83]
$e + Al \rightarrow Al^* + e$	$f\epsilon$	[63]

$e + Al \rightarrow Al^+ + e + e$	$f\epsilon$	[63]
$e + Al^* \rightarrow Al + e$	$f\epsilon$	[63]
$e + Al^* \rightarrow Al^{**} + e$	$f\epsilon$	[63]
$e + Al^* \rightarrow Al^+ + e + e$	$f\epsilon$	[63]
$e + Al^{**} \rightarrow Al^+ + e + e$	$f\epsilon$	[63]
$Ar_2^* \rightarrow Ar + Ar$	$6 \times 10^7 s^{-1}$	[70][c]
$Ar(1s_4) \rightarrow Ar$	$1.2 \times 10^8 s^{-1}$	[86]
$Ar(1s_2) \rightarrow Ar$	$5.1 \times 10^8 s^{-1}$	[86]
$Ar(4p) \rightarrow Ar(1s_5)$	$1.6 \times 10^7 s^{-1}$	[87]
$Ar(4p) \rightarrow Ar(1s_4)$	$9.3 \times 10^7 s^{-1}$	[87]
$Ar(4p) \rightarrow Ar(1s_3)$	$1 \times 10^7 s^{-1}$	[87]
$Ar(4p) \rightarrow Ar(1s_2)$	$8.5 \times 10^7 s^{-1}$	[87]
$Ar(4d) \rightarrow Ar(1s_5)$	$2 \times 10^5 s^{-1}$	[87]
$Ar(4d) \rightarrow Ar(1s_4)$	$2 \times 10^5 s^{-1}$	[87]
$Ar(4d) \rightarrow Ar(1s_3)$	$2 \times 10^5 s^{-1}$	[87]
$Ar(4d) \rightarrow Ar(1s_2)$	$2 \times 10^5 s^{-1}$	[87]
$Ar(4d) \rightarrow Ar(4p)$	$1 \times 10^7 s^{-1}$	[87]
$Ar(1s_5) + M \rightarrow Ar(1s_4) + M$	$1.5 \times 10^{-15} T_n^{0.5} exp(-881/T_g)$	[87]
$Ar(1s_4) + M \rightarrow Ar(1s_5) + M$	$2.5 \times 10^{-15} T_n^{0.5}$	[87]
$Ar(1s_5) + M \rightarrow Ar(1s_3) + M$	$0.5 \times 10^{-15} T_n^{0.5} exp(-2029/T_g)$	[87]
$Ar(1s_3) + M \rightarrow Ar(1s_5) + M$	$2.5 \times 10^{-15} T_n^{0.5}$	[87]
$Ar(1s_5) + M \rightarrow Ar(1s_2) + M$	$1.5 \times 10^{-15} T_n^{0.5} exp(-3246/T_g)$	[87]
$Ar(1s_2) + M \rightarrow Ar(1s_5) + M$	$2.5 \times 10^{-15} T_n^{0.5}$	[87]
$Ar(1s_4) + M \rightarrow Ar(1s_3) + M$	$0.83 \times 10^{-15} T_n^{0.5} exp(-1148/T_g)$	[87]
$Ar(1s_3) + M \rightarrow Ar(1s_4) + M$	$2.5 \times 10^{-15} T_n^{0.5}$	[87]
$Ar(1s_4) + M \rightarrow Ar(1s_2) + M$	$2.5 \times 10^{-15} T_n^{0.5} exp(-2365/T_g)$	[87]
$Ar(1s_2) + M \rightarrow Ar(1s_4) + M$	$2.5 \times 10^{-15} T_n^{0.5}$	[87]
$Ar(1s_3) + M \rightarrow Ar(1s_2) + M$	$7.5 \times 10^{-15} T_n^{0.5} exp(-1217/T_g)$	[87]
$Ar(1s_2) + M \rightarrow Ar(1s_3) + M$	$2.5 \times 10^{-15} T_n^{0.5}$	[87]
$Ar(*) + Ar(*) \rightarrow Ar^+ + Ar + e$	$1.2 \times 10^{-9} T_n^{0.5}$	[87]
$Ar^* + Ar^* \rightarrow Ar_2^+ + e$	$5.7 \times 10^{-10} T_n^{0.5}$	[67] [c]
$Ar(4d) + Ar \rightarrow Ar_2^+ + e$	$1 \times 10^{-9} T_n^{0.5}$	[88]

$Ar_2^* + Ar_2^* \rightarrow Ar_2^+ + Ar + Ar + e$	$5 \times 10^{-10} T_n^{0.5}$	[70][c]
$Ar^* + O_2^* \rightarrow O_2^+ + Ar + e$	$1.2 \times 10^{-9} T_n^{0.5}$	[87][bc]
$Ar^* + O_2 \rightarrow O_2^+ + Ar + e$	$1.2 \times 10^{-9} T_n^{0.5}$	[87][bc]
$Ar^* + O \rightarrow O^+ + Ar + e$	$1.2 \times 10^{-9} T_n^{0.5}$	[87][bc]
$Ar^* + O^* \rightarrow O^+ + Ar + e$	$1.2 \times 10^{-9} T_n^{0.5}$	[87][bc]
$Ar_2^* + O_2(^1\Delta) \rightarrow O_2^+ + Ar + Ar + e$	$5 \times 10^{-10} T_n^{0.5}$	[70][bc]
$Ar_2^* + O(1s) \rightarrow O^+ + Ar + Ar + e$	$5 \times 10^{-10} T_n^{0.5}$	[70][bc]
$O^* + O_2 \rightarrow O + O_2(^1\Delta)$	$2.56 \times 10^{-11} exp(-67/T_g)$	[89]
$O^* + O_2 \rightarrow O + O_2^*$	$1.6 \times 10^{-12} exp(-67/T_g)$	[89]
$O^* + O_3 \rightarrow O_2 + O_2$	1.2×10^{-10}	[90]
$O^* + O_3 \rightarrow O_2 + O + O$	1.2×10^{-10}	[90]
$O + O_3 \rightarrow O_2 + O_2$	$8.71 \times 10^{-12} exp(-2113/T_g)$	[91]
$O + O_3 \rightarrow O_2^* + O_2$	$1 \times 10^{-11} exp(-2300/T_g)$	[92]
$O(1s) + O_2^* \rightarrow O + O_2$	1.1×10^{-10}	[93][e]
$O(1s) + O_2^* \rightarrow O^* + O_2(^1\Delta)$	2.9×10^{-11}	[93]
$O(1s) + O_2^* \rightarrow O + O + O$	3.2×10^{-11}	[93]
$O(1s) + O_3 \rightarrow O_2 + O_2$	5.8×10^{-10}	[94]
$O_2^* + O_2^* \rightarrow O_2 + O_2$	9×10^{-17}	[94, 95][e]
$O_2^* + O_2^* \rightarrow O_2(^1\Delta) + O_2$	9×10^{-17}	[94, 95][e]
$O_2^* + O_2 \rightarrow O + O_3$	2.95×10^{-21}	[96]
$O_2^* + O_{2V} \rightarrow O + O_3$	2.95×10^{-21}	[96]
$O_2^* + O_3 \rightarrow O_2 + O_2 + O$	$5.2 \times 10^{-11} exp(2840/T_g)$	[92]
$O_2(^1\Delta) + O_2(^1\Delta) \rightarrow O_2^* + O_2$	$3.6 \times 10^{-17} T_n^{0.5}$	[89]
$O_2(^1\Delta) + O_3 \rightarrow O + O_2 + O_2$	1.5×10^{-11}	[92]
$O_2 + O_2 \rightarrow O_3 + O$	$1.11 \times 10^{-11} exp(49800/T_g)$	[97]
$O_3 + O_3 \rightarrow O_2 + O_2 + O_2$	$7.47 \times 10^{-12} exp(9310/T_g)$	[98]
$O_2 + M \rightarrow O + O + M$	$1.31 \times 10^{-10} exp(52740/T_g)$	[99]
$O_{2V} + M \rightarrow O + O + M$	$1.31 \times 10^{-10} exp(50422/T_g)$	[99][d]
$O_2^* + M \rightarrow O + O + M$	$1.31 \times 10^{-10} exp(41146/T_g)$	[99][d]
$O_2(^1\Delta) + M \rightarrow O + O + M$	$1.31 \times 10^{-10} exp(34190/T_g)$	[99][d]
$O_3 + M \rightarrow O_2 + O + M$	$7.17 \times 10^{-10} exp(11170/T_g)$	[99]

$Ar_2^* + M \rightarrow Ar(*) + Ar + M$	$1.31 \times 10^{-10} exp(348/T_g)$	$[99]^{cd}$
$O + O + M \rightarrow O_2 + M$	$5.25 \times 10^{-35} exp(-906/T_g)$	[91]
$O + O + M \rightarrow O_{2V} + M$	5.25×10^{-35}	$[91]^d$
$O + O + M \rightarrow O_2^* + M$	5.25×10^{-35}	$[91]^d$
$O + O + M \rightarrow O_2(^1\Delta) + M$	5.25×10^{-35}	$[91]^d$
$O + O_2 + M \rightarrow O_3 + M$	$5.25 \times 10^{-35} exp(855/T_g)$	[100]
$Ar(*) + Ar + M \rightarrow Ar_2^* + M$	$1.14 \times 10^{-32} T_n^{-1}$	$[70]^c$
$O_{2V} + M \rightarrow O_2 + M$	$1 \times 10^{-14} T_n^{0.5}$	$[89]^d$
$O_2 + M \rightarrow O_{2V} + M$	$1.5 \times 10^{-14} exp(2203/T_g)$	$[60]^f$
$O_2(^1\Delta) + M \rightarrow O_2^* + M$	$3.6 \times 10^{-17} T_n^{0.5}$	$[89]^d$
$O_2(^1\Delta) + M \rightarrow O_2 + M$	$4 \times 10^{-18} T_n^{0.5}$	$[89]^d$
$O_2^* + M \rightarrow O_2 + M$	$3 \times 10^{-18} exp(200/T_g)$	$[94]^d$
$O(1s) + M \rightarrow O^* + M$	$3.2 \times 10^{-12} exp(850/T_g)$	$[101]^d$
$O(1s) + M \rightarrow O + M$	$1.6 \times 10^{-12} exp(850/T_g)$	$[101]^d$
$O^* + M \rightarrow O + M$	4.8×10^{-12}	$[89]^d$
$Ar^+ + Ar \rightarrow Ar^+ + Ar$	$5.66 \times 10^{-10} T_n^{0.5}$	[102, 103]
$Ar^+ + O \rightarrow O^+ + Ar$	1×10^{-11}	[60]
$Ar^+ + O_2 \rightarrow O_2^+ + Ar$	5.1×10^{-11}	[104]
$Ar^+ + Ar_2^* \rightarrow Ar_2^+ + Ar$	1×10^{-11}	$[60]^c$
$Ar^+ + Ar + Ar \rightarrow Ar_2^+ + Ar$	$2.5 \times 10^{-31} T_n^{-1}$	[105]
$Ar_2^+ + Ar_2^* \rightarrow Ar_2^+ + Ar_2^*$	1×10^{-9}	$[60]^c$
$Ar_2^+ + O \rightarrow O^+ + Ar + Ar$	1×10^{-11}	[60]
$Ar_2^+ + O_2 \rightarrow O_2^+ + Ar + Ar$	5.1×10^{-11}	$[104]^d$
$O^+ + O \rightarrow O^+ + O$	$1 \times 10^{-9} T_n^{0.5}$	[95]
$O^+ + O_2 \rightarrow O_2^+ + O$	2×10^{-11}	[106]
$O^+ + Ar_2^* \rightarrow Ar_2^+ + O$	1×10^{-11}	$[60]^c$
$O^+ + O_3 \rightarrow O_2^+ + O_2$	1×10^{-10}	[93]
$O_2^+ + O_2 \rightarrow O_2^+ + O_2$	1×10^{-9}	[60]
$O_2^+ + Ar_2^* \rightarrow Ar_2^+ + O_2$	1×10^{-11}	$[60]^c$
$O^- + O_2(^1\Delta) \rightarrow O + O_2 + e$	$6.9 \times 10^{-10} T_n^{0.5}$	[93]
$O^- + O_2 \rightarrow O_2^- + O$	2.5×10^{-14}	[107]

$O^- + O_2 \rightarrow O_3 + e$	5×10^{-15}	[108]
$O^- + O_3 \rightarrow O_2 + O_2 + e$	2×10^{-14}	[108]
$O^- + O_3 \rightarrow O_3^- + O$	5.5×10^{-10}	[108]
$O^- + O_3 \rightarrow O_2^- + O_2$	1×10^{-11}	[108]
$O^- + O \rightarrow O_2 + e$	1.4×10^{-10}	[82]
$O^- + O_2^* \rightarrow O_3 + e$	3×10^{-10}	[82]
$O^- + O_2 + M \rightarrow O_3^- + M$	$1.1 \times 10^{-30} cm^6 s^{-1}$	[108]
$O_2^- + O \rightarrow O^- + O_2$	$1.5 \times 10^{-10} T_n^{0.5}$	[104]
$O_2^- + O \rightarrow O_3 + e$	$1.5 \times 10^{-10} T_n^{0.5}$	[104]
$O_2^- + O_2 \rightarrow O_3^- + O$	3×10^{-15}	[109]
$O_2^- + O_2^* \rightarrow e + O_2 + O_2$	2×10^{-10}	[110]
$O_2^- + O_3 \rightarrow O_3^- + O_2$	3.2×10^{-10}	[108]
$O_3^- + O \rightarrow O_2^- + O_2$	1×10^{-11}	[108]
$O_3^- + O \rightarrow O_2 + O_2 + e$	1.1×10^{-13}	[108]
$O^- + O_2^+ \rightarrow O + O_2^*$	2×10^{-7}	[95, 111, 112]
$O^- + O^+ \rightarrow O + O^*$	2×10^{-7}	[95, 111, 112]
$O^- + Ar^+ \rightarrow O + Ar(1s_5)$	1×10^{-7}	[95, 111, 112]
$O^- + Ar^+ \rightarrow O + Ar(1s_3)$	1×10^{-7}	[95, 111, 112]
$O^- + Ar_2^+ \rightarrow O + Ar + Ar$	2×10^{-7}	[95, 111, 112]
$O^- + O^+ + M \rightarrow O_2 + M$	1.2×10^{-25}	[113]
$O^- + O_2^+ + M \rightarrow O + O_2 + M$	$2 \times 10^{-25} T_n^{-2.5} cm^6 s^{-1}$	[113]
$O_3^- + O_2^+ \rightarrow O_3 + O_2^*$	2×10^{-7}	[95, 108, 111, 112]
$O_3^- + O^+ \rightarrow O_3 + O^*$	$1 \times 10^{-7} T_n^{-0.5}$	[95, 108, 111, 112]
$O_3^- + Ar^+ \rightarrow O_3 + Ar(1s_5)$	1×10^{-7}	[95, 111, 112]
$O_3^- + Ar^+ \rightarrow O_3 + Ar(1s_3)$	1×10^{-7}	[95, 111, 112]
$O_3^- + Ar_2^+ \rightarrow O_3 + Ar + Ar$	2×10^{-7}	[95, 111, 112]
$O_2^- + O_2^+ \rightarrow O_2 + O_2^*$	2×10^{-7}	[95, 111, 112]
$O_2^- + O^+ \rightarrow O_2 + O^*$	2×10^{-7}	[95, 111, 112]
$O_2^- + Ar^+ \rightarrow O_2 + Ar(1s_5)$	1×10^{-7}	[95, 111, 112]
$O_2^- + Ar^+ \rightarrow O_2 + Ar(1s_3)$	1×10^{-7}	[95, 111, 112]
$O_2^- + Ar_2^+ \rightarrow O_2 + Ar + Ar$	2×10^{-7}	[95, 111, 112]

$Al^* \rightarrow Al$	7.3×10^5	[63]
$Al^{**} \rightarrow Al$	1×10^3	[63]
$Al^{**} \rightarrow Al^*$	1×10^3	[63]
$Al^* + Al \rightarrow Al + Al$	1×10^{-12}	[63]
$Al^* + Al^* \rightarrow Al^* + Al$	1×10^{-12}	[63]
$Al^+ + Al \rightarrow Al + Al^+$	1×10^{-9}	[63]
$Al^+ + Al^* \rightarrow Al + Al^+$	1×10^{-9}	[63]
$Al^+ + Al^{**} \rightarrow Al + Al^+$	1×10^{-9}	[63]
$Al^* + Ar \rightarrow Al + Ar$	1×10^{-14}	[63]
$Ar(*) + Al \rightarrow Al^+ + Ar + e$	5.9×10^{-10}	[63]
$Ar(*) + Al^* \rightarrow Al^+ + Ar + e$	5.9×10^{-10}	[63]
$Ar(*) + Al^{**} \rightarrow Al^+ + Ar + e$	5.9×10^{-10}	[63]
$Ar^+ + Al \rightarrow Al^+ + Ar$	1×10^{-9}	[63]
$Ar^+ + Al^* \rightarrow Al^+ + Ar$	1×10^{-9}	[63]
$Ar^+ + Al^{**} \rightarrow Al^+ + Ar$	1×10^{-9}	[63]

[a] Lumped states with $Ar(4p)$ representing $Ar(4p, 3d, 5s, 5p)$ and $Ar(4d)$ representing $Ar(4d, 6s, Rydberg)$.
[b] Rate coefficients are in units of $cm^3 s^{-1}$ unless otherwise stated. $f\epsilon$ indicates that the rate coefficients have been calculated from the electron energy distribution within the eMCS. T_g is the gas temperature (K), T_n is the normalised gas temperature ($T_g/300K$), and T_e is the electron temperature (eV).
[c] These rates are lumped rates where $Ar(*)$ includes all excited states shown previously in the table and Ar_2^* is $Ar_2(^3\sum_u{}^+)$.
[d] Rate was estimated within the reference given using a similar reaction.
[e] Rate given by the reference. It assumes half branches to O_2 and half to $O_2(^1\Delta)$.
[f] Rate calculated within reference by detailed balance.

Table 3.2: Argon, oxygen, and aluminium gas phase reactions and rate coefficients

3.2.4 Plasma-surface chemistry

For the purpose of creating a plasma surface reaction chemistry only certain parameters need to be input. These are the reactions themselves of the form given in equation 3.13, the threshold energy of the process (E_{th}), a reference energy (E_{ref}) with a given probability (p_0), and an exponential (m). The ion energy (E) used in the reaction is fed from the FKPM and the PCMCM. To calculate the probability of a reaction occurring ($p(E)$) the following

equation is used, which is typical for this work and where the value for m is 0.5 [114]. The values of these variables and the reactions to which they apply are shown in table 3.3.

$$p(E) = p_0 \frac{E^m - E_{th}^m}{E_{ref}^m - E_{th}^m} \tag{3.14}$$

This is a very simplified process that was designed around sputtering of elemental targets, which is a very well-known process that has undergone extensive study [25]. When considering a multi-component surface the complexity of the situation increases and the knowledge is limited. Complicated linear cascade models rely on the surface binding energies of the involved elements, which have been under investigation but are always limited to specific compounds [115,116]. Often these models do not match experimental results for oxide films due to a lack of understanding of the process. Kubart *et al.* have even shown disagreements to exist between the etching rates measured through sputter experiments and the subsequent analysis of the surface by X-ray photoelectron spectroscopy (XPS) [117]. He suggests that the surface of the Al_2O_3 has the O preferentially sputtered from it leaving a very thin Al surface which cannot be detected. This gives an increased etching rate in comparison with expected values and which has been seen in the case of ZnO [118].

The SKM itself operates on a number of sites that represent one particle each, and not all surface chemistries can be modelled owing to this and other current limitations. These sites are given a specific surface density but this can only be of one type of particle (e.g. Al, O, or a particle representing Al_2O_3). Multiple elements or particles cannot initially share the surface. This is not such an issue if Al_2O_3 etches and deposits just as an element would as a whole, but this is not the case. The discussion in the previous paragraph suggests that the mechanism is preferential O etching, leaving an enriched Al surface, which then etches and leaves an Al_2O_3 surface to begin the process again. Then there is the further redeposition. This is a current stumbling block for experimental efforts in this work being carried out by Moser *et al.*, as build ups of re-deposited material are seen in different places depending on rotation of a mirror within a chamber [20]. With both etching and redeposition the amount of material within the system must be conserved. The reactions involved in the SKM are only ever two body reactions, with one being a surface site and one being a gas-phase particle. This is a limitation of the code, which makes it particularly difficult to model a compound with a 2:3 ratio of elements whilst maintaining material conservation.

For the above reasons the surface reaction mechanism is simplified to a 1:1 ratio of Al and O. The surface sites are initially populated with "AlO" which can etch either as a whole and output Al and O into the gas phase, or the O can etch preferentially and leave behind an Al surface. This Al surface can then be etched and expose the "AlO" site below it or it can take on another O and reform the "AlO" site. Similarly an Al may be re-deposited and undergo the same oxidation process. Each time a lower site is exposed through a reaction this counts as an etching step. The overall thickness of the film is input into the SKM using the known mono-layer thickness of Al_2O_3, and by specifying the number of layers. The thickness and conductivity of this layer, for the purpose of the plasma, is input separately into the FKPM.

Oxygen species in the plasma produced from the Al_2O_3 surface will not only oxidise Al on the surface but should also, if ions of sufficient energy, perform etching reactions. This is an area where published data is not available, owing to oxygen only being used as a background gas in sputtering experiments in order to produce an oxide surface; it is not used as a source of ions. It is also true that the amount of oxygen species in the gas phase will be minimal; from simulations of the plasma with 2 % O_2 in the feed gas the flux of any oxygen ions to the surface was less than 1 % of that of the background Ar. It is for this reason that oxygen ion sputtering reactions are not included in the surface chemistry.

Gas Species: $Ar_g, Ar_g^+, Ar_{2g}^+, O_g, O_g^+, O_{2g}^+, Al_g, Al_g^+$ Surface species: AlO_s, Al_s			
Reaction[a,b,c,d,e]	p_0	$E_{th}(eV)$	Ref.[f]
$Ar_g^+ + AlO_s \rightarrow Ar_g + Al_g + O_g + ET$	0.27[g]	50	[119–121]
$Ar_g^+ + AlO_s \rightarrow Al_s + Ar_g + O_g$	0.33[gh]	50	[119]
$Ar_g^+ + Al_s \rightarrow Ar_g + Al_g + ET$	0.8	29	[122, 123]
$Ar_{2g}^+ + AlO_s \rightarrow Ar_g + Ar_g + Al_g + O_g + ET$	0.27	50	[124]
$Ar_{2g}^+ + AlO_s \rightarrow Al_s + Ar_g + Ar_g + O_g$	0.33	50	[124]
$Ar_{2g}^+ + Al_s \rightarrow Ar_g + Ar_g + Al_g + ET$	0.8	29	[124]
$Al_g^+ + AlO_s \rightarrow Al_g + Al_g + O_g + ET$	0.01[i]	50	[125]
$Al_g^+ + AlO_s \rightarrow Al_s + Al_g + O_g$	0.01[i]	50	[125]
$Al_g^+ + Al_s \rightarrow Al_g + Al_g + ET$	0.5	10	[126]
$O_g^+ + Al_s \rightarrow AlO_s$	1	[j]	[127]
$O_{2g}^+ + Al_s \rightarrow AlO_s + O_g$	0.1	[j]	[128, 129]
$O_g + Al_s \rightarrow AlO_s$	1[i]		[127]
$Al_g + AlO_s \rightarrow Al_s + DEP$	0.5[i]		[130]
$Al_g^+ + AlO_s \rightarrow Al_s + DEP$	0.5[i]	[j]	[130]

[a] Subscript s and g denote surface site and gas phase species respectively.
[b] ET in the reaction represents an etching reaction that is used to calculate the etching rate. DEP in the reaction represents a deposition reaction which is used to calculate a deposition rate.
[c] Unless specified all ions neutralise on any surface and return as their neutral species.
[d] The sum of probabilities for any gas phase species on any surface site may not total 1 as the remainder will denote the probability of no reaction taking place.
[e] Gas phase species have units of flux ($cm^{-2}s^{-1}$). The initial surface site density for this work is $1 \times 10^{15} cm^{-2}$.
[f] References refer to the probability and the threshold energy used, rather than the reaction itself unless otherwise stated.
[g] Probability split between two processes.
[h] Calculated to give a total yield of 0.54 including a subsequent Al_s reaction. I.e. the referenced yield of 0.54 for Al_2O_3 requires both an O and an Al to leave the surface in two reactions in this reaction set.
[i] Estimated based off reference.
[j] Low-energy process, no low threshold energy for reaction to take place. The higher energy reaction will take precedence if the incoming particle is above the threshold energy.

Table 3.3: The surface chemistry used in the SKM within HPEM

Chapter 4

Experimental methods and deposition analysis

To model the plasma responsible for the deposition removal process there must first be some benchmarking of the code against experimental results. The Gaseous Electronics Conference (GEC) cell is a reference cell design that is used all over the world and is very well understood. It is therefore a perfect device to model due to the experimental data available with which to compare. However, etching of Al_2O_3 has not been done before in this chamber so it is important to investigate the process. To do that deposits are created and their structure and composition analysed within this chapter. The experimental devices and methods used in the following chapters are also presented.

The work carried out within this thesis has used Torr as the unit of pressure, due to this being the unit required as an input for HPEM. It is also widely used in the semi-conductor industry from which the etching literature is based. The conversion to Pascal has been given in previous chapters but will not be included in the remainder of the thesis. Only a few pressures are used and conversions between Torr and Pascal are given for these pressures in appendix A.

4.1 The GEC cell

At York deposition is carried out using a variation of the Pulsed laser Deposition (PLD) technique within a 6 arm CF160 vacuum chamber, which is shown in figure 4.1 and is based on a GEC reference cell [131]. As can be seen, the geometry of the chamber is the basis of

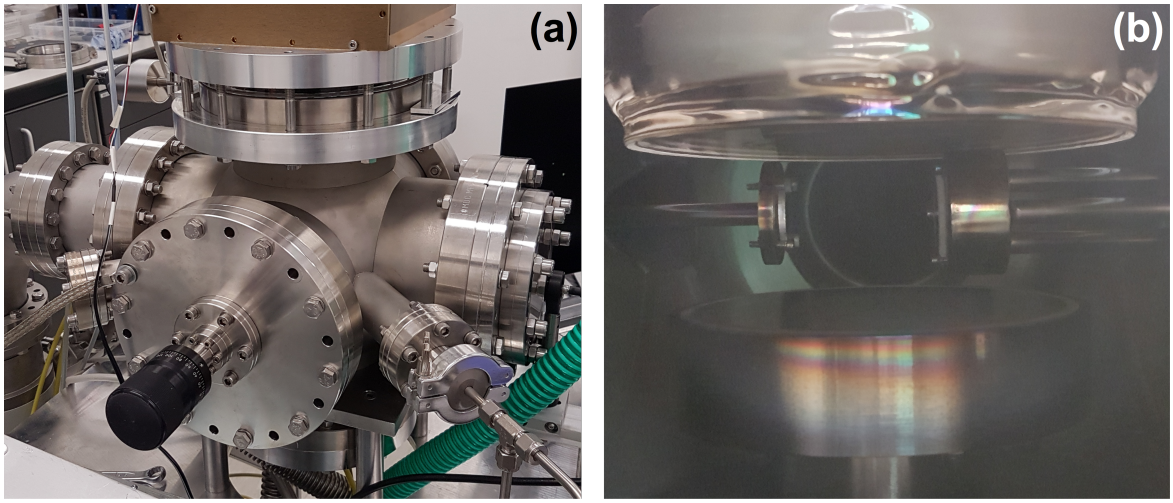

Figure 4.1: External (a) and internal (b) images of the GEC cell used in this work. The external image is taken from the gas line in with the black handle being the rotating target holder. The internal image shows that same holder on the left of the image and is the same orientation as the diagram in figure 4.2.

that of the model shown in figure 3.2, as it is the same chamber used to do the erosion work although in a different set up, which will be discussed in this chapter. The chamber has a base pressure of $\approx$ 11 mTorr using an Edwards nxDS 15i scroll pump; this can be reduced further with the attached turbo pump, however this is not used for either process. All gas flows are controlled by MKS Instruments thermal mass flow controllers which are calibrated for each gas using an MKS 247 meter. Specifics of each process are given in the following sections.

4.1.1 Deposition

Before deposition can begin the mirrors must be prepared. Stainless steel disks of 25 mm diameter were cut in the workshop from a 1 mm thick sheet using a plasma cutter, as opposed to traditional press cutting, in order to avoid bent disks. These disks were then hand sanded using wet sand paper in stages from 150 grit, to 300 grit, to 600 grit. They were then polished using Autoglym metal polish and a fibre cloth. This produced a mirrored surface and the polish residue was removed using isopropyl alcohol and a clean cloth. As no reflectivity measurements were taken during this process the quality of the mirrors was only visually inspected. As long as the surface is of good enough quality to be used with the thickness measurement device this is deemed to be experimentally viable.

Using the Plasma Enhanced Pulsed Laser Deposition (PE-PLD) experiment at York,

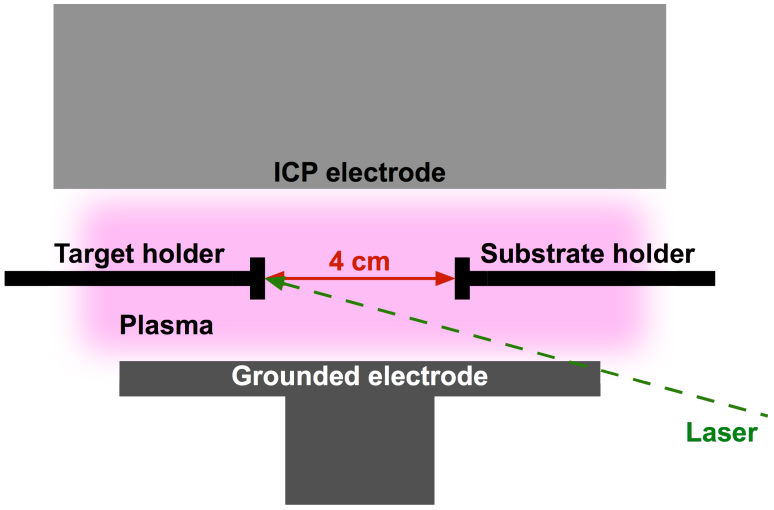

Figure 4.2: PE-PLD target and substrate configuration

deposits of Al_2O_3 have been made on these stainless steel mirrors. The PE-PLD process uses a laser to ablate a target surface, in this case aluminium, within an oxygen background plasma. The ablated atoms are ejected across the chamber towards a substrate and collect oxygen atoms along the way to deposit an oxide coating upon the substrate. The details of this process are not the focus of my work but have been recently published by Rossall [132]. The process is also described in detail in the thesis of Sudha Rajendiran [133]. The important points are covered here, in terms of reproduction of these specific results, but no further analysis will be given.

The plasma is key in this process. It is inductively coupled and pulsed such that the plasma is active during the laser ablation of the target. The ICP coil is 4 turns of copper at the top of the chamber with a 1 inch quartz shield between it and the inside of the chamber. It is run at a frequency of 13.56 MHz and 700 W input power using a 1 kW Advanced Energy Ceaser™ 1330 power supply through a impedance matching network. The oxygen is fed in to give a chamber pressure of 64 mTorr for this process. The sample is held 4 cm from the substrate, equidistant between the upper and lower electrodes, as shown in figure 4.2. The aluminium used is of 99.99 % purity and the holder can be rotated in order to spread the laser erosion around the face of the sample. Both the sample and the substrate are held secure by a series of screws and washers around their edges; the substrate holder is also water cooled. The laser is a 1064 nm Nd:YAG Continuum Minilite™which is run at its first harmonic of 532 nm, pulsed at a rate of 10 Hz for a 5 ns pulse length, with 35 mJ of total beam energy per pulse. The focal spot size on the target, after passing through a

Site	Atomic composition Al (%)	Atomic composition O (%)
1	39.44	60.56
2	38.88	61.12
3	39.46	60.54
4	39.37	60.63
5	39.04	60.96
Average	39.24 ± 0.26	60.76 ± 0.26

Table 4.1: EDX analysis results of Al_2O_3 deposit

focussing lens, is 1 mm in diameter. Timings of the pulsed operation are controlled using a digital delay generator in the following order: The ICP coil is powered to ignite the plasma, which typically reaches equilibrium within 1 μs [134]. The laser flash lamp is powered 8 ms after the plasma has been ignited, reaching peak energy after 150 μs, and the q-switch is triggered. The laser ablates the target and the ablated material travels across the chamber in under 2 ms [132, 133]. The plasma is then switched off and the process is held for 92 ms after which the series is repeated. The system therefore has a duty cycle of 10 %.

Thickness measurements of deposits are made using a Filmetrics F20 thin film analyser and the FILMeasure 8 software. This device shines light from 375 nm to 3000 nm from a tungsten-halogen bulb through a fibre-optic cable perpendicularly towards the surface. A spectrometer analyses the reflected light at the different wavelengths using a diffraction grating to disperse the light, and a linear photodiode array to take measurements. The software takes these measurements and compares them with calculated reflectance spectra to work out the thickness of the deposited material.

As can be seen from figure 4.3, the rate of deposition onto a stainless steel mirror substrate is linear at about 1.8 nm/min. An image comparing a clean disk with one with a 100 nm Al_2O_3 deposit is also shown. Energy-dispersive X-ray spectroscopy (EDX) has been used to analyse the deposited surface in order to determine its composition. Five sites on one deposit were measured under a 3 keV electron beam. These electrons displace inner shell electrons of atoms causing outer electrons to fall to the inner shell and release a photon, which is analysed. The results from this analysis are shown in table 4.1 and it can be seen that the atomic composition of the deposit is exactly Al_2O_3. This was performed on the JEOL 7800FPRIME scanning electron microscope using the attached X-ray detector and was analysed using the Pathfinder software.

Further composition measurements were taken using X-Ray Diffraction (XRD) with a

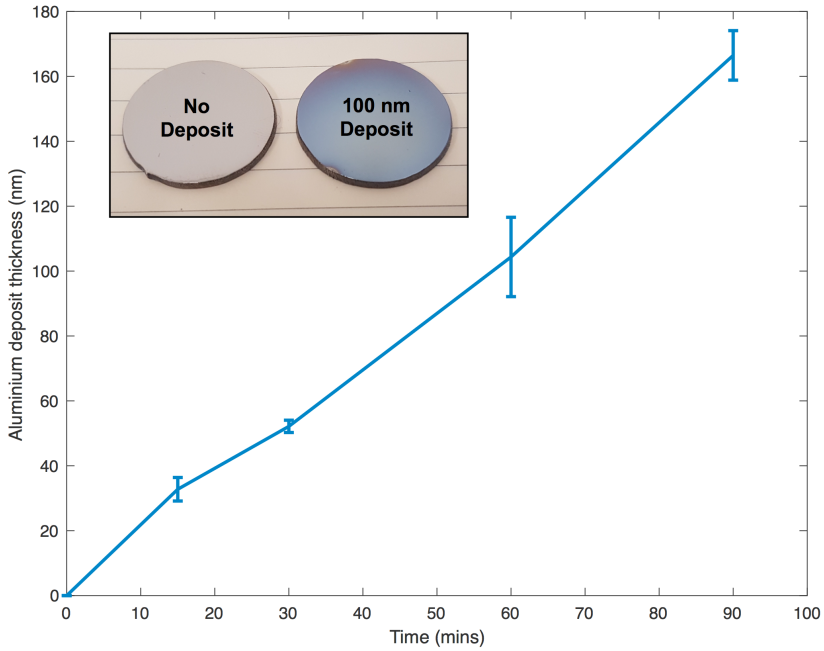

Figure 4.3: PE-PLD deposition rate of aluminium oxide onto a stainless steel mirror. A visual comparison of a mirror with no deposit and one with 100 nm of Al_2O_3 is also shown.

Rigaku Smartlab, which uses an X-ray beam diffracting within the crystal structure of a surface. A detector measures the interference patterns as a function of scattering angle and Bragg peaks can be identified. The raw scan shown in figure 4.4 has three fairly obvious peaks, however the counts per second are low and there is significant noise. With this deposition technique the structure of the deposited material mimics the structure of the substrate through the free energy of the deposited material being lower than that of the substrate [133]. As the Al_2O_3 is deposited on the surface it takes up the structure of the steel, which is typically of a body centred cubic structure, but the angle of these planes is unknown. This can leave the surface looking rough on the atomic scale, giving the deposited material an amorphous structure. By additionally scanning a steel mirror with no deposit and getting the same result, it is clear that we have an amorphous Al_2O_3 surface that stems from an amorphous steel substrate. It is known that PLD deposits have been shown to match the amorphous nature of deposits found within fusion devices, this result being no exception [135, 136].

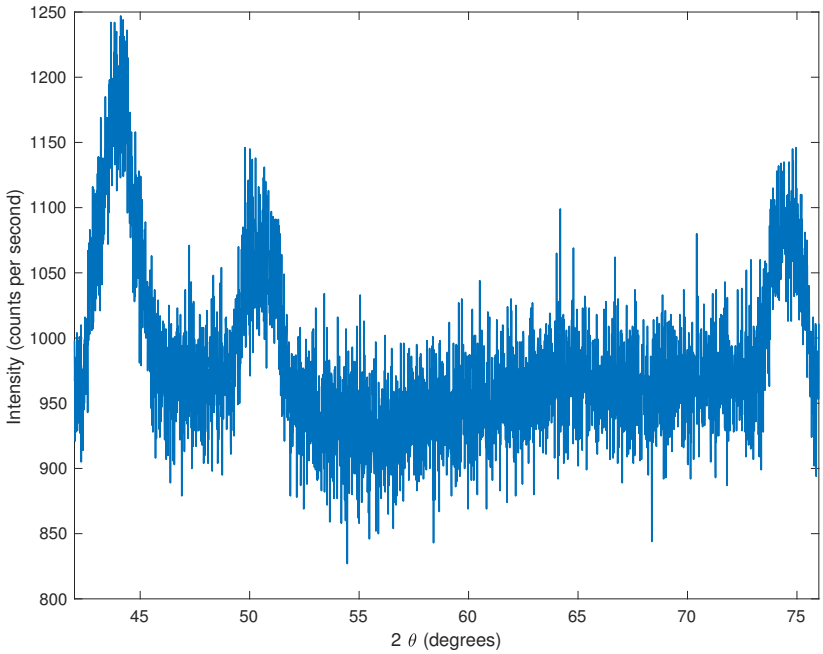

Figure 4.4: Raw XRD scan of 100 nm Al_2O_3 on stainless steel.

4.1.2 Deposition removal

By reconfiguring the chamber to power the lower electrode it can be run as a CCP reactor, as shown in figure 4.5. The steel mirror, with deposit, is then placed on this lower electrode. As discussed in section 2.2 the ions produced are attracted to the lower electrode and etch away the deposit. The switch from ICP to CCP involves swapping the cable from between the power supply and the ICP matching box and connecting it to the Advanced Energy Navio™ digital auto matching unit, which is in turn attached to the lower electrode. The lower electrode itself is 10 cm across and is surrounded by a 6 mm ring of PEEK which fully encloses it. This is subsequently held within a grounded stand and water cooling is supplied between the electrode and the PEEK housing on the back side. The water cooling allows the device to be run in continuous operation, thereby there is no requirement for a digital delay generator, so this is removed. The substrate holder is also removed, along with the flange it rests in, and is replaced with a door which allows for easier access for placing and removal of the steel mirrors. As thickness measurements cannot be made in situ the removal process is timed and the mirror removed at regular intervals in order to measure the deposit.

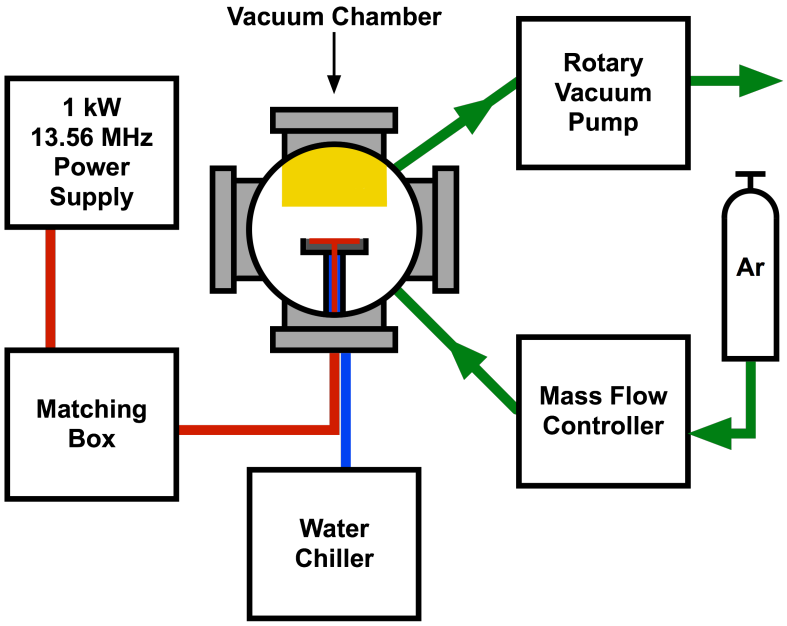

Figure 4.5: Diagram of the PLD GEC cell configured for deposition removal. The chamber is grounded.

4.2 Atmospheric-pressure plasma jet (APPJ)

In the initial phases of this investigation the APPJ was considered a viable deposition removal method, when carbon was still used as a first wall material. Some work on the hydrocarbon polypropylene, presented in chapter 8, was completed with the APPJ.

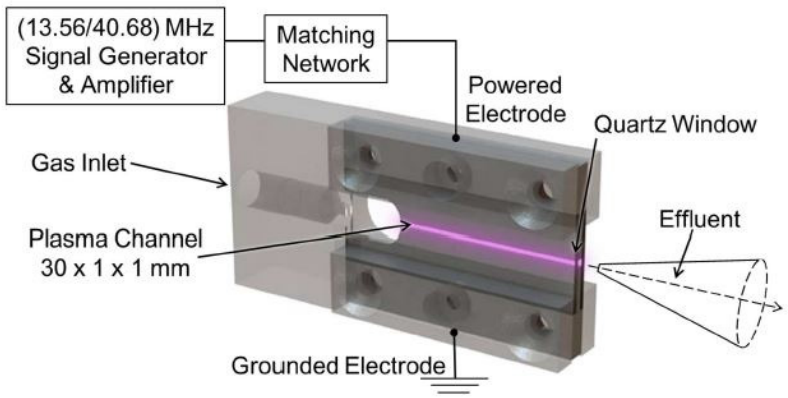

Figure 4.6: Schematic diagram of the APPJ used in this work.

There are many forms of APPJ but in general there are two types; those in which the field is parallel to the gas flow (linear-field); and those in which the field is perpendicular to the gas flow (cross-field). The APPJ that is used in chapter 8, shown in figures 4.6 and 4.7, has a 1 mm square channel through which a gas can be passed, and an electric field formed across it, and is thus cross-field. It was originally taken from the designs of Schulz-von der Gathen *et al.* [137, 138]. The history of the APPJ is described and most variations are discussed in Winter *et al.* [139]. In comparison with low-pressure systems the use of APPJs mitigates the need for vacuum equipment. This benefit is one that covers both the costly installation and operation, and also the restrictions placed on treatment area. A vacuum system can only treat an area enclosed within the chamber and as a result becomes significantly more expensive, in both time and money, as you increase the volume of the system [140]. Increasing the size of the treated area with an atmospheric system is easily achieved through both 1D and 2D arrays of devices [141–154]. Replacement of current vacuum systems for treatment of large areas has certainly been a successful application of APPJs, especially in treating rolls of materials [155, 156]. However, there has also been an interest in small-scale plasma

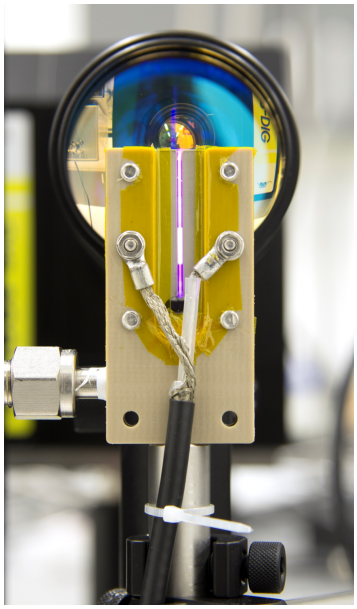

Figure 4.7: Picture of the APPJ used in this work

applications requiring focal treatment, notably in the field of biomedicine. Such utilisations include wound healing [157–159] and cancer treatment [160–163].

This particular jet has the channel formed between two stainless steel electrodes and two quartz plates, allowing for good optical access to the device whilst remaining compact. The length of the device's plasma channel is shown in figure 4.6 and is 30 mm. The gas enters the device through flexible pipework at a rate of litres per minute and is controlled by mass flow controllers. A plasma is formed by driving an RF voltage from a fixed frequency generator through a matching network and across the electrodes. Impedance matching is important for plasma generation, as the amplifiers that supply the RF voltage are designed to couple into a purely resistive 50 Ω load [164].

In this cross-field design the plasma recombines in the order of microseconds after exiting the device [165], leaving only neutral species in the effluent, unlike linear-field devices where charged particles that extend from the APPJ can form sheaths on incident surfaces and cause unwanted ion bombardment. The APPJ is also thermally cold enough to be used on temperature-sensitive materials, such as biological material or plastics; the neutral gas is generally below 100 ^{o}C and RF power can be limited to keep the temperature down [166].

When first igniting a plasma the electrons that are accelerated by the applied field must gain sufficient energy to ionise the background gas through collisions. With increased pressure comes decreased mean free path, such that the frequency of collisions quenches the

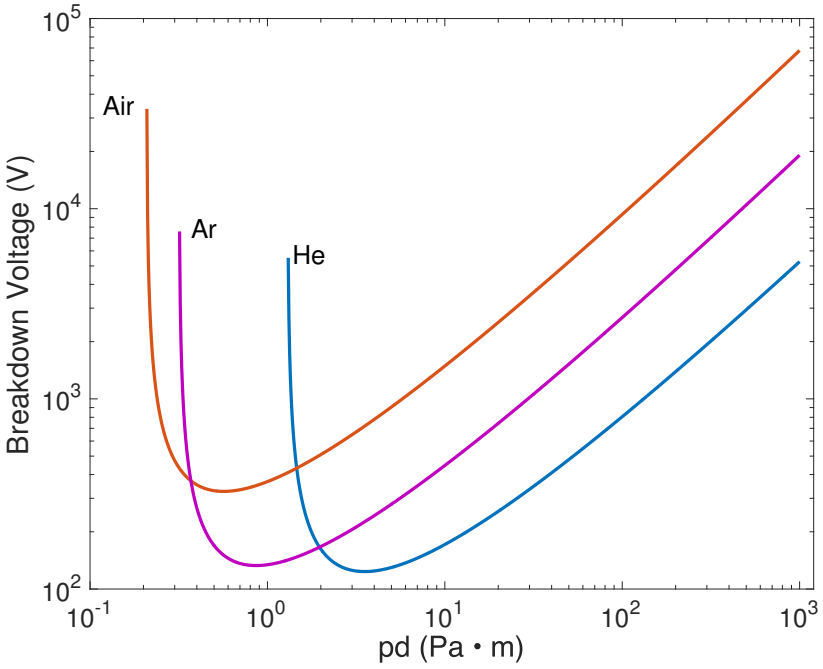

Figure 4.8: The breakdown voltage as a function of the product of the inter-electrode distance and gas pressure (pd) for various gasses. Values taken from [167, 168].

electrons before ionisation energy is reached. This then requires a higher voltage to be implemented between the electrodes to begin and sustain the discharge. This voltage can be reduced by decreasing the inter-electrode distance, such that secondary electrons (released from a surface after ion impact) become a major part of maintaining the plasma. This distance is also limited as quasi-neutrality must be maintained, with the plasma length scale remaining much larger than that of the Debye length. Consequently a relationship can be seen between the required breakdown voltage, the inter-electrode distance, and the gas pressure. This relationship, first discovered in 1889 by Friedrich Paschen, and hence called Paschen's law [169], is presented for various gasses in figure 4.8. For the APPJ the pressure is atmospheric at 750 Torr (10^5 Pa); and the inter-electrode distance is 10^{-3} m; for the GEC the pressure is around 75 mTorr (10^1 Pa); and the inter-electrode distance is roughly 10^{-1} (although difficult to know when running the ICP geometry as a CCP). In comparison, the two devices have very different power requirements, with the APPJ only needing a few Watts from the generator and the GEC requiring tens to hundreds.

Chapter 5

GEC cell model benchmarking

5.1 Ion energy distribution functions

Plasma sputtering through ion bombardment is a well-known process. Ions are generated and accelerated towards a material with sufficient energy to eject surface atoms through collisions, detailed in section 2.3. It is therefore important to know that the proposed method of deposition removal can create ions of sufficient energy to initiate this process. Table 5.1 shows the energies required for argon ions to eject various relevant metals and metal oxides. The Al and Al_2O_3 energies are included in the plasma chemistry used within HPEM shown in table 3.3.

Material	Sputtering threshold (eV)	Reference
Be	15	[170]
Al	29	[122]
Al_2O_3	50	[120, 121]
Mo	35	[122]
Rh	29	[122]

Table 5.1: Damage threshold for various materials in Ar

A first step is to benchmark IEDFs produced by HPEM against published experiments. Work done by Liu et al. shows experimental IEDFs taken within a parallel plate CCP and they are presented here in figure 5.1. It is important to note that the work done by Liu et al. had the IEDFs measured at the grounded electrode rather than on the powered electrode. As the system is parallel plate the ion dynamics will give reasonable qualitative comparison

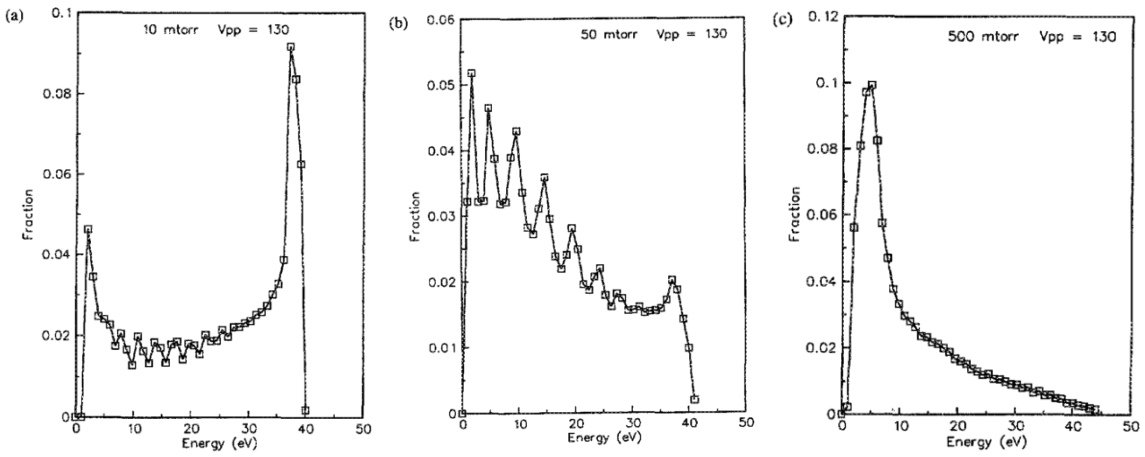

Figure 5.1: Measured IEDFs taken from Liu et al. (a) P = 10 mTorr, (b) P = 50 mTorr, and (c) P = 500 mTorr. In each graph the voltage supplied is 130 V and the frequency is 13.56 MHz. The IEDFs were measured on the grounded electrode and thus there is no applied bias [171].

due to the symmetric area of the plates and therefore symmetrical sheaths. This is not the case for the simulated data where the grounded area is much greater than the powered area and thus a self bias is formed (as described in section 2.3.1).

Figure 5.1 shows the resulting IEDFs and how their shape changes with pressure. The theoretical nature of these changes have been discussed in section 2.3.1.4 but these experimental results require further explanation. At 10 mTorr the bimodal structure is seen with a peak at very low energy corresponding to a low-frequency regime (ion transit time $\ll$ RF period). The lower energy peak is also much smaller than the higher energy peak as the plasma is only very weakly collisional, resulting in high numbers of ions passing through the sheath with no collisions from the higher ion density region. The bimodal structure is also very visible with the peaks being at the maximum and minimum sheath voltages. At 50 mTorr the plasma becomes more collisional, resulting in the majority of the ions undergoing charge exchange collisions within the sheath, creating slow moving ions that are not accelerated for the full sheath width. By 500 mTorr the plasma is highly collisional and nearly all of the ions undergo collisions within the sheath, leaving only a tail of high energy ions.

Figure 5.2 shows IEDFs produced using HPEM for the same input parameters as the IEDFs in figure 5.1. Qualitatively the simulations match the experiments by Liu et al. The differences all stem from the inclusion of a self bias within the model, which gives the electrode a negative potential thus increasing the potential difference across the sheath. At

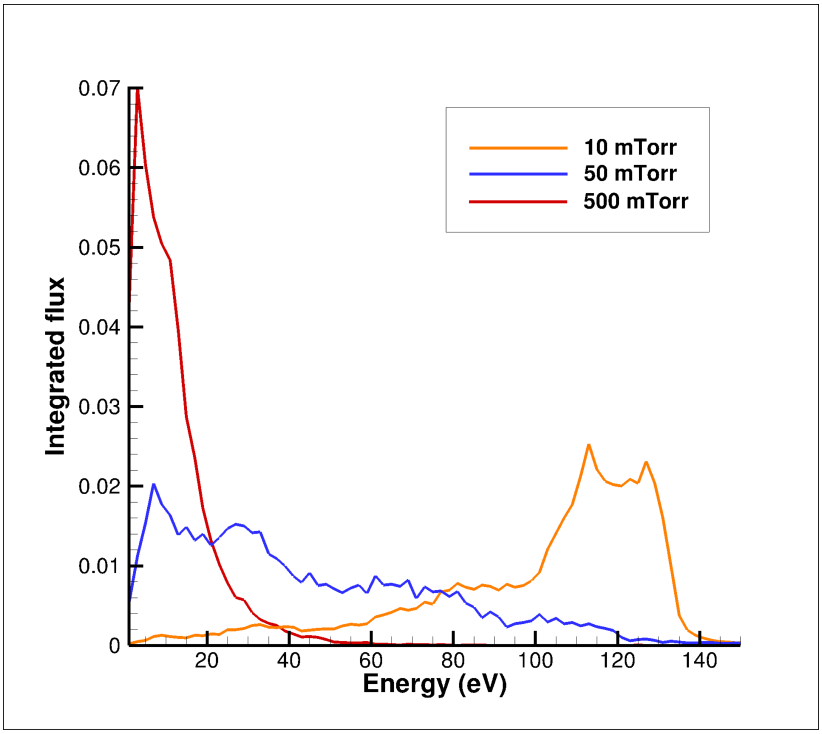

Figure 5.2: Simulated IEDFs for varied pressures. The graphs are all normalised so the area under the curves are equal.

10 mTorr the bias has pushed the IEDF structure up the energy axis with the lower peak being at the bias voltage. The higher energy peak is at the self bias plus the plasma potential. There are still some collisions within the plasma resulting in the tail towards lower energies and the increase in flux of the lower energy peak. At 50 mTorr the energies of incoming ions have not shifted up the axis, but spread. The sheath width has increased which gives further for the ions to accelerate producing higher energies, however the mean-free path of the ions remains the same and is no longer greater than the sheath width. This is also the cause of the loss of the high-energy peak, with almost no ions making it all the way through the sheath. At 500 mTorr the plasma is so collisional that the shift in energies is almost unnoticeable and qualitatively this IEDF compares extremely well with the experimental results from Liu et al.

These results show that the model can give accurate IEDFs for the given geometry. It also shows that a reduction in pressure will produce a substantial fraction of high-energy ions well above the requirements for sputtering the required materials. With pressures on published experimental work between 3.75 mTorr and 75 mTorr there should be sufficient energetic ions for the process [18, 19, 172, 173]. The exact working pressure that will be used

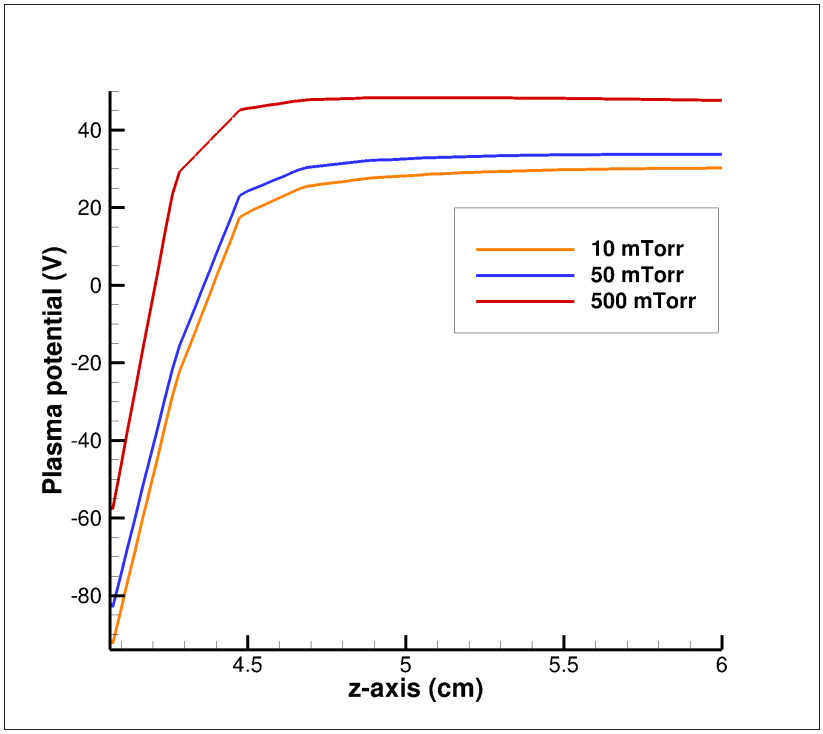

Figure 5.3: Plasma potentials for across the sheath at various pressures. The x-axis represents the z-axis of the simulated geometry where the location of the y-axis is the surface of the powered electrode. These are from the same simulation as the results in figure 5.2.

for this process in situ on ITER is not known [18]. A suggested working pressure of 13 mTorr has been suggested by Moser although this is not achievable experimentally in the York GEC device and will be investigated further later on in this thesis [20].

5.2 Sheath potential

To control the IEDF there are two values that are important; the plasma potential and the bias voltage. These two parameters define the potential difference across the sheath and hence the energy that an ion may be accelerated to in that distance. When looking at the sheath, for the parameters simulated in the previous section, this relationship can be seen in more detail. Figure 5.3 shows the potentials which were taken at the the same point as the IEDFs; 2.5 cm from the centre of the lower electrode. It is evident from the graph that as the pressure increases the values of the plasma potential shift positively along the y-axis. This is not entirely a correct description as the potential at the surface of the electrode, the effective self bias, increases slightly faster with pressure than the peak plasma potential. This results in a lower potential difference as the pressure increases (125.05 V at 10 mTorr, 119.47 V at

50 mTorr, and 108.43 V at 500 mTorr) but cannot explain the shape of the IEDFs shown in figure 5.2.

This bias change is due to better confinement at higher pressures, which reduces the flow of electrons to the wall and thus a lower bias develops on the driven electrode to maintain net current. The plasma potential rises with the pressure as increased collisions, due to the reduction in mean free path, result in a greater number of ionisation events. However the likelihood of collisions means that only a small percentage, if any, of the ions achieve the maximum energy possible as the pressure increases. This explains the spread in particle energies with pressure in the IEDFs in figure 5.2. This is not to say that the ions at higher pressure neutralise, as this depends on the electron density, as is known from the Saha equation [23]:

$$\frac{n_i}{n_n} \approx 2.4 \times 10^{21} \frac{T^{3/2}}{n_i} e^{-E_i/k_b T} \tag{5.1}$$

5.3 Experimental self bias

As a further comparison between the model and the experiments, the self bias obtained as a function of peak voltage was measured. This is an output of the model but experimentally the measurements were taken using a voltage probe for the peak voltage and the self bias formed was read off the power supply. Figure 5.4 shows the same trend for the bias and the model. The bias from the model is always higher, for the same peak voltage, than in the experiment but is always within 10 %. The explanation for this is that there is a difference in the ratio of grounded to driven areas in the two geometries, the data showing that the grounded area is lower for the experiment. The model has the walls of the reactor, the only ground in this set up, slightly closer than that of the experiment, as the efficiency of the code is proportional to the area being modelled. Reducing this area accelerates the solution time through a reduced number of calculations required, as discussed in section 3.1. With these simulations taking upwards of a week to complete this was a compromise that was made. This should, in theory, reduce the ratio of the ground and driven electrode areas and give a smaller bias in the model. However, within the experiment there are also areas of the wall that are either pipes to pumps or dielectric windows, which are not possible to include in a cylindrical 2D geometry, and reduce the overall grounded area below that of the model. The bias difference is not very large in comparison to the surface area difference,

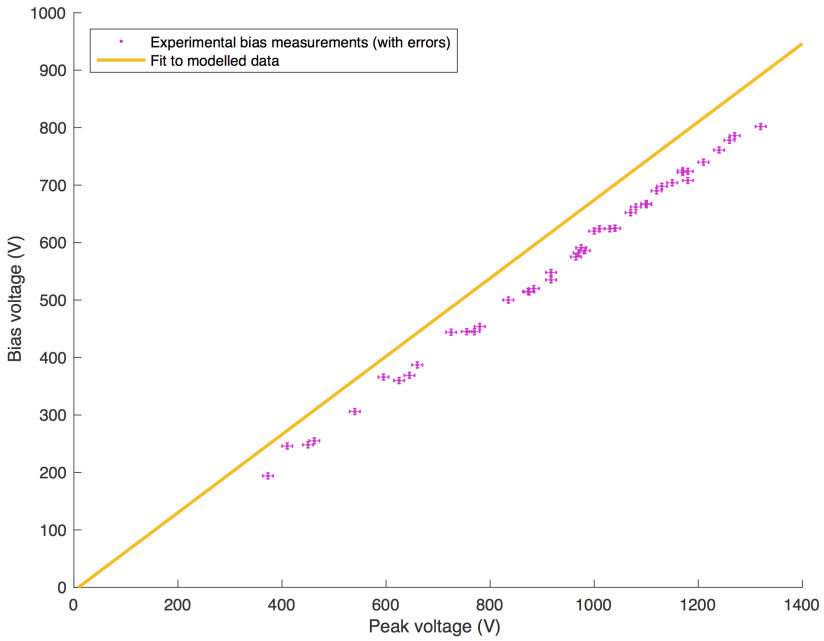

Figure 5.4: Experimental vs model self bias as a function of peak voltage. The error in the modelled data is not feasible to calculate and is not shown. All modelled data points sit on the fitted line. The experimental data was taken at multiple pressures from 20 mTorr to 60 mTorr. The model was run at 50 mTorr with simulated voltages of 50 V, 100 V, 200 V, 500 V, 1000 V, and 1400 V.

which suggests that the maximum self bias may have been reached within the model and that the experiment is close.

Research has been carried out into formulating the expected bias voltage given the ratio of driven to grounded electrode areas [174], this only applies for collisionless sheaths where the mean free path of the ions is greater than the thickness of the sheath, which does not apply in this case.

5.4 Etching

After investigating the dependence of the IEDFs on pressure and voltage the affects on etching were observed. Figure 5.5 shows the etching rates that have been achieved in York at (a) 24 mTorr and (b) 60 mTorr. These pressures were chosen as the minimum pressure possible in the chamber using the scroll pump, at minimal Ar flow rate, and within the capabilities of the matching unit. The higher pressure was chosen simply as a comparison that would be significantly more collisional, for which bias measurements had already been taken. The two graphs tell very different stories. Figure 5.5(a) has an exponential fit of only

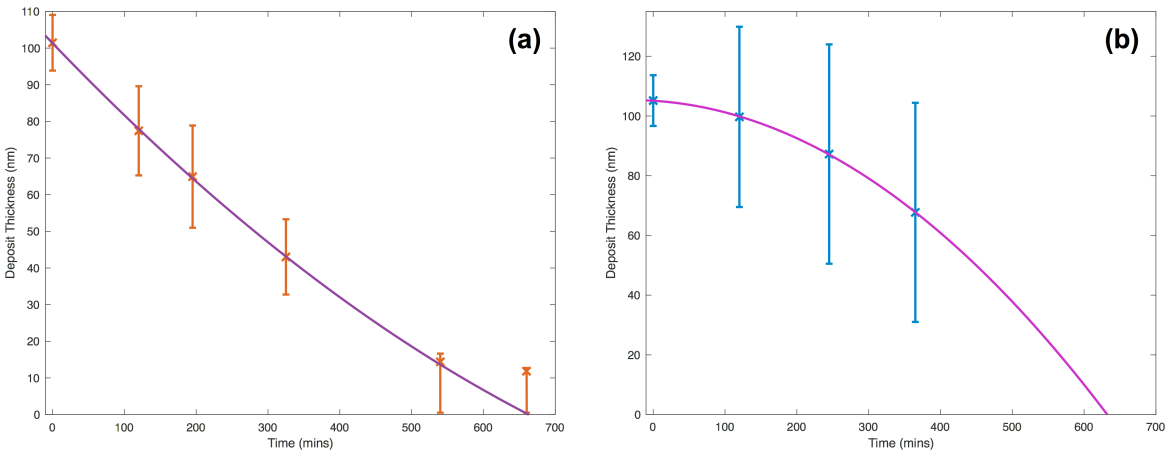

Figure 5.5: Experimental etching rates achieved in York at (a) 24 mTorr and (b) 60 mTorr. In both graphs the fit is quadratic.

the first 4 data points showing a decay in the thickness of the deposit with time spent in the device. The fit is only to these points as the interferometry to measure the thickness is not possible in the Filmetrics device for films below 10 nm. This reduces the measurement error on the final two points because the measurements are at the limit of the device, and half of the measurements taken for these final 2 points saturated the device, indicating full reflection. An error is shown on the figure implying that the actual thickness may be anywhere below 10 nm. In both 5.5(a) and (b) the points are the average thickness from multiple measurements from different locations over the entire surface of the mirror. The profile of the 60 mTorr result is shown in figure 5.6 with the difference in the maximum and minimum deposit thickness accounting for the large errors.

The self bias in 5.5(a) was measured as $\sim$ 420 V throughout, which corresponds to a $\sim$ 750 V amplitude, which is from 30 W generator input power. The rate of etching with these parameters averages out to be between 0.18 nm/min and 0.16 nm/min depending on the inclusion of the 5th data point. It is difficult to compare these results with previously published work on deposition removal, as the "cleaning conditions" are only given as an ion energy that is calculated from the addition of the plasma potential and the self bias [20]. The rates also depend on multiple factors including the quality of the Al_2O_3 film. When produced for previous experiments this has been closer to AlO; magnetron sputtering producing 47 % Al and 53 % O; and atomic layer deposition producing 50 % Al and 50 % O [18,20]. Having said this it is clear that the rate falls within these published results, which are between 0.02 and 0.4 nm/m [18]. Goshnick gives an etching rate of 0.15 nm/min for 400 eV Ar ions [119].

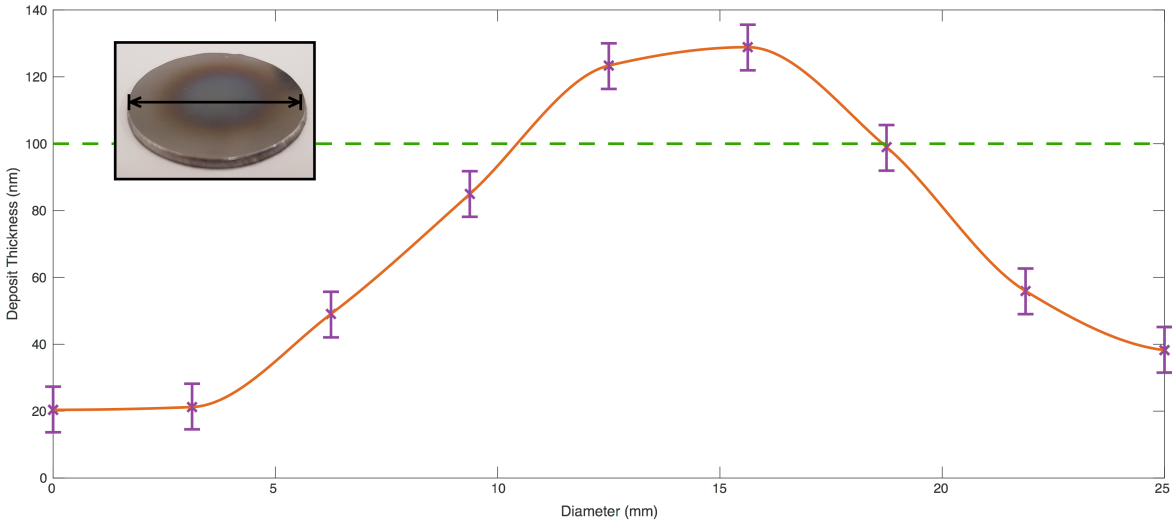

Figure 5.6: Thickness of Al_2O_3 across a mirror diameter after 365 minutes of exposure to 60 mTorr Ar with an electrode bias of 400 V from figure 5.5(b). The dashed green line shows the original 100 nm deposit thickness.

For figure 5.5(b) the input power was maintained, and the self bias reduced to $\sim$ 400 V, which corresponds to $\sim$ 680 V peak. The graph shows an exponential increase in the etching rate with time. The errors are also much larger which is a consequence of preferential sputtering towards the edge of the mirror, as detailed in the figure caption. These large errors make the fit unreliable. This preferential sputtering occurred with both pressures but for the 60 mTorr result there was not only significantly increased sputtering around the edge of the mirror, but also heavy redeposition towards the centre. As the deposition is removed the increased pressure holds a number of the atoms close to the surface allowing them to re-deposit. Some do escape into the bulk where they can be swept away by the gas flow, causing a decrease in the number of Al atoms in the system over time, hence reducing the re-deposition rate to a point where it equals, and then is taken over by, the sputtering rate. Visually this can be seen in figure 5.6, where the offset of the deposit can be attributed to the non-central placement of the mirror on the bottom electrode. Even after 365 minutes in the chamber the centre of the mirror shows 20 % more deposited material on it than it had initially. This will be discussed in more detail in section 5.5.

Non-uniform etching is expected due to the increased electric field at the sharp edge of the mirror. This is not something seen in industrial processing as the wafer is usually a dielectric placed on an electrode much larger than itself. This allows for these edge effects to be neglected, which is not true for a conductor. The increased field raises the ion flux to

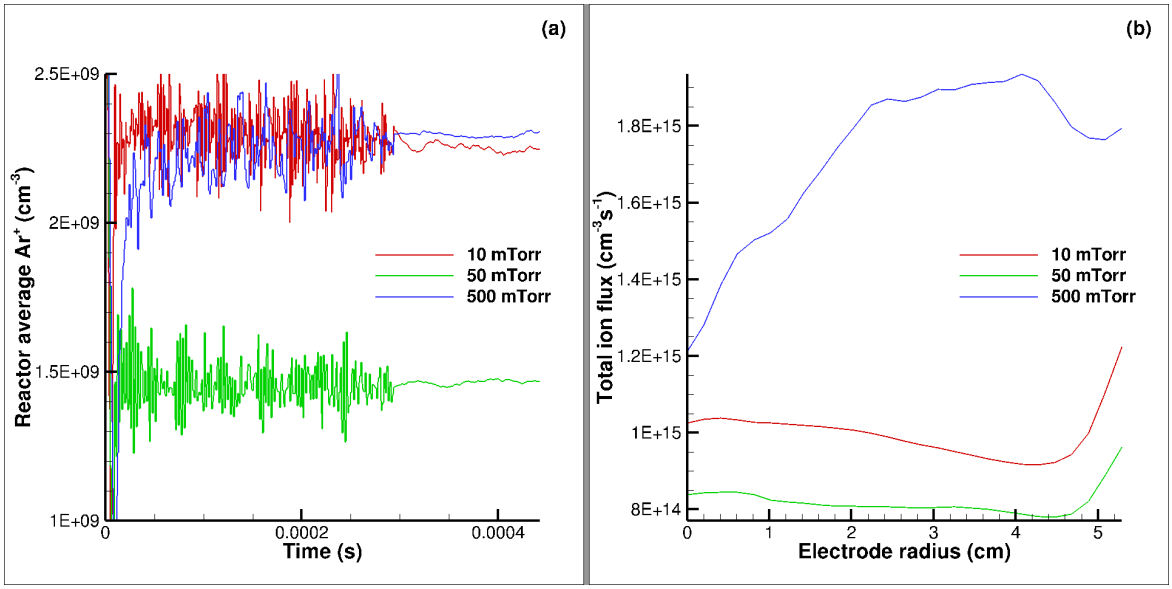

Figure 5.7: (a) Reactor averaged Ar^+ densities as a function of simulated time and (b) ion flux as a function of electrode radius in the GEC geometry. Both for various pressures at 130 V_{pp}.

the surface and so produces a greater etch. This can be seen in the simulations, figure 5.7, where the flux of the ions to the surface is high at the edge of the electrode. The angle at which the ions impact the surface also plays a part in the etch rate, with studies showing that etch rates peak at an incidence angle of $\sim 70°$ [175].

Figure 5.7 (a) shows the averaged density of Ar ions in the chamber. The noise for the first 66 % of the time is related to the acceleration of the simulation. In order to achieve a steady state more rapidly, a linear acceleration method is used whereby densities are increased or decreased within upper and lower limits. In this case acceleration is applied twice in every iteration of the FKPM; both at the beginning of the iteration; and then any transients introduced are allowed to damp out. The noise of the simulation during the accelerated period is high and does suggest that the acceleration bounds may be too aggressive, but the resulting densities once the acceleration is switched off are steady state. This figure shows that at 10 mTorr and at 500 mTorr the densities of ions within the plasma volume are almost identical and yet the fluxes to the surface, shown in figure 5.7 (b), are vastly different.

In figure 5.7 (b) there is a distinct difference between the flux for 500 mTorr and that of the lower pressures. This results from a mode change from α-mode to γ-mode within the plasma occurring at the sheath. There is a constant conduction current (flow of ions) through the sheath which collapses to zero during the RF cycle allowing electrons to balance the net

flux. As the ions impact the surface of the electrode they have a chance to release secondary electrons from the surface. These usually have a sufficient mean-free path to avoid causing significant ionisation events within the sheath. At the higher pressure the mean-free path reduces and the secondary electrons ionise atoms within the sheath and into the bulk plasma. In the 500 mTorr case this is driven by the increased field at the edge of the electrode. Such an increase propagates ionisation events towards the centre where the field is weaker and secondary electron emission from the surface is small. The production of ions in γ-mode at the electrode surface causes the densities of ions to be similar, on average, to those produced in the bulk at 10 mTorr and their proximity to the surface increases the flux.

For the 10 mTorr and 50 mTorr cases the sheath remains in an α-mode. The flux across the electrode has a near identical shape for the two pressures with a maximum at the edge owing to the increased field, and a peak in the centre due to maximum plasma density. The total number of ions at 50 mTorr is smaller than at 10 mTorr and so the flux to the surface is lower. From the IEDFs in figure 5.2 it is known that the 10 mTorr ions are of a much higher energy, on average, compared to the 50 mTorr ions. This will have a dramatic effect on the sputtering rate, with the 50 mTorr case having insufficient high-energy ions to etch whilst having substantial low-energy ions that may re-deposit.

5.5 Re-deposition

Once the Al and O has been removed from the surface it travels into the plasma and can ionise; the movement of these sputtered particles are what drive redeposition onto the surface, and are evidently the cause of the increased deposit thickness in figure 5.6. This is only discussed in a few pieces of literature in terms of experimental results [176–179]. These experiments discuss redeposition of two different types; *redeposition* has commonly been used to describe direct deposition from a sputtered surface into an adjacent surface, such as the wall of a trench; *backscattered redeposition* or *recondensation* then refers to those particles that deposit after returning from the gas phase. For this work, redeposition will be used freely to refer to both, however the lack of adjacent surfaces means that it can be assumed there will be no direct deposition. All four experimental methods in the referenced literature do not directly measure redeposition, but instead use simulation or derivation based on theory. They then come to varying conclusions about the rates for different materials and

pressures. In general it can be said that redeposition is not entirely well understood and that not being able to measure it directly, as it is convolved within the sputtering rate, is a problem.

For this work the redeposition was seen experimentally in figure 5.6 and has been included in the model based off Al and O neutral and low energy ions returning from the plasma. As seen in the surface chemistry, table 3.2.4, any neutral Al returning from the plasma has a 50 % chance of re-attaching to the surface. Any low-energy ion (below the sputtering threshold) also has a 50 % chance of re-attaching. These low-energy ions can be seen in figures 5.2 and 5.7, where the peak ion flux is of low energy ions at 50 mTorr.

Simulations were run using the surface chemistry matching the experimental parameters from figure 5.5 in section 5.4. The simulated etch profiles of the Al_2O_3 surfaces for both 20 mTorr and 60 mTorr are shown in figure 5.8. In these profiles the movement of the etched material can be seen re-depositing on different areas of the electrode. At both pressures the peak of the etching is at the edge of the electrode, which is expected as the flux and energies are at their peak in that region at these low pressures. The etching then differs between the two pressures, with 20 mTorr experiencing the slowest etching just inside from the edge of the electrode, and the 60 mTorr experiencing it in the centre of the electrode. When the simulation has been run without any redeposition, at both pressures, the result is similar to the 20 mTorr profile but significantly faster. It can therefore be concluded that the change in shape between 20 mTorr and 60 mTorr in this case is purely due to redeposition. The output etch rates from the simulation, averaged across the electrode, are found to be almost the same, which is is also seen in the experimental results in figure 5.5, although the errors in 5.5(b) are extremely large and the trend may not continue as the fit suggests. There is therefore a difference that is generally observed in the experimental etch profile and that which is output from the simulation, this suggests a fundamental problem with the surface kinetics in the simulation.

The rate itself for both is $\sim$ 25 nm/min which is two orders of magnitude higher than seen in experiment; this is a combined figure of both etching and redeposition reactions. Unlike experiment the redeposition rate is never greater than the etching rate at any point across the surface at either pressure. Both of these may be an issue with the input data and the current understanding of how Al_2O_3 is thought to etch and re-deposit. Other things to consider include the flows within the experiment and the model. In the experiment the gas

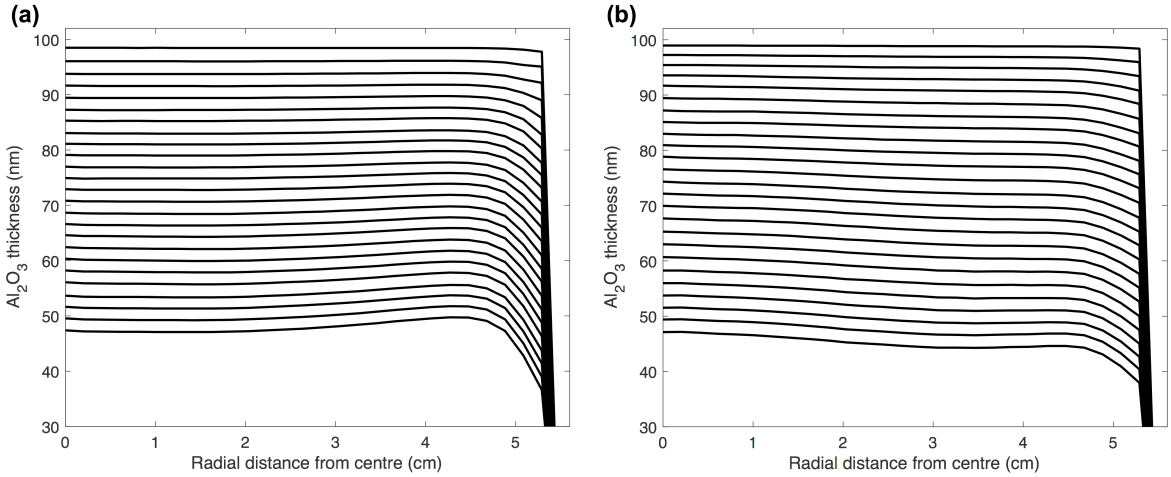

Figure 5.8: Simulated etch profiles of Al_2O_3 at (a) 20 mTorr and (b) 60 mTorr. In both cases the top line indicates the surface profile after one etching iteration and the bottom line is the final profile after 50 iterations. Not all iterations are shown for clarity.

flow comes from one source in the mid-plane of the reactor and exits via multiple points at various angles. In the model the mid-plane input remains but will still be dissimilar in a 2D system, as will the outlet being located around the base of the chamber, which will combine to cause a flow, even a slow-moving one, down the sides of the electrode. This will carry away some of the etched Al, leaving less to re-deposit. There is also the consideration that the model is technically etching AlO with the properties of Al_2O_3, which is not ideal.

Comparisons, aside from simple qualitative descriptions of the etch profiles and trends, cannot be made between the experiment and the surface model to any real degree of accuracy. It is clear the development of the surface chemistry is required. However, it is possible to compare the two simulations with regard to the plasma as the only variable between the two is the pressure, and the plasma modules have been well benchmarked against experiments, as previously cited. Looking into the outputs of the plasma the amount of Al being removed from the surface and staying within the plasma is five orders of magnitude lower than the background Ar in number density (10^9 and 10^{14} cm^{-3} respectively). This has negligible effect on any of the plasma properties and this is at a flux into the plasma 20 times higher than would be seen experimentally. Any change in plasma properties is purely down to pressure differences. This is easy to differentiate from the effects of the Al as the surface module and, therefore, the flux of Al into the plasma does not initiate until 2/3 of the way through the simulation. This is an important result as although inclusion of Al in the plasma chemistry has almost no effect on the plasma properties, its inclusion is important

when considering redeposition.

5.6 Summary and conclusions

- The code has been successfully benchmarked against experiment in terms of the IEDFs and the bias voltage.
- Ion energy distributions are an important control when it comes to deposition removal which have been modelled and compare well to experimental IEDFs in the same geometry, voltage, and pressure. The inclusion of the self bias increases the energy of the ions and pushes the IEDF along the energy axis which is in turn useful for controlling the IEDF.
- The simulated bias is slightly higher than in the experiment, which is due to the GEC geometry in the model having much closer walls, reducing the ratio of ground to driven area. This is only a slight difference in bias suggesting that the model may be at the maximum self bias required to balance the current, and that the experiment is close to the required ratio.
- Experimental etching of the Al_2O_3 has been successfully giving an etch rate of 0.18 nm/m at 24 mTorr with a 420 V bias. This has compared well with previously published experimental data in similar parameters. The 60 mTorr result showed significant redeposition in the centre of the mirror. Analysis of the IEDFs gives some insight into the cause.
- The IEDFs are non uniform across the electrode surface, with considerable changes in energy with pressure and radial distance. At all pressures there are changes in the flux of ions across the electrode with peaks at the edges due to edge effects. The centre also sees a rise of flux in lower pressures owing to the plasma density being greater in the centre of the volume.
- Etching of Al_2O_3 isn't very well understood, with suggestions that preferential etching of O leaves an Al surface which accounts for the higher-than-expected etching rates. The inclusion of redeposition is important in etching rate calculations, as the flux of ions may be similar at different pressures but their energies are not. Al ions below the

etching threshold energy are likely to re-deposit, this is also true of any Al neutrals that come into contact with the surface.

- The surface kinetics module is a simple model that cannot quantitatively describe the etching process for Al_2O_3 but has given some interesting qualitative results, showing that the profile of the etch depends heavily on re-deposited material.
- Even without the SKM it is possible to predict the quality of the etch based on the flux and energy of incoming ions.

Qualitatively, etching is a well-understood process which has been modelled successfully in terms of how the system pressure alters the IEDFs and how they impact the etching process. It is clear from this analysis that lower pressures, where the system becomes weakly collisional, provide a better environment for etching. This is especially true after identifying redeposition as an important factor to take into consideration, even in a plasma model, where the etched material has limited to no impact on the plasma itself. No quantitative results can be taken from the SKM owing to the current limitations of the model in terms of surface chemistry, the complexity of Al_2O_3, and how it etches. It may be more reasonable to attempt this same process with BeO as it is a much simpler molecule but with a lack of comparative experimental data it is not useful for benchmarking of a model. Detailed optimisation of the process is therefore unachievable; only general guidelines as to the pressure of the system and understanding of how the IEDF can be utilised to predict the etching process.

Chapter 6

Modelling towards ITER

This chapter will look at comparisons between simulations carried out here at York, along with experiments completed by Moser et al. at Basel. The experiments are detailed in multiple papers and within the thesis of Lucas Moser, which will be cited at the relevant points. The experiments were funded by the ITER organisation, have not been conducted in any collaboration with York, and were mainly completed prior to the work carried out at York. There is also a modelling investigation into geometry, voltage, and frequency changes in a simplified geometry to discover trends and guidelines for installation of this method on ITER. Results from the introduction of a static magnetic field into the system are also shown, as these will be present.

6.1 Basel B-field chamber

The B-field chamber is a vacuum vessel designed to be inserted within a re-purposed superconducting magnet at the Swiss Plasma Center, Ecole Polytechnique Federale de Lausanne. Various experiments were carried out within the chamber, some of which will be used as a comparison to modelling. The majority of the experiments were undertaken in the absence of the field. The chamber is shown in figure 6.1 and is analogous to the geometry given in figure 3.3. Three mirrors were housed within a Cu electrode for initial experiments, but this was then changed to a full, mirror-polished, Cu electrode with a 200 nm Mo coating. This is affixed to a rotatable joint, allowing for multiple magnetic field angles of incidence to be investigated. The depth of the chamber within the device can be changed in order to adjust the strength and polarity of the field. The field itself is achieved as a solenoid with the coil

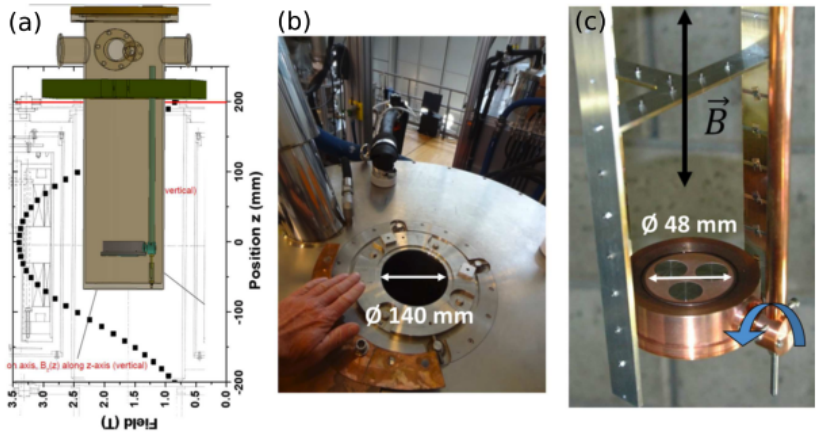

Figure 6.1: (a) The B-field chamber inserted into the superconducting magnet. (b) The hole in the magnet where the chamber is inserted. (c) The copper electrode with three mirrors mounted. This figure was taken direct from the thesis of Lucas Moser [20].

around the chamber.

6.1.1 Comparison with GEC modelling results

As a comparison with the modelling results obtained for the GEC, the IEDFs for 10 mTorr and 50 mTorr in the B-field chamber are shown in figure 6.2. They compare very well with the results from the GEC, however there is the apparent loss of the bimodal structure and a slightly lower energy for the 10 mTorr result. This result is interesting as the expectation is that a higher-grounded area would increase the self bias and thus push the IEDF up the energy axis. However, as the geometry is very different the density of ions in the plasma is increased with fewer of them being incident on an opposing electrode and neutralising. As a result of this the number of ions available to balance the current is greater, so the bias does not need to be as high as in the GEC geometry. The bimodal structure is lost as the self bias is $\sim$ 20 V and the smaller peak is lost within the noise of the simulation.

The dashed lines in figure 6.2 are from the same simulation parameters but with a geometry 1/3 the height. As the chamber is designed such that the electrode can be moved up and down within the device, the grounded to powered ratio will also change. As the electrode is now closer to the upper wall the number of ions that get neutralised on a wall increases and the ion density drops. This shifts the ion energies for both the 10 mTorr and 50 mTorr in the 1/3 height geometry up the energy axis, as the self bias increases to attract a similar number of ions as before. This is an important result for implementation of this method onto ITER as the ratio of electrodes in complex geometries is not as simple

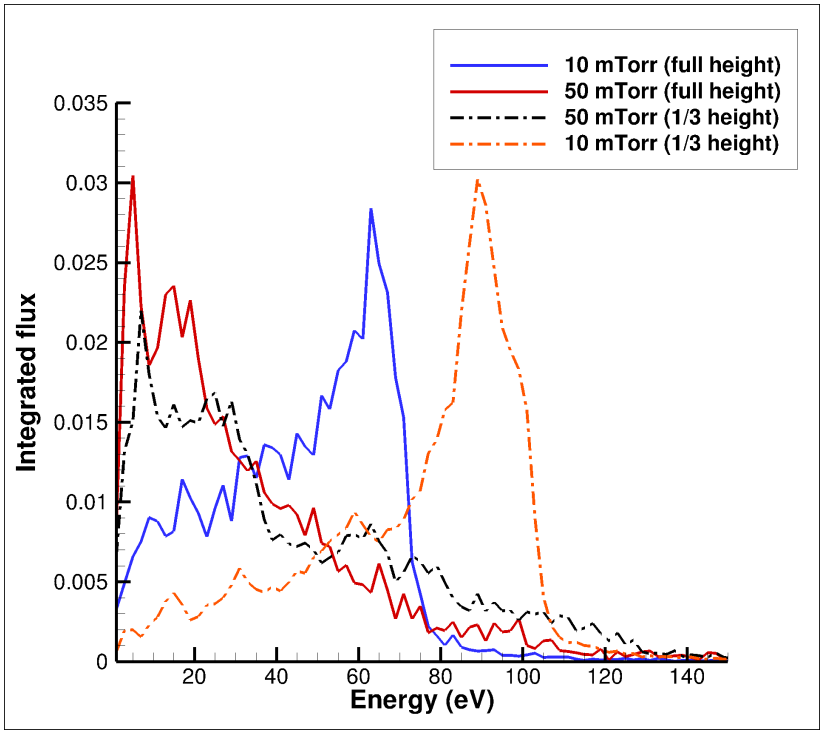

Figure 6.2: IEDFs for the Basel geometry at 10 mTorr and 50 mTorr for the same parameters as were run in the GEC simulation (130 V). A second geometry was run at 1/3 the height of the chamber and the results shown with the dashed lines.

as calculating the areas, without real knowledge of the extent of the plasma.

6.2 Simplified geometry

Looking towards ITER and the many geometries of mirrors to be used on the device it would be extremely time consuming to study each one individually. It has been seen that an important output of the simulations is the IEDF. In order to find the general trends that may be followed to reach the desired function the simulations need to be simplified and parameter scans completed. The first simplification is the geometry, shown in figures 3.4 and 6.3, which is very similar to the GEC geometry in outer shape, but the electrode has been reduced in height and simplified, and the ICP structure has been removed. Multiple versions of this geometry mesh, for input into the simulation, with different heights and widths have been created to investigate the effects of the grounded area; this will be discussed in section 6.2.1. The electrode radius changes slightly between simulations due to the edge needing to be on a cell boundary but stays within 6 mm of the 5 cm goal radius. In this geometry there is also a spatially separated "wafer", which is a requirement of the code to get ion

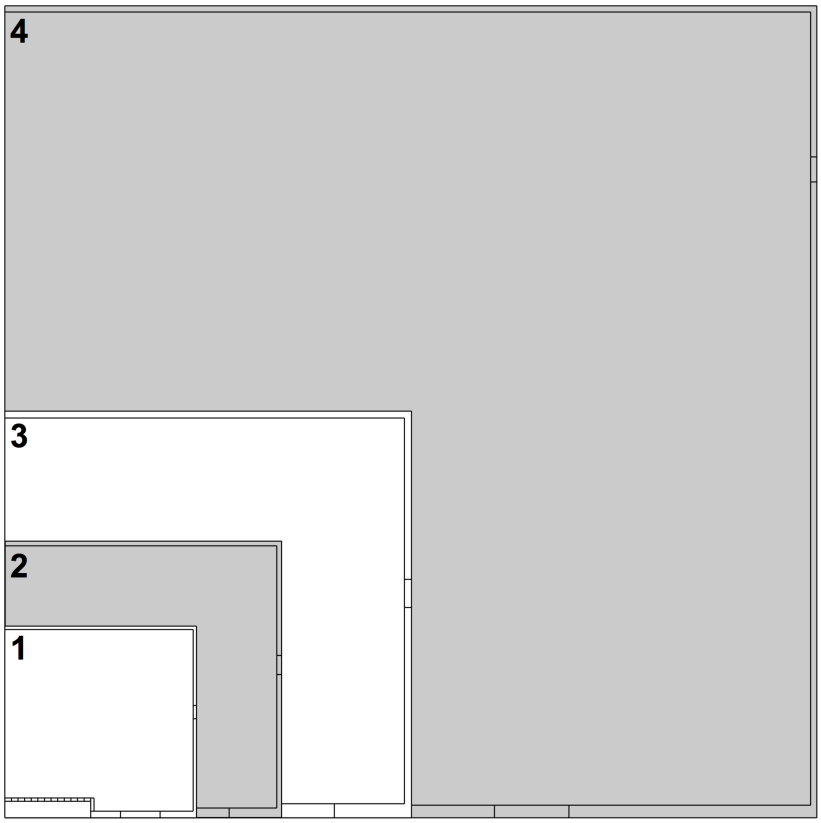

Figure 6.3: Visual representation of the simple geometries 1 to 4. A labelled version of this geometry is shown in figure 3.4 with the heights and radius of the geometries given in table 6.1. The electrode remains the same size in all geometries.

energy distribution functions for different locations across the electrode. The cell size of the geometries can be seen in figure 6.3 where the cells are all square and the upper and side walls are one cell thick. The number of cells increases for each geometry, and the size of the cells changes slightly to accommodate the electrode radius remaining the same.

Geometry	**Height and radius (cm)**
1	11.8
2	17.7
3	23.6
4	47.2

Table 6.1: Values for height and radius of the simple geometry.

The ideal IEDF is homogeneous across the entire mirror, has a sufficient number of ions above the sputtering threshold of the BeO surface to ensure efficient etching, and has as few low energy ions possible in order to limit redeposition. Up to this point the work was done using multiple pressures, in comparison to experiment or previous simulations. The results

have shown that the 10 mTorr results are favourable when working towards etching due to the greater definition of the IEDF. It has also been suggested, based on experimental results by Moser, that 12 mTorr is a good working pressure for implementation on ITER [20]. For these reasons, and the fact that some simulation work has already been done at this pressure, the rest of this work will focus on 10 mTorr.

As briefly mentioned in section 3.2.3 there is no data for sputtering of BeO by Ar. The data available for BeO is mainly theoretical and is focussed on light ions, where the Bodhansky formula for sputtering yield may be used (it is only valid when the incoming ion is <0.4 the mass of the surface atom) [180]. Comparisons from Moser give BeO having about half the sputtering yield as Al_2O_3 in Ar at a 200 V bias [18], however the quoted values are based on fits from Yamamura, which has limited data at the lower energy levels [122]. It is also contrary to experimental results from the lower mass ion etching with D_2, which shows BeO having a lower threshold energy for sputtering than Al_2O_3 by more than 50 % (29 eV to 66 eV respectively) [59]. Experiments have shown that BeO does etch faster with Ar than with lighter elements, such as He and H_2, but there is no direct experimental comparison of sputtering thresholds [181]. With the limited information available the work here will assume a sputtering threshold in the region of 25 eV, which is half that of Al_2O_3 [120, 121].

6.2.1 Grounded area

Each mirror within ITER will be positioned in such a way that the grounded area available will be substantially different. The simple geometry was so used to increase the volume of the plasma whilst maintaining the electrode area. This allowed for the identification of any trends the change in reactor volume and distance of the electrode from the walls had on the plasma. The values for a (height and width of chamber) in each geometry are given in table 6.1. Figure 6.4 shows the evolution of the ion energy and flux on the powered electrode as the volume of the chamber increases.

The general trends of increasing the volume of the reactor are a decrease in maximum energy and a decrease in peak flux. The change in flux can be seen specifically in figure 6.5 where the change in the total flux across the surface doesn't seem as disjointed as it does in figure 6.4. All of the geometries show a peak at the edge of the electrode from the effects of the increased field in that area, which then reduces to a minimum within a cm of the edge. For geometry 4 the minimum flux is actually at the centre of the electrode,

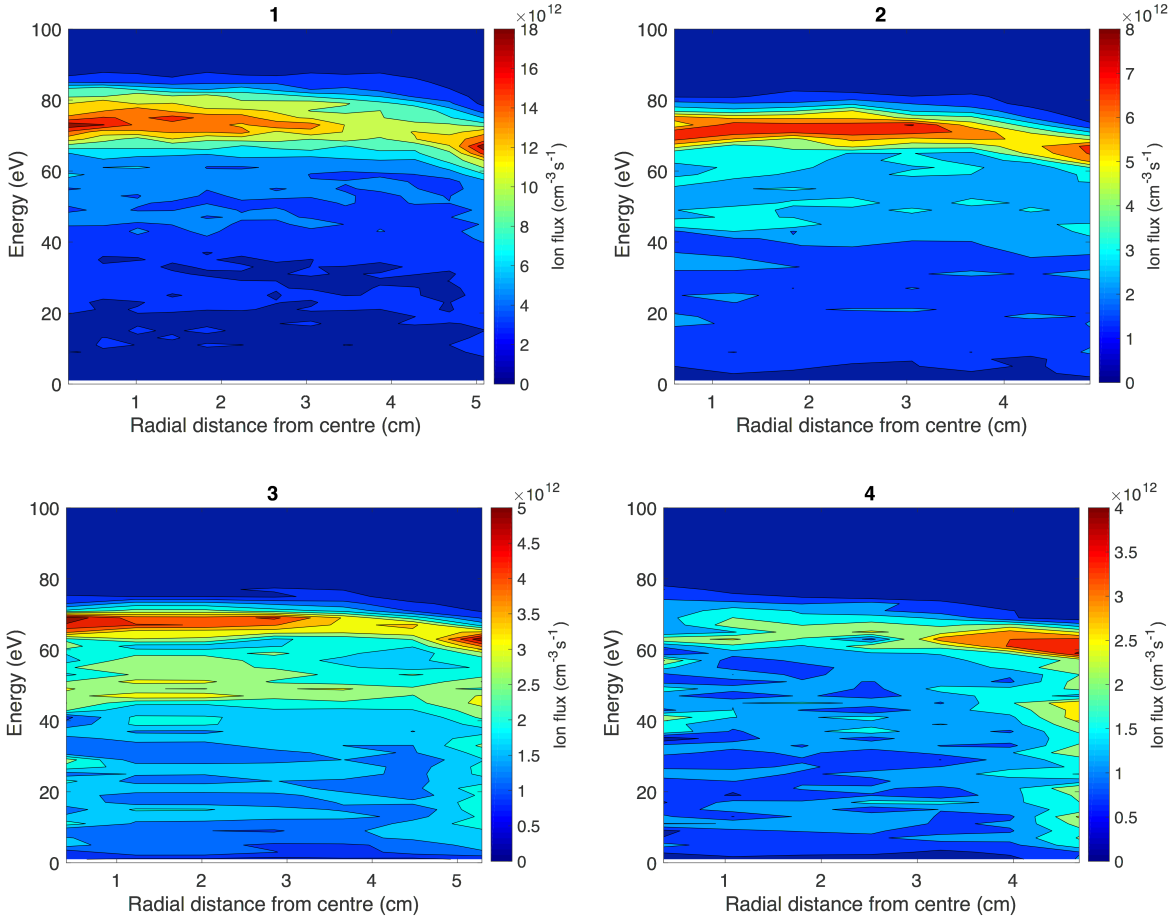

Figure 6.4: Simple geometries, as defined in table 6.1 and shown in figure 6.3, ion energies and flux as a function of radius. The pressure in all geometries was maintained at 10 mTorr and the applied voltage was 130 V. The bias voltages created were -58.8 V in geometry 1, -56.0 V in geometry 2, -51.8 V in geometry 3, and -71.1 V in geometry 4.

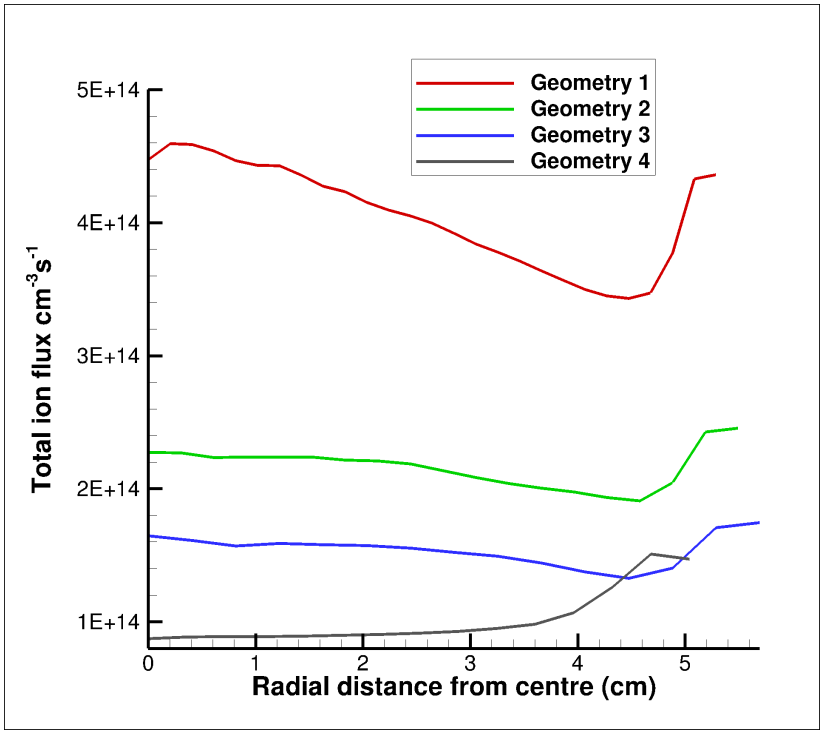

Figure 6.5: Flux to the powered electrode as a function of chamber volume for the simple geometries. Between the simulated geometries the size of the electrode changes slightly due to the mesh cells which accounts for the differing radii.

Geometry	Plasma potential and self bias (V)
1	24.7, -58.8
2	23.0, -56.0
3	20.6, -51.8
4	8.8, -71.1

Table 6.2: Values for measured plasma potential and self bias in the simple geometries.

which is completely contrary to that desired for etching purposes, especially considering the number of low-energy ions that make up that flux. The number of these low-energy ions is also clearly increasing with reactor volume, where in geometry 1 and 2 there is a clear single peak of ion energies across the electrode but spread over a wide range. Geometry 3 begins to have more of a bimodal structure with a smaller peak forming at about 50 eV, which corresponds to the minimum sheath potential with some collisions, as discussed in section 2.3.1.4. By geometry 4 the ion energies have lost a significant amount of structure across the electrode and it is not a stable or homogeneous system.

In table 6.2 the plasma potential and the self bias can be seen to be decreasing very slightly for the first three geometries, which appears contrary to the theory that as the

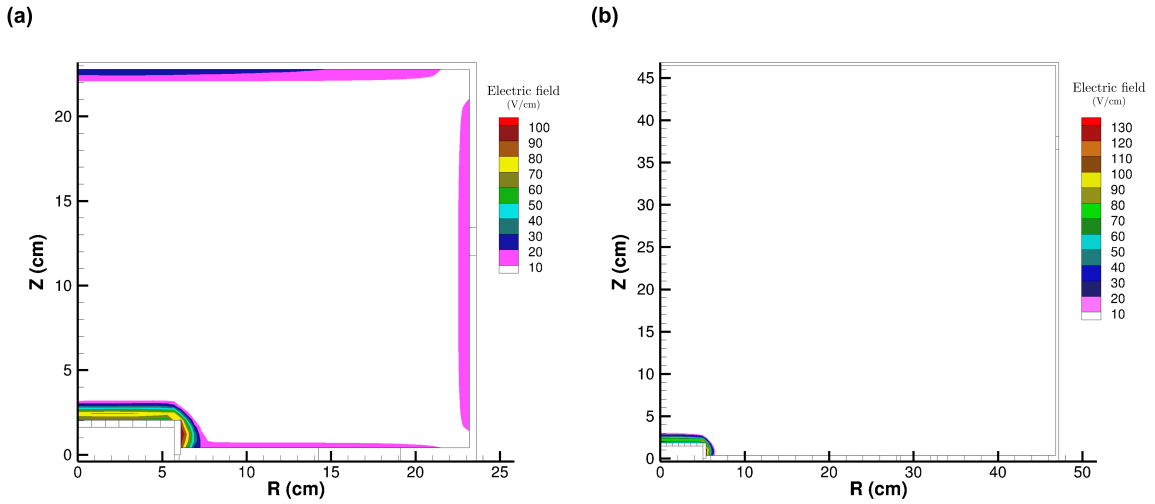

Figure 6.6: The electric fields averaged over an RF cycle for (a) geometry 3 and (b) geometry 4.

grounded area increases in relation to the powered area the bias should increase to balance the current. What the result shows is that in this simple geometry the bias for this particular input voltage is already at the maximum required to balance the current; no further increase in the ratio of grounded to powered electrode area will change the bias voltage. However, what is also shown is what occurs when the grounded area goes to the extreme.

The plasma in each of these first three geometries forms sheaths on the upper and side walls. However, by geometry 4 the walls are such a distance away that the plasma does not exist at these extremities. A disconnection of the plasma to the geometry size has occurred and the only ground nearby is from the lower wall. This has caused the electric field to be purely confined to the region immediately around the electrode, shown in figure 6.6, which has given rise to the dramatic edge effects seen in figure 6.4. In all of the cases the ion energies are taken from the upper surface of the electrode, but it is possible that in geometry 4 that the current flow to the ground is now no longer from that upper surface but from the side, which is actually taking the vast majority of the flow. Clearly at some point it doesn't matter how big the ground is if it is too far away to be in contact with the plasma. Whether this is an issue for any of the mirrors within ITER is unknown and will depend on the specific layout of each individual optical system.

6.2.2 Voltage variation

The self bias is also dependent on the input voltage of the system, as shown in figure 5.4 in the previous chapter. Figure 6.7 shows how the ion energies and flux change with the given voltage and show the evolution of the plasma potential and the bias voltage with this change. The voltages used were 50 V, 200 V, 300 V, 500 V, and 1000 V, and were all run within geometry 1 at 10 mTorr. In each case the link between the bias voltage, the plasma potential, and the ion energy distribution can be seen. The maximum energy ions are at the sum of the bias voltage and the plasma potential, the bottom of the main band of ions is at the bias voltage. Ions with energies below this were created within the sheath. These low energy ions would be attracted to the surface but a number of them are below the $\sim$ 25 eV sputtering threshold of BeO.

In figure 6.8 the overall flux of the ions at the different voltages is shown. From figure 6.8(a) the increase in the edge effects with the voltage can be observed more clearly, especially in the case of 1000 V, where the spread of energies masks this increase in the contour plots of figure 6.7. Increasing the voltage would give a faster etch due to the higher energies and flux but the non-uniformity of the etch would also substantially increase. This is detrimental for the underlying mirror as erosion of the mirror, if non-uniform, will cause the surface to become misshapen and mirror shape is significantly linked to its function. Figure 6.8 (b) shows that the average increase in flux is not linear with the voltage. Although not shown here, the difference between the maximum and minimum flux for each voltage follows the exact same trend, showing that the non-uniformity change is also non-linear. From the voltage variation there is a clear trade off between energy and etch uniformity. Higher voltages mean higher energy and flux which increases the etch rate and also reduces redeposition. This is only useful if the uniformity of the etch is unimportant, however, with etching thresholds for the mirrors themselves being only 35 eV (for Mo) any ions above this energy would begin to etch the mirror once the deposit has been removed. With a non-uniform etch the mirror itself would become non-uniform and could, as a result, no longer be fit for purpose. From this the only recommendation would be to keep voltages low, 50 V keeps all ions below 35 eV and hence is the voltage of choice for this specific geometry.

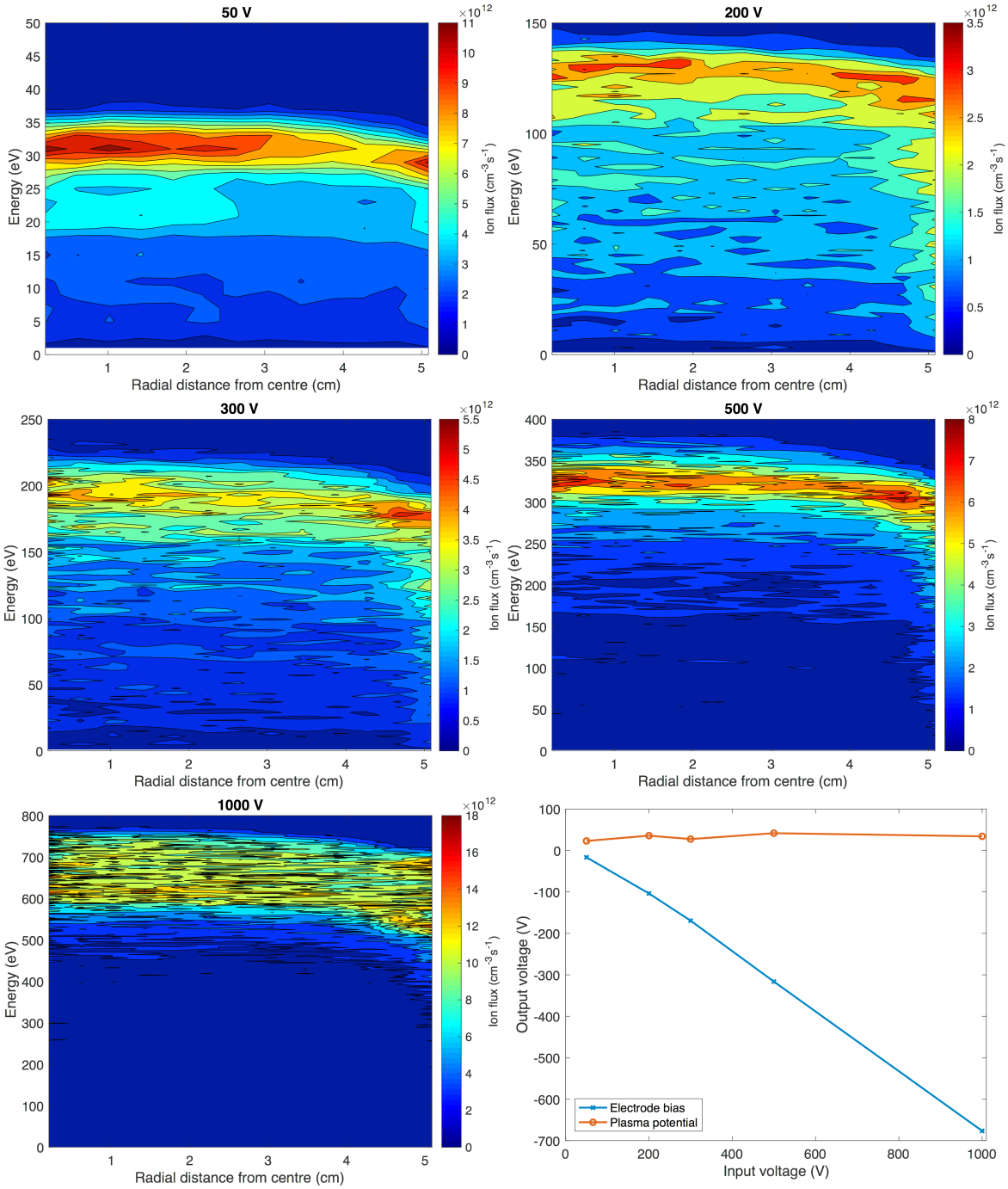

Figure 6.7: Ion energies and flux as a function of radius for varying voltages at 10 mTorr in geometry 1 with the plasma potential and electrode bias as a function of input voltage also shown.

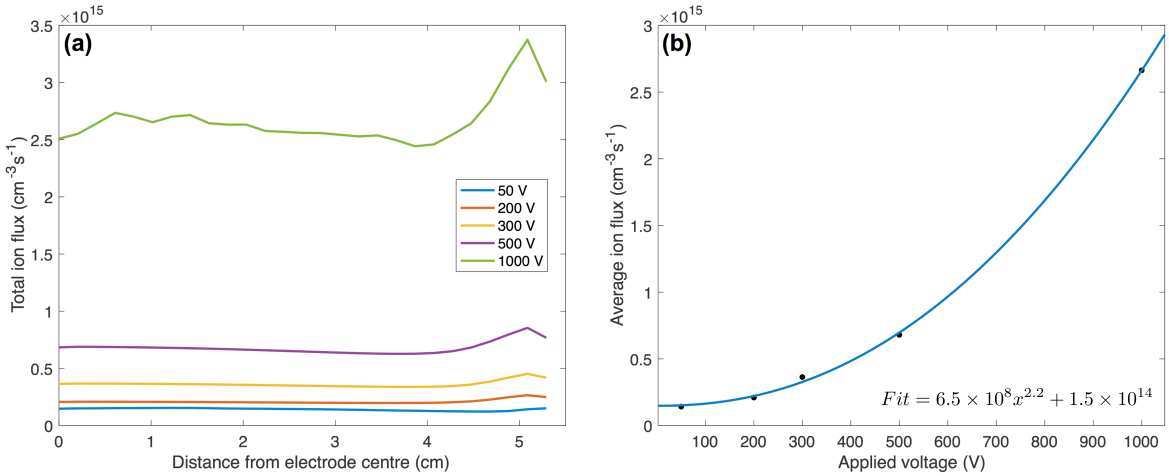

Figure 6.8: Ion flux variations on the powered electrode as a function of input voltage. (a) shows the spatial distribution of the flux along the electrode and (b) gives the average flux as a function of input voltage.

6.2.3 Alternative frequency

It is known that increasing the driving voltage frequency of a discharge increases the plasma density and ion current, while maintaining the maximum ion energy (assuming the geometry, pressure, and voltage remain the same) [182]. The simulation was, therefore, run at various harmonics of 13.56 MHz in geometry 1 at 130 V; the ion energy and flux as a function of electrode radius are shown in figure 6.9. The results are as expected, with the higher frequencies increasing the flux, which can be seen more easily in figure 6.10. The ion energies themselves decrease very slightly and are spread over a much smaller range due to the decrease in the sheath width. This is good for etching as having a finer band of energetic ions would lead to better tuning of the system. The number of low energy ions also decreases as the frequency rises as the sheath gets narrower leaving less path length for collisions, this would decrease re-deposition.

The flux changes in figure 6.10 (a) also show that the increase with frequency is greater in the centre of the electrode than it is towards the edge. This is attributable to the overall increase of the plasma density, shown in figure 6.11 (a), which can be seen as a multiplication that increases the areas of high density more than it increases in areas where it is low. The greater number of ions in these locations gives rise to a higher flux. This will give a less uniform etch with higher frequencies, which is not ideal when the threshold energies for the deposit and the mirror itself are so close (25 eV presumed for BeO and 35 eV given for Mo). The range of energies at 60 MHz is between $\sim$ 50 eV and 65 eV with the main flux across

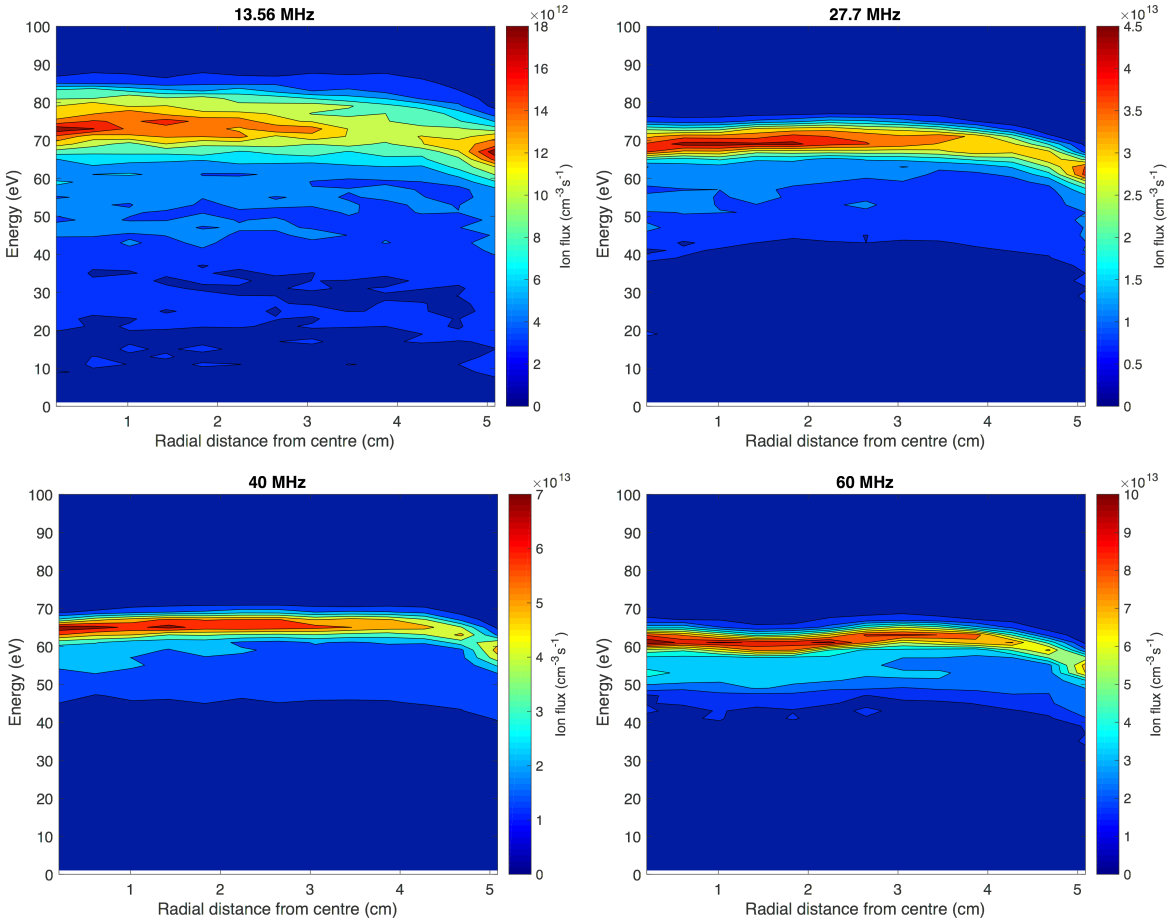

Figure 6.9: Geometry 1 ion flux and energy as a function of electrode radius for various frequencies. The pressure was set at 10 mTorr and the voltage at 130 V.

most of the electrode being between ∼ 58 eV and 65 eV. Reducing the voltage could bring the maximum energy below the 35 eV threshold energy of Mo etching while maintaining the vast majority of the flux above the assumed 25 eV BeO etching threshold. This removes the necessity to have a uniform etch, assuming there is no etching below the threshold energy for Mo, as there will never be any damage to the mirror itself. This is potentially not a valid assumption to make as is has been shown that metals, such as Mo, have much higher sputtering yields compared to metal oxides when compared at higher energies, with the yield increasing by an order of magnitude after initial sputter cleaning of any oxide layers [183]. This could mean that the yield of Mo below the threshold, where some sputtering may still take place, could be as fast that the BeO surface that has been removed.

The flux increase with frequency is different from that seen with voltage, as shown in figures 6.8 (b) and 6.10 (b). The increase is very slightly sub-linear with frequency and is

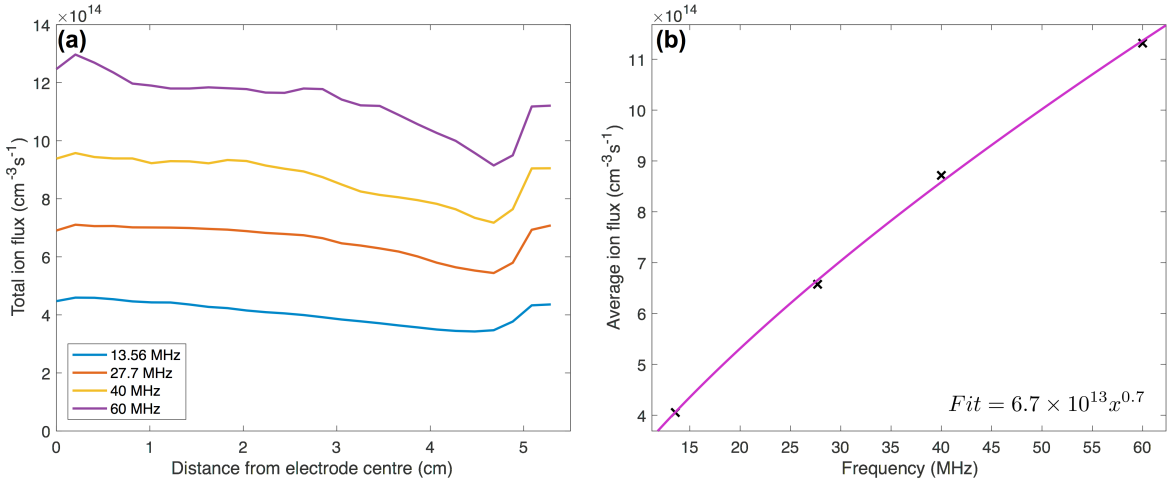

Figure 6.10: Total ion flux vs electrode radius with varying frequencies (a) and average ion flux as a function of frequency (b).

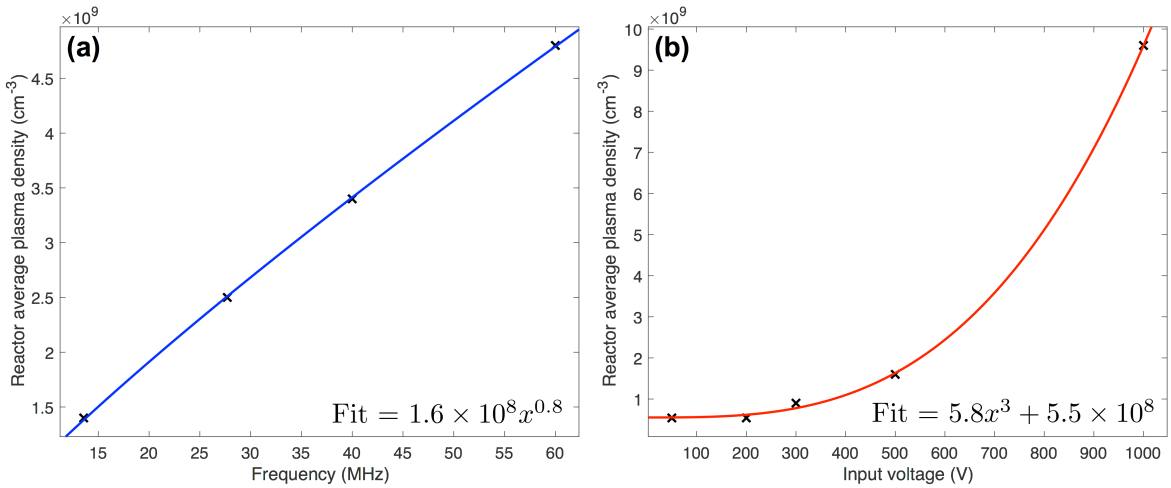

Figure 6.11: Plasma density as a function of (a) frequency with a fixed voltage of 130 V and (b) voltage with a fixed frequency of 13.56 MHz.

super-linear with voltage, which is expected. Figure 6.11 shows that as both voltage and frequency increase, the plasma density increases and, that being so, there are more ions in the plasma in general. With the increase in frequency the bias voltage decreases only by a few volts but with an increase in voltage the bias increases significantly.

6.2.4 Optimisation

The geometry variation indicated that the geometrical changes were significant. This is already set within ITER and, thus, optimisation is not something that is reasonably achieved through geometrical changes. Some conclusions regarding geometry will be discussed in the summary of this chapter. From the voltage and frequency variation some optimisation can be made. The number of low-energy ions striking the surface is linked to the sheath width. However, it appears that the number of these ions being produced within the sheath is relatively independent of the voltage but not of the frequency. To reduce the redeposition the number of ions below the threshold etching energy should be kept as low as possible, so increasing the frequency appears to be an obvious choice. As discussed in section 6.2.3 the frequency increase can even keep the majority of the range of energies between the threshold energies of the BeO deposit and the Mo mirror, negating the need for a uniform etch rate across the mirror. However, the low energy ions would cause redeposition to some extent, which will decrease the already experimentally-slow overall etching rate ($<$ 0.2 nm/m at 130 V and 13.56 MHz for the Al_2O_3 proxy in chapter 5).

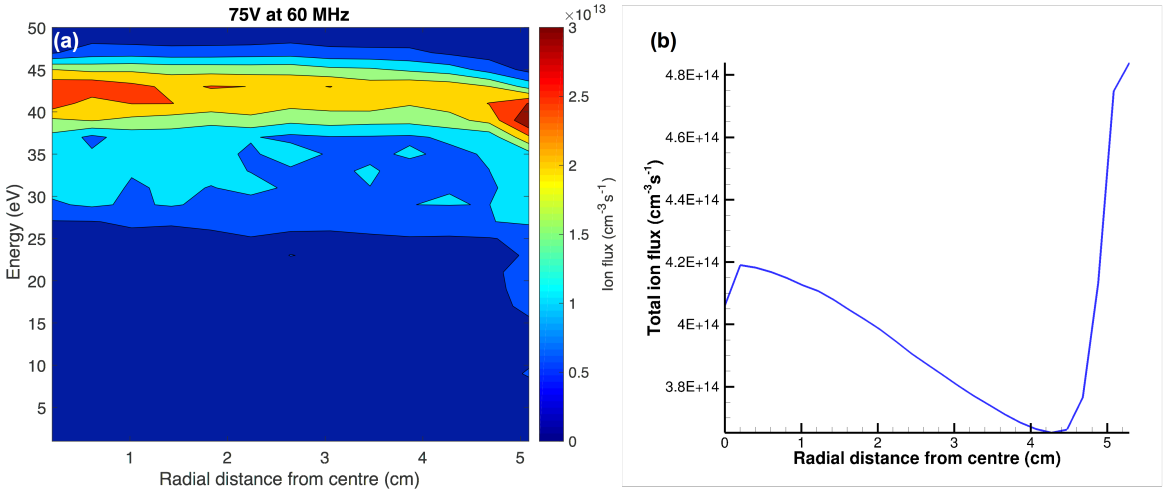

Figure 6.12: Ion energy and flux as a function of electrode radius for 75 V at 60 MHz in geometry 1.

From the voltage variation shown in figure 6.7 the 50 V example showed that the highest flux was in the 25 eV to 35 eV region of interest. A simulation was run at 50 V and 60 MHz in an attempt to narrow the spread of energies, this showed the densities of ions decreasing with time and it was clear that the plasma was not sustainable for these parameters. For this reason the voltage was increased and attempts were run at 5 V intervals until the plasma was sustainable at 75 V. The ion energy and flux from this simulation are shown in figure 6.12. The energy distribution is thin with the main flux between $\sim$ 38 eV and $\sim$ 47 eV over the majority of the electrode. Almost the entirety of the ions are above the 25 eV etching threshold for BeO, which should limit redeposition, nevertheless the flux is very inhomogeneous and with the energies high enough to etch the underlying mirror this would not be acceptable. The 50 V case not being sustainable indicates that the voltage and frequency parameters are not independent of each other, hence following both trends to obtain a perfect result is not possible; only general guidelines can be given. Again this points to optimisation only being possible when considering individual cases.

6.3 Influence of a magnetic field

Within ITER a principal challenge will be the magnetic fields, which are ever present within the device. As discussed in the introduction, the field magnitude at the edge of the reactor, where the first mirrors are to be located, is about 3.5 T. Simulating plasmas within magnetic fields is problematic as the cyclotron motion requires small-time steps, which increase the overall simulation time. In order to keep the run time of the simulation acceptable, the magnetic field simulated was kept at 100 G (0.01 T). This may be in excess of two orders of magnitude smaller than expected in practice but it still shows the significant changes that even a small static homogeneous vertical field induces.

Figure 6.13 (a) shows the reduction in energy of $\sim$ 20 eV for the ions across the electrode but the spread of energies remains almost the same as without a magnetic field (if comparing with the 13.56 MHz result in figure 6.9). The ion flux is completely different with the magnetic field, as is shown in figure 6.13 (b). Overall it is reduced to less than half of its non-magnetic field value, but the shape is also different. The peak in the centre of the electrode no longer exists and only the edge effects appear to remain. This is a consequence of a complete change in the distribution of the plasma, as shown in 6.14. A proposed

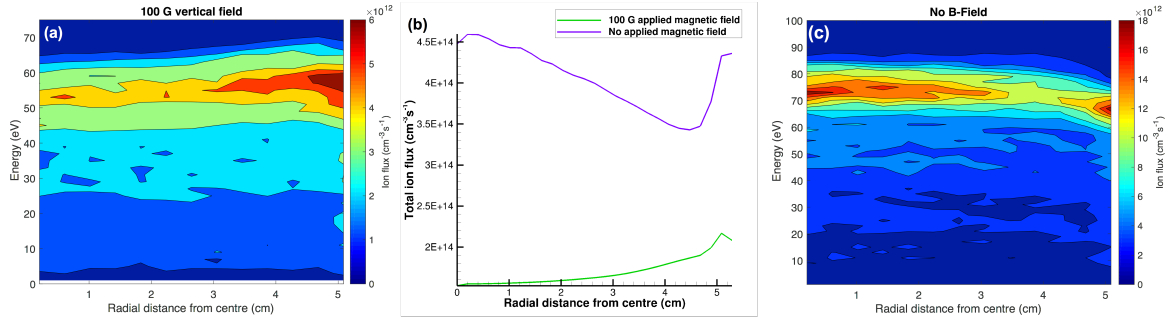

Figure 6.13: (a) Flux and energy as a function of radial distance from the centre of the electrode in geometry 1 at 13.56 MHz, 130 V, and 10 mTorr with a 100 G (0.01 T) vertical magnetic field. (b) The total ion flux on the lower electrode with and without the magnetic field. (c) Flux and energy as a function of radial distance for the same parameters but with no magnetic field.

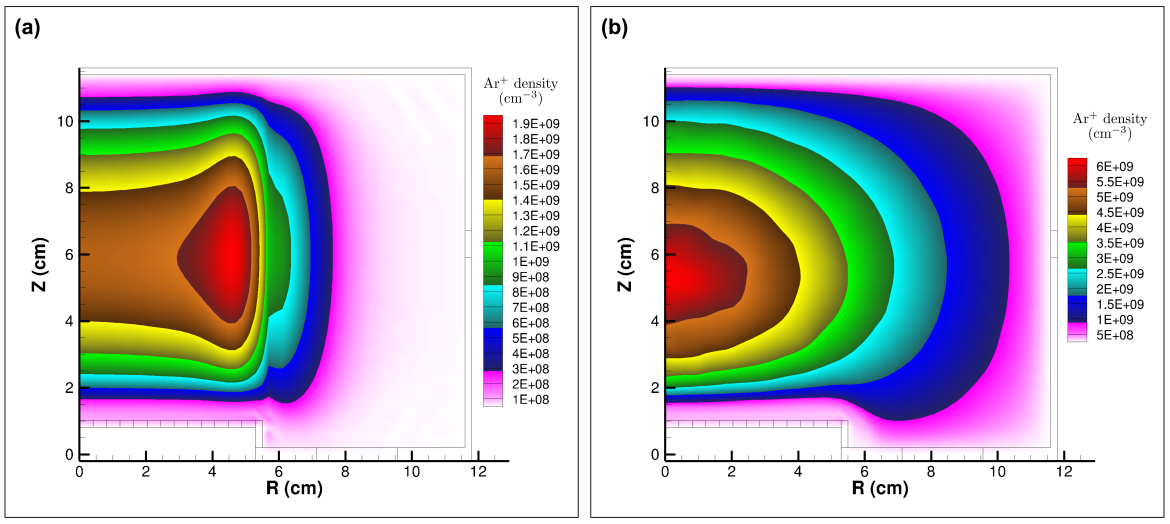

Figure 6.14: Ion densities in geometry 1 at 13.56 MHz, 130 V, and 10 mTorr. (a) Shows the densities with an applied 100 G magnetic field and (b) shows the same simulation without the applied field.

explanation for this is that the electrons cannot spread throughout the volume away from the areas of high density, as a result of being constrained to the magnetic field lines. The ions are still able to move but are strongly impeded and move outwards away from the higher densities, which has been shown at field strengths of up to 2.3 T [184].

In high fields and low pressures the formation of filamentary structures within the plasma is reported [184–186]. These are not seen in these simulations as they have not been encountered at low field strengths (< 0.9 T), but the cited works are significantly below the field strength within which the deposition removal process will be required to work. Moser has

also shown a single filamentary structure in the B-field chamber which brought about a massive peak in etch rate at the location of the filament [20]. A further important factor to consider is the direction of the field. Although not analysed in this work the angle of the field to the mirror will also change the plasma dynamics. This is important for ITER as the field orientation will be different for each first mirror.

Clearly a small vertical static B-field is able to cause significant changes in the plasma which are detrimental to etching. There are also indications that higher field strengths will induce filamentary structures which have been shown to cause localised etching. A detailed model is therefore needed to understand the effect of high magnetic fields in these low-temperature plasmas.

6.4 Summary and conclusions

- Experiments into the deposition removal are useful to determine the energies required to remove deposits, yet they cannot reasonably be used for all ITER geometries. Even the simple height change of the mirrors within the B-field geometry causes significant changes to the IEDFs.

- Maximum bias has been achieved in even the smallest of the simple geometries tested, nevertheless the bias cannot be the sole basis for determining the etch rates. Depending on distance and orientation of the ground, the homogeneity of the etch across the surface will change. Any plasma ignited above an appropriately biased surface will etch but there needs to be an appropriate ground for the field to bring the ions in.

- Edge effects are clearly an issue, and optimisation of this technique would depend heavily on the mirror assembly.

- Increasing the voltage would increase the etch but decrease uniformity.

- It is the same story for frequency although to a lesser extent as the bias voltage for a given input voltage would remain almost the same.

- 60 MHz is promising as a working frequency but there are engineering issues that must be considered. Higher frequencies cause heating in cables and the 1/4 wavelength installation option must be considered.

- It is possible to optimise the system for a given geometry but not possible to get a perfect homogeneous etch, thus keeping the ions below the etching threshold of the mirror is a good option. This would, however, reduce the etch rate significantly and could be an issue for the availability of the machine. Trends in frequency and voltage are not independent and would need to be calculated for individual geometries in order to reach optimal performance.

- Magnetic fields within ITER are an issue. Not withstanding the consideration that these fields will all be at different angles to the surface of the mirror, there is little understanding of the filamentary structures seen experimentally. Thomas et al. at the University of Auburn are currently working on simulating these structures using models, but no publication in relation to this has been published so far.

Modelling is certainly the correct direction for the prediction of reflectivity recovery through deposition removal. The tools currently available need development in order to fully understand the processes taking place. In their current state some qualitative analysis is possible and has been carried out. Fully quantitative optimisation may only be achieved through model development and individual analysis of each mirror. This is also true should attempts be made experimentally, individual analysis of every mirror would still be required and general trends from single experiments cannot be applied globally.

Chapter 7

Beryllium

7.1 Beryllium plasma chemistry

In order to simulate the effects of sputtering beryllium its gas chemistry must be formulated in order that once removed from the surface its behaviour within the plasma can be analysed. HPEM has never been used to study beryllium and so the gas chemistry data needed to be created as an input file in the correct format. Experimental data for beryllium cross sections does not exist in any ample quantity; this is due to its high toxicity and chemical reactivity, making it incredibly difficult to work with. The relevance of beryllium within fusion has caused an increase in activity surrounding the need for accurate modelling data. Cross sections for electron excitation [187–191], ionisation [191,192], and momentum transfer [191], have all been calculated through various methods. The most recent and demonstrably accurate data is from Zatsarinny and has been utilised in this work [191]. The full raw data provided through personal communication with Zatsirinny appears as plots in appendix B. In this chapter the supplied electron data is processed and heavy particle interactions are then calculated separately to form a Be gas chemistry set for inclusion within HPEM.

7.1.1 Lumping of energy levels

The Zatsirinny data consists of elastic cross sections for the first 19 states; the excitation cross sections from all of those states to all higher states (up to 4p 1P); ionisation cross sections for ground and the 2p 3P state; and momentum transfer for the ground state. This is a substantial amount of data and to optimise computational efficiency some of the energy levels that are very close can be lumped together. This is a common technique used within

Lumped state	Original states
BE	Ground
BE1	2p 3P
BE2	2p 1P
BE3	3s 3S, 3s 1S
BE4	1D2
BE5	3p 3P, 3p 1P
BE6	3P2
BE7	3d 3D, 3d 1D, 4d 3D, 4d 1D, 4f 3F, 4f 1F
BE8	4s 3S, 4s 1S
BE9	4p 3P, 4p 1P

Table 7.1: How the first 19 excited state cross sections of beryllium have been lumped for efficiency in the HPEM input file

low-temperature plasma modelling and was used to create the Ar, O, and Al chemistry sets previously used in this thesis [60–63]. In order to do this the cross sections for each level are simply summed to create a cross section for the lumped state; the threshold energy of the lumped state is the lowest threshold energy of the states that are lumped; the statistical weight ($g = 2j+1$) of the lumped state is the sum of the statistical weights of all the summed states; and for all the excited states there must be a super-elastic cross section to all lower states. Analysis of the Grotrian diagram for beryllium clearly shows which states can be lumped by proximity in energy level, and this has been done, as shown in table 7.1. The statistical weights of each state were taken from Fuhr [193].

7.1.2 Ionisation and momentum transfer

Also needed are the ionisation cross sections for each level. The data provided by Zatsirinny has these calculated for the first three states but not for any higher state. In order to account for ionisation from higher states the classical approach of Gryzinski was used [79, 194–197]. This method is built into the HPEM code as shown in equation 7.1.

$$\text{Cross-section} = \pi a_0^2 \times N_{eq} \times \left(\frac{E_{H,Thresh}}{E_{Thresh}}\right)^2 \times \frac{1}{U} \times \left(\frac{U-1}{U+1}\right)^{\frac{3}{2}} \times \left(1 + \frac{2}{3} \times \left(1 - \frac{1}{2U}\right) \times log(2.7 + \sqrt{U-1})\right) \quad (7.1)$$

In this equation $U = E/E_{Thresh}$ which is the incoming electron energy (E) over the threshold energy of ionisation for beryllium in its current excited state (E_{Thresh}); $E_{H,Thresh}$ is the

threshold ionisation energy of hydrogen; N_{eq} is the number of equivalent electrons that could undergo the reaction; and πa_0^2 is the area of the electron cloud of a hydrogen atom as seen by an incoming electron. As this approach is only being used for higher excited states, N_{eq} is set to 1 as only one electron is likely to be in the excited state and have this cross section. Threshold energies for ionisation for each excited state are the differences between the ionisation energy for the ground state and the energy of the current excited state. The πa_0^2 value is $8.79 \times 10^{-17} cm^{-2}$ and represents a conversion factor of the cross section.

Momentum transfer was given for the ground state but not for any of the higher states. There is no simple analytical method for calculating this cross section for these states but the elastic cross sections are given. With the assumption that the scattering is isotropic the elastic cross section can be used as the momentum transfer cross section.

7.1.3 Extrapolation to higher energies

Data for the cross sections has been given up to 110 eV and, as such, the higher energies must be accounted for through extrapolation of the data. It is known that dipole allowed transitions scale as $log(E)/E$ and this is the slowest at which these cross sections should decay with increasing energy [198]. For transitions that become less dipole like, the scaling first loses the $log(E)$ and becomes $1/E$, it then begins to pick up exponents and follows the trend $1/E^2$, $1/E^3$, $1/E^4$, etc... In order to extend the cross sections up into higher energies the final 20 % of the data was fitted with a straight line on a log-log plot, under the assumption that the decay will have begun by about 80 eV. In most cases the fits matched the data in the overlapping areas and merged well into the cross sections. In other cases the number of data points in the raw data was very small ($\sim$ 40 points) and the final few points had significant variation. For these cases it was impossible to get a completely smooth raw data to fit transition, but the difference in the fit and data is still very small. The final function of the fits was of the form $E^a + \exp(b)$, where a and b are constants, and was done in the curve fitting toolbox within Matlab. In order to check that the decays were in fact in line with the above decay rate they were checked for intercepts with $log(E)/E$. The lumped and fitted data is all shown in figures 7.1 to 7.10. These graphs show both the lumped data and the extrapolation fits for each of the cross sections that are input into the HPEM code.

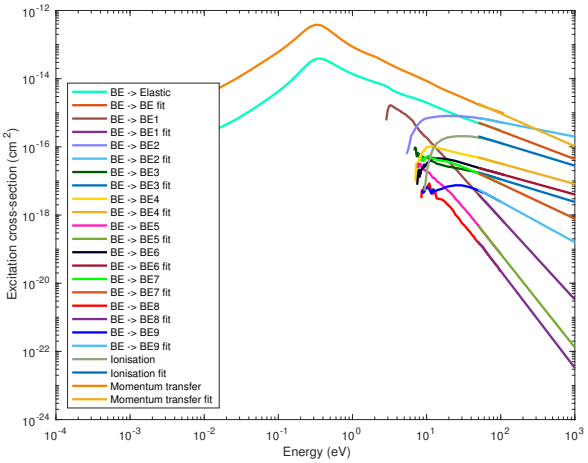

Figure 7.1: BE lumped state excitation cross sections

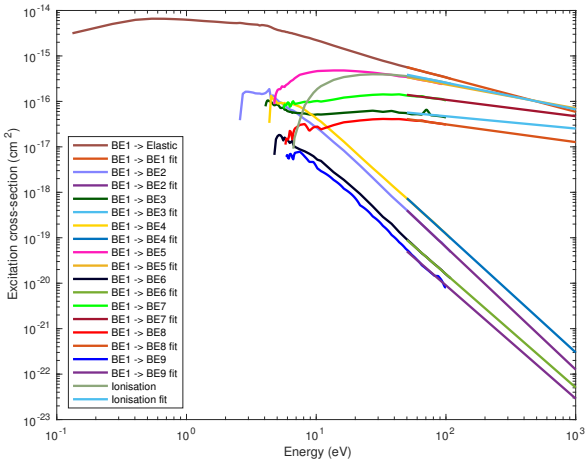

Figure 7.2: BE1 lumped state excitation cross sections

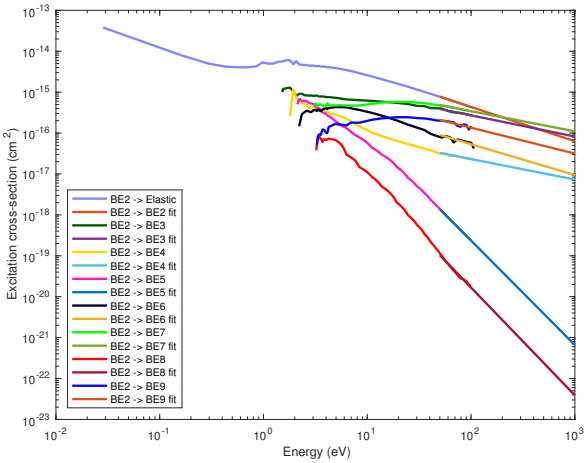

Figure 7.3: BE2 lumped state excitation cross sections

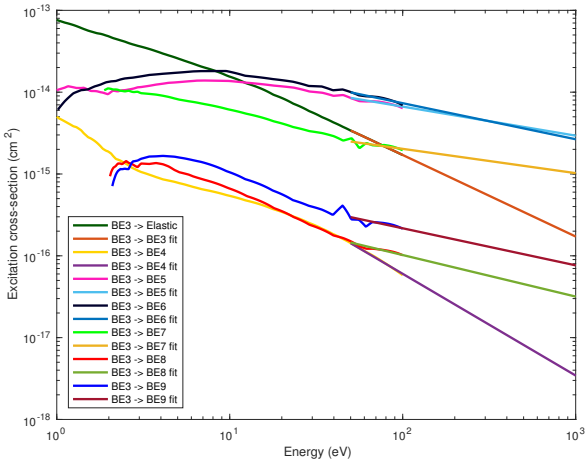

Figure 7.4: BE3 lumped state excitation cross sections

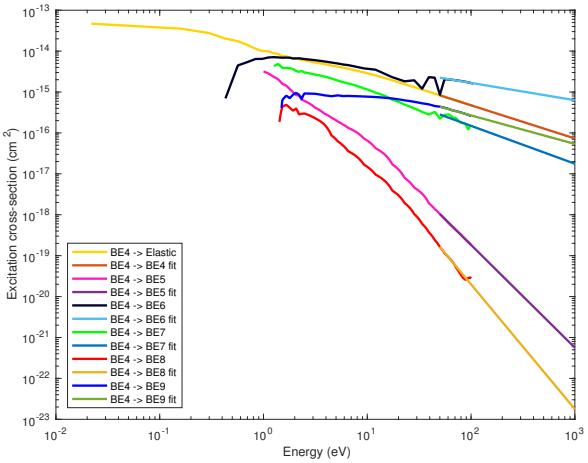

Figure 7.5: BE4 lumped state excitation cross sections

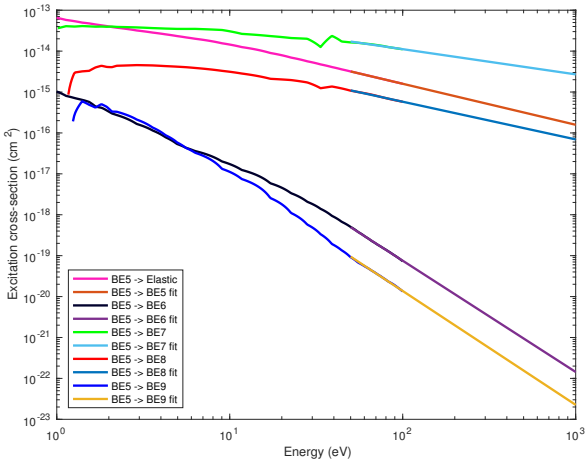

Figure 7.6: BE5 lumped state excitation cross sections

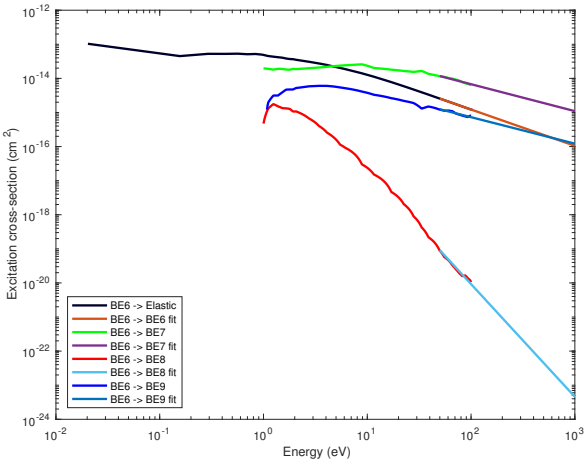

Figure 7.7: BE6 lumped state excitation cross sections

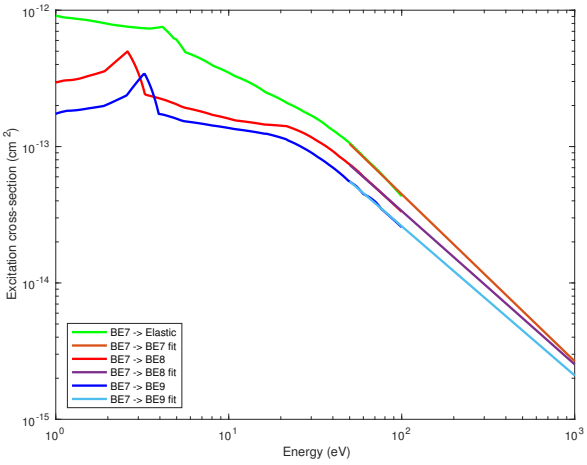

Figure 7.8: BE7 lumped state excitation cross sections

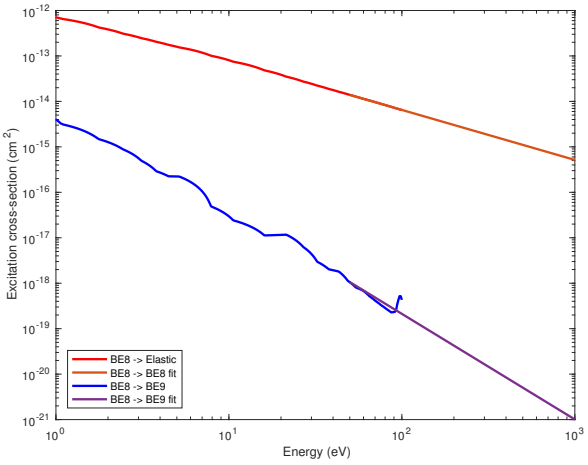

Figure 7.9: BE8 lumped state excitation cross sections

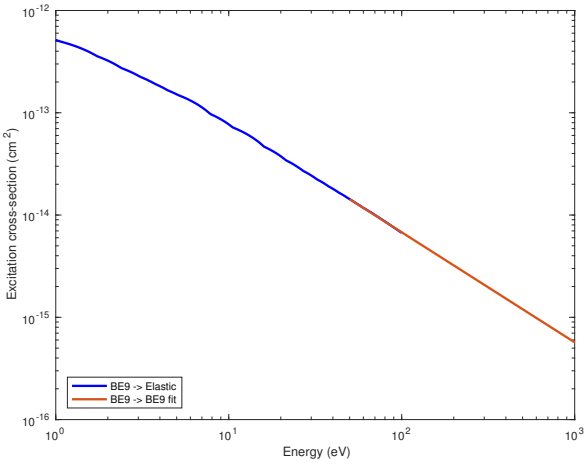

Figure 7.10: BE9 lumped state elastic cross section

7.1.4 Heavy particle interactions

With the electron interactions dealt with, the further task of heavy particle interaction was considered. Usually this would mean turning to chemical kinetics databases, such as NIST [199], or the recent QuantemolDB database [200], but only one reaction exists for Be in either database. To decide which reactions to include the Al chemistry was used as a template and the Langevin cross section σ_L for ion-neutral interactions was used [22].

$$\sigma_L = \left(\frac{\pi\alpha_p q^2}{\epsilon_0 m_R}\right)^{1/2} \frac{1}{v_R} \tag{7.2}$$

Within this α_p is the polarizability of the target atom which is a measure of how readily an electric field can distort the atom's charge distribution [201]; q is the charge of the incoming atom; m_R is the reduced mass of the two atoms ($m_1 m_2/m_1 + m_2$); and v_R is the relative velocity ($|\mathbf{v}_1 - \mathbf{v}_2|$). This cross section assumes that the ion is a point charge which can be considered accurate in most cases as the movement of the ion averages the charge to the centre [202]. For ionisation transfer reactions the cross section is halved giving a 50 % chance that either atom comes away from the reaction ionised. The rate of the reaction as a function of the temperature is

$$K(T) = \int_0^\infty f_m v_R \sigma_L(v_R) 4\pi v_R^2 dv_R \tag{7.3}$$

which includes the Maxwellian velocity distribution f_m as

$$f_m = \left(\frac{m_R}{2\pi kT}\right)^{3/2} exp\left(-\frac{m_R v_R^2}{2kT}\right) \tag{7.4}$$

This can then be fit as a power function and the coefficients can be used as inputs in Arrhenius form, shown in the Be/Ar/O gas chemistry reactions in table 7.2.

A further reaction to be calculated was the Penning ionisation rate. This involves an interaction between an excited atom and neutral in which the excited atom is quenched, the target atom is ionised, and an electron is released. The general form of the reaction is

$$A^* + B \rightarrow A + B^+ + e$$

The Langevin cross section cannot be used as it is only applicable for charge transfer from

already-ionised atoms to neutrals. Instead the cross section is calculated as follows.

$$\sigma_P = \pi R_0^2 \frac{n \exp^{-d\sqrt{E_i}}}{\sqrt{E_i} v r_B^2} 10^7 \tag{7.5}$$

The above equation, formulated by Hotop and Niehaus [203], is a simplified "billiard ball" collision of A* and B. R_0 is the combined radius of A and B ($r_A + r_B$) in Å, E_i is the ionisation potential of B in eV, v is the relative velocity in cm/s, n is the number of equivalent electrons in the outer shell of B, and d is the effective wall thickness if $R = R_0$ in Å. This effective wall thickness, d, is a measure of the potential barrier that an electron tunnels through from B to A. When compared with experiment the cross section of a reaction when A remains the same species the value of d does not change regardless of the target atom. So the value for d depends almost entirely on A, which is useful as it can be fixed and used to calculate cross sections between any target atom. That being the case, Be has no Penning cross section measurements and so the value of d cannot be gained from comparison. For the purposes of this work the value for d has been set at 60 % of R_0, which is through comparison of d for other species [204]. The process following the calculation of the cross section to output a rate is exactly the same as above using equations 7.3 and 7.4.

Species: Be, Ar, O, O_2, O_3, Ar_2^*, Ar^+, Be^+, O^+, O^-, O_2^-, O_3^-, $Be1$ to $Be9$ [a], Ar^*, O^*, e		
Reaction	Rate coefficient[b]	Ref.[c]
$e + Be \leftrightarrow Be + e$	$f\epsilon$	[191]
$e + Be \leftrightarrow Be1 + e$	$f\epsilon$	[191]
$e + Be \leftrightarrow Be2 + e$	$f\epsilon$	[191]
$e + Be \leftrightarrow Be3 + e$	$f\epsilon$	[191]
$e + Be \leftrightarrow Be4 + e$	$f\epsilon$	[191]
$e + Be \leftrightarrow Be5 + e$	$f\epsilon$	[191]
$e + Be \leftrightarrow Be6 + e$	$f\epsilon$	[191]
$e + Be \leftrightarrow Be7 + e$	$f\epsilon$	[191]
$e + Be \leftrightarrow Be8 + e$	$f\epsilon$	[191]
$e + Be \leftrightarrow Be9 + e$	$f\epsilon$	[191]
$e + Be \rightarrow Be^+ + e + e$	$f\epsilon$	[191]
$e + Be1 \leftrightarrow Be1 + e$	$f\epsilon$	[191]

$e + Be1 \leftrightarrow Be2 + e$	$f\epsilon$	[191]
$e + Be1 \leftrightarrow Be3 + e$	$f\epsilon$	[191]
$e + Be1 \leftrightarrow Be4 + e$	$f\epsilon$	[191]
$e + Be1 \leftrightarrow Be5 + e$	$f\epsilon$	[191]
$e + Be1 \leftrightarrow Be6 + e$	$f\epsilon$	[191]
$e + Be1 \leftrightarrow Be7 + e$	$f\epsilon$	[191]
$e + Be1 \leftrightarrow Be8 + e$	$f\epsilon$	[191]
$e + Be1 \leftrightarrow Be9 + e$	$f\epsilon$	[191]
$e + Be1 \rightarrow Be^+ + e + e$	$f\epsilon$	[191]
$e + Be2 \leftrightarrow Be2 + e$	$f\epsilon$	[191]
$e + Be2 \leftrightarrow Be3 + e$	$f\epsilon$	[191]
$e + Be2 \leftrightarrow Be4 + e$	$f\epsilon$	[191]
$e + Be2 \leftrightarrow Be5 + e$	$f\epsilon$	[191]
$e + Be2 \leftrightarrow Be6 + e$	$f\epsilon$	[191]
$e + Be2 \leftrightarrow Be7 + e$	$f\epsilon$	[191]
$e + Be2 \leftrightarrow Be8 + e$	$f\epsilon$	[191]
$e + Be2 \leftrightarrow Be9 + e$	$f\epsilon$	[191]
$e + Be2 \rightarrow Be^+ + e + e$	$f\epsilon$	[191]
$e + Be3 \leftrightarrow Be3 + e$	$f\epsilon$	[191]
$e + Be3 \leftrightarrow Be4 + e$	$f\epsilon$	[191]
$e + Be3 \leftrightarrow Be5 + e$	$f\epsilon$	[191]
$e + Be3 \leftrightarrow Be6 + e$	$f\epsilon$	[191]
$e + Be3 \leftrightarrow Be7 + e$	$f\epsilon$	[191]
$e + Be3 \leftrightarrow Be8 + e$	$f\epsilon$	[191]
$e + Be3 \leftrightarrow Be9 + e$	$f\epsilon$	[191]
$e + Be3 \rightarrow Be^+ + e + e$	$f\epsilon$	[191]
$e + Be4 \leftrightarrow Be4 + e$	$f\epsilon$	[191]
$e + Be4 \leftrightarrow Be5 + e$	$f\epsilon$	[191]
$e + Be4 \leftrightarrow Be6 + e$	$f\epsilon$	[191]
$e + Be4 \leftrightarrow Be7 + e$	$f\epsilon$	[191]
$e + Be4 \leftrightarrow Be8 + e$	$f\epsilon$	[191]
$e + Be4 \leftrightarrow Be9 + e$	$f\epsilon$	[191]

$e + Be4 \rightarrow Be^{+} + e + e$	$f\epsilon$	[191]
$e + Be5 \leftrightarrow Be5 + e$	$f\epsilon$	[191]
$e + Be5 \leftrightarrow Be6 + e$	$f\epsilon$	[191]
$e + Be5 \leftrightarrow Be7 + e$	$f\epsilon$	[191]
$e + Be5 \leftrightarrow Be8 + e$	$f\epsilon$	[191]
$e + Be5 \leftrightarrow Be9 + e$	$f\epsilon$	[191]
$e + Be5 \rightarrow Be^{+} + e + e$	$f\epsilon$	[191]
$e + Be6 \leftrightarrow Be6 + e$	$f\epsilon$	[191]
$e + Be6 \leftrightarrow Be7 + e$	$f\epsilon$	[191]
$e + Be6 \leftrightarrow Be8 + e$	$f\epsilon$	[191]
$e + Be6 \leftrightarrow Be9 + e$	$f\epsilon$	[191]
$e + Be6 \rightarrow Be^{+} + e + e$	$f\epsilon$	[191]
$e + Be7 \leftrightarrow Be7 + e$	$f\epsilon$	[191]
$e + Be7 \leftrightarrow Be8 + e$	$f\epsilon$	[191]
$e + Be7 \leftrightarrow Be9 + e$	$f\epsilon$	[191]
$e + Be7 \rightarrow Be^{+} + e + e$	$f\epsilon$	[191]
$e + Be8 \leftrightarrow Be8 + e$	$f\epsilon$	[191]
$e + Be8 \leftrightarrow Be9 + e$	$f\epsilon$	[191]
$e + Be8 \rightarrow Be^{+} + e + e$	$f\epsilon$	[191]
$e + Be9 \leftrightarrow Be9 + e$	$f\epsilon$	[191]
$e + Be9 \rightarrow Be^{+} + e + e$	$f\epsilon$	[191]
$Be^{1} \rightarrow Be$	4.2×10^{-1}	[199]
$Be^{2} \rightarrow Be^{1}$	1×10^{-6}	[199]
$Be^{2} \rightarrow Be$	5.52×10^{8}	[199]
$Be^{3} \rightarrow Be^{2}$	1×10^{7}	[199]
$Be^{3} \rightarrow Be^{1}$	1×10^{7}	[199]
$Be^{3} \rightarrow Be$	1×10^{-6}	[199]
$Be^{4} \rightarrow Be^{3}$	1×10^{-6}	[199]
$Be^{4} \rightarrow Be^{2}$	1×10^{5}	[199]
$Be^{4} \rightarrow Be^{1}$	1×10^{-6}	[199]
$Be^{4} \rightarrow Be$	1×10^{-6}	[199]
$Be^{5} \rightarrow Be^{4}$	1×10^{5}	[199]

$Be^5 \rightarrow Be^3$	1×10^7	[199]
$Be^5 \rightarrow Be^2$	1×10^{-6}	[199]
$Be^5 \rightarrow Be^1$	1×10^{-6}	[199]
$Be^5 \rightarrow Be$	1×10^6	[199]
$Be^6 \rightarrow Be^5$	1×10^{-6}	[199]
$Be^6 \rightarrow Be^4$	1×10^{-6}	[199]
$Be^6 \rightarrow Be^3$	1×10^{-6}	[199]
$Be^6 \rightarrow Be^2$	1×10^{-6}	[199]
$Be^6 \rightarrow Be^1$	1.41×10^8	[199]
$Be^6 \rightarrow Be$	1×10^{-6}	[199]
$Be^7 \rightarrow Be^6$	1×10^{-6}	[199]
$Be^7 \rightarrow Be^5$	1×10^6	[199]
$Be^7 \rightarrow Be^4$	1×10^{-6}	[199]
$Be^7 \rightarrow Be^3$	1×10^{-6}	[199]
$Be^7 \rightarrow Be^2$	2×10^7	[199]
$Be^7 \rightarrow Be^1$	5×10^7	[199]
$Be^7 \rightarrow Be$	1×10^{-6}	[199]
$Be^8 \rightarrow Be^7$	1×10^{-6}	[199]
$Be^8 \rightarrow Be^6$	1×10^{-6}	[199]
$Be^8 \rightarrow Be^5$	2×10^6	[199]
$Be^8 \rightarrow Be^4$	1×10^{-6}	[199]
$Be^8 \rightarrow Be^3$	1×10^{-6}	[199]
$Be^8 \rightarrow Be^2$	5×10^6	[199]
$Be^8 \rightarrow Be^1$	2×10^6	[199]
$Be^8 \rightarrow Be$	1×10^{-6}	[199]
$Be^9 \rightarrow Be^8$	1×10^5	[199]
$Be^9 \rightarrow Be^7$	1×10^6	[199]
$Be^9 \rightarrow Be^6$	1×10^{-6}	[199]
$Be^9 \rightarrow Be^5$	1×10^{-6}	[199]
$Be^9 \rightarrow Be^4$	5.2×10^5	[199]
$Be^9 \rightarrow Be^3$	2×10^5	[199]
$Be^9 \rightarrow Be^2$	1×10^{-6}	[199]

$Be^9 \rightarrow Be^1$	1×10^{-6}	[199]
$Be^9 \rightarrow Be$	1.2×10^5	[199]
$Be^* + Be \rightarrow Be + Be$	2.4×10^{-11}	[22, 199, 201]^d
$Be^* + Be \rightarrow Be + Be^*$	1.2×10^{-11}	[22, 199, 201]^d
$Be^+ + Be \rightarrow Be + Be^+$	1.2×10^{-11}	[22, 199, 201]^d
$Be^+ + Be1 \rightarrow Be + Be^+$	1.2×10^{-11}	[22, 199, 201]^d
$Be^+ + Be2 \rightarrow Be + Be^+$	1.2×10^{-11}	[22, 199, 201]^d
$Be^+ + Be3 \rightarrow Be + Be^+$	1.2×10^{-11}	[22, 199, 201]^d
$Be^+ + Be4 \rightarrow Be + Be^+$	1.2×10^{-11}	[22, 199, 201]^d
$Be^+ + Be5 \rightarrow Be + Be^+$	1.2×10^{-11}	[22, 199, 201]^d
$Be^+ + Be6 \rightarrow Be + Be^+$	1.2×10^{-11}	[22, 199, 201]^d
$Be^+ + Be7 \rightarrow Be + Be^+$	1.2×10^{-11}	[22, 199, 201]^d
$Be^+ + Be8 \rightarrow Be + Be^+$	1.2×10^{-11}	[22, 199, 201]^d
$Be^+ + Be9 \rightarrow Be + Be^+$	1.2×10^{-11}	[22, 199, 201]^d
$Be^+ + Ar \rightarrow Be + Ar^+$	$1.59 \times 10^{-11} \exp(74698/T_g)$	[22, 199, 201]^d
$Be1 + Ar \rightarrow Ar^+ + Be + e$	$1.59 \times 10^{-11} \exp(150858/T_g)$	[22, 199, 201]^d
$Be2 + Ar \rightarrow Ar^+ + Be + e$	$1.59 \times 10^{-11} \exp(121847/T_g)$	[22, 199, 201]^d
$Be3 + Ar \rightarrow Ar^+ + Be + e$	$1.59 \times 10^{-11} \exp(107922/T_g)$	[22, 199, 201]^d
$Be4 + Ar \rightarrow Ar^+ + Be + e$	$1.59 \times 10^{-11} \exp(100959/T_g)$	[22, 199, 201]^d
$Be5 + Ar \rightarrow Ar^+ + Be + e$	$1.59 \times 10^{-11} \exp(98638/T_g)$	[22, 199, 201]^d
$Be6 + Ar \rightarrow Ar^+ + Be + e$	$1.59 \times 10^{-11} \exp(97478/T_g)$	[22, 199, 201]^d
$Be7 + Ar \rightarrow Ar^+ + Be + e$	$1.59 \times 10^{-11} \exp(93996/T_g)$	[22, 199, 201]^d
$Be8 + Ar \rightarrow Ar^+ + Be + e$	$1.59 \times 10^{-11} \exp(90515/T_g)$	[22, 199, 201]^d
$Be9 + Ar \rightarrow Ar^+ + Be + e$	$1.59 \times 10^{-11} \exp(87033/T_g)$	[22, 199, 201]^d
$Be^+ + O \rightarrow Be + O^+$	$9.2 \times 10^{-12} \exp(49847/T_g)$	[22, 199, 201]^d
$Ar^+ + Be \rightarrow Ar + Be^+$	1.2×10^{-11}	[22, 199, 201]^d
$Ar^+ + Be^* \rightarrow Ar + Be^+$	1.2×10^{-11}	[22, 199, 201]^d
$O^+ + Be \rightarrow O + Be^+$	1.2×10^{-11}	[22, 199, 201]^d
$O^+ + Be^* \rightarrow O + Be^+$	1.2×10^{-11}	[22, 199, 201]^d
$O_2^+ + Be \rightarrow O + O + Be^+$	9.17×10^{-12}	[22, 199, 201]^d
$O_2^+ + Be^* \rightarrow O + O + Be^+$	9.17×10^{-12}	[22, 199, 201]^d

$Ar_2^+ + Be \rightarrow Ar + Ar + Be^+$	4.58×10^{-11}	$[22, 199, 201]^d$
$Ar_2^+ + Be^* \rightarrow Ar + Ar + Be^+$	4.58×10^{-11}	$[22, 199, 201]^d$
$Ar^* + Be \rightarrow Be^+ + Ar + e$	1.59×10^{-11}	$[22, 199, 201, 203]^{ed}$
$Ar_2^* + Be^* \rightarrow Be^+ + Ar + Ar + e$	2.75×10^{-12}	$[22, 199, 201, 203]^{ed}$
$Ar_2^* + Be \rightarrow Be^+ + Ar + Ar + e$	2.75×10^{-12}	$[22, 199, 201, 203]^{ed}$
$O^- + Be^+ \rightarrow O + Be$	1×10^{-7}	EST^{ed}
$O_2^- + Be^+ \rightarrow O_2 + Be$	1×10^{-7}	EST^{ed}
$O_3^- + Be^+ \rightarrow O_3 + Be$	1×10^{-7}	EST^{ed}

[a] The lumped excited states of Be are detailed in table 7.1. Be^* is representative of any excited state.
[b] Rate coefficients are in units of $cm^3 s^{-1}$ unless otherwise stated. $f\epsilon$ indicates that the rate coefficients have been calculated from the electron energy distribution within the eMCS. T_g is the gas temperature (K).
[c] References for the heavy particle reactions refer to the sources for the atomic properties used within the calculation for the Arrhenius coefficient and the threshold energy.
[d] Adjusted to gas temperature by $T_g^{0.5}$.

Table 7.2: Argon, oxygen, and beryllium gas phase reactions and rate coefficients. These are only the reactions involving beryllium as the argon and oxygen chemistry remain the same as in table 3.2.

In the reaction rates there is a threshold energy at which the reaction can take place which is dependent on the ionisation potential of the two involved atoms. If the incoming ion has a lower ionisation potential than the target neutral, then the threshold energy is the gap between the two potentials. If the incoming ion has a higher ionisation potential than the target neutral, then there is no threshold energy. Be has a low ionisation potential so there is a high threshold energy for it to ionise the Ar or O atoms in the gas. The reactions shown in table 7.2 replace the Al reactions used in the Al/Ar/O gas chemistry from table 3.2, yet the Ar/O reactions remain the same and are not shown.

7.2 Modelling comparisons with aluminium

How changing from Al to Be will influence the plasma is important to investigate, so two almost identical simulations were run. Geometry 1 was run in Ar with a 130 V 13.56 MHz supply, no B-field, and at 10 mTorr. These parameters were the same for both simulations, though for one simulation the electrode provided a flux of Al and in the other it provided a

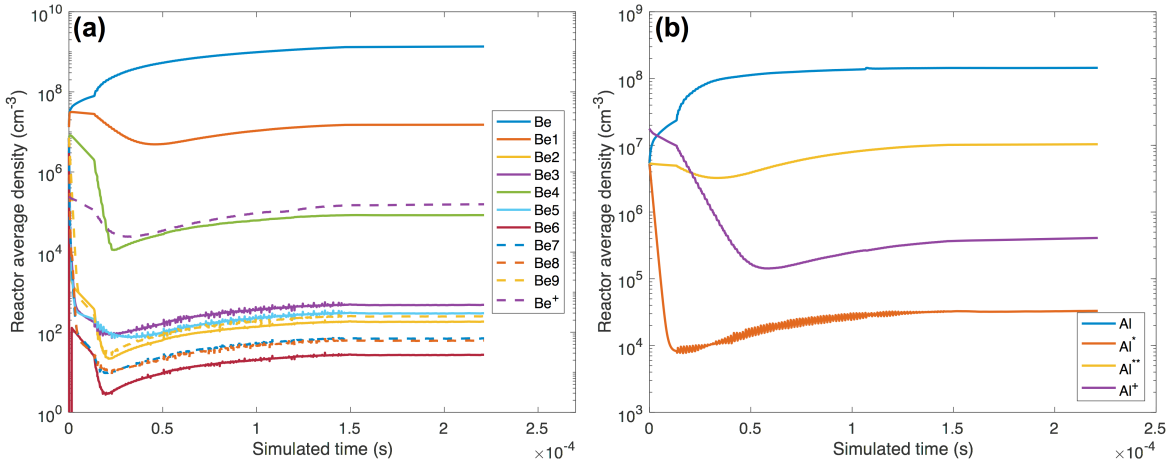

Figure 7.11: Reactor averaged densities of (a) Be and (b) Al showing steady state has been reached.

flux of Be. This was achieved simply through adding a 20 % probability of any ion impacting the surface releasing Al/Be or an O. The ion itself also came back neutralised. Comparisons of the plasma parameters showed identical results, indicating that regardless of the element being produced the plasma remained the same owing to the comparatively small number of particles. In both cases Ar densities were 10^{14}, and maximum Ar^{+} densities were 10^{10}, both being four orders of magnitude higher than the comparative Be or Al densities as shown in figure 7.11.

From figure 7.12 the densities of the neutral, highest density excited state, and ionised state are shown for Be and Al. From this it can be seen that although Al has not diffused into the reactor to the same degree as the Be, it does have a slightly higher density of ions. This is due to the lower energy required to ionise Al (9.3 eV for Be and 6 eV for Al). In figure 7.11 the overall total density of Be is greater than that of Al. With the surface of the electrode being the only production mechanism and the gas outlet being the only destruction mechanism, one or both of these must be responsible. The flux of total ions to the surface in the simulations is exactly the same and the flux of Be and Al from the surface is also the same. This rules out the production mechanism as being the root cause of the density differences, it must be the gas outlet. From figure 7.12 it can be seen that the neutral Al remains close to the surface of the electrode as a result of to the mass of Al being much greater than that of Be and the diffusion coefficient being proportional to $\sqrt{1/M_{Ar} + 1/M_{Al/Be}}$ (0.25 for Al in Ar, 0.37 for Be in Ar). With the neutral Al remaining near the electrode surface and the bottom of the reactor, the neutral Al is more likely to swept out of the reactor through the

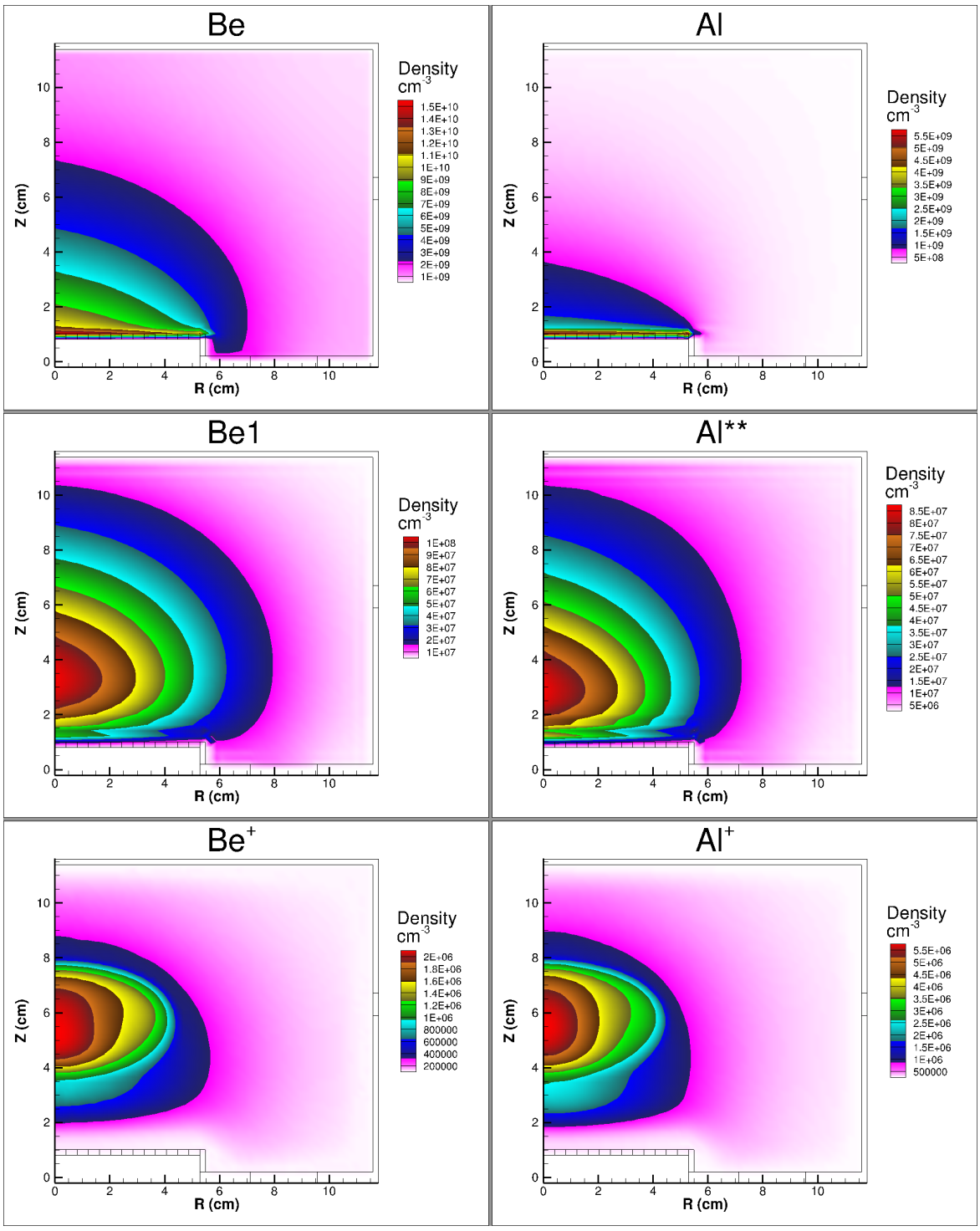

Figure 7.12: Densities of Be and Al states within otherwise identical plasmas. In both cases the flux of particles from the surface is exactly the same. The system is at 10 mTorr, 130 V, 13.56 MHz, in geometry 1 with no B-field.

outlet. It is important to mention here that in these simulations the pressure is maintained through the flow of the gas exiting the reactor. Both the flow in and the pressure are set variables within the input files; the outlet varies its flow to maintain pressure.

7.3 Summary and conclusions

- Electron impact cross sections have been lumped and extrapolated to be inserted within HPEM.
- The heavy particle interactions have been calculated using theoretical equations for cross sections and subsequently the rate equations.
- The full Be chemistry set has been incorporated into the Ar/O chemistry set used in previous chapters of this thesis. This has been used to run a Be simulation in comparison with an identical Al simulation, which has shown various differences in the way Al and Be behave within a plasma. Minimal effect on the overall plasma has been seen but overall densities of Al and Be differ by an order of magnitude. This has been tied to the diffusion of the two within the gas and the location of the gas outlet.
- As the SKM was shown to be giving poor results in chapter 5 any future modelling work should remove the SKM as a module and instead use a table of energy dependant sputtering rates. This would both speed up the simulation, with the SKM being the most computationally expensive element, and also potentially give more physically accurate results.

How the Al and Be behave within the plasma will change how the etching process occurs. With the higher density of neutrals near the surface for Al there may be significant redeposition, in comparison with the Be which diffuses more completely into the plasma bulk. With the gas flow in this simple reactor proven to be important, as shown by the overall densities, this must be taken into consideration when this method is employed on ITER. It could also be that only the increased residence time of Be within the chamber allows more opportunities for it to re-deposit. These are all variables that must be considered to gain a full working understanding of the method.

Chapter 8

Atmospheric modification of a polymer surface

The following chapter stands alone from the rest of this thesis. It is work that was carried out during the initial stages of the Ph.D as a continuation of work that had beginnings in a masters thesis. This new work was begun when the atmospheric pressure plasma jet was still seen as a possible deposition removal tool. When it became clear that the atomic oxygen produced by the jet would not be welcome within a fusion device, in any quantity, the plasma jet method was disregarded. However interest in the treatment of polymer films remained and hence this investigation was completed and published in Plasma Sources Science and Technology in 2016 [1].

As four authors are listed it is important to distinguish between my work and that of the other authors, and is as follows: E. Wagenaars supervised the project; A. West assisted with the set up and use of the laboratory equipment in the initial stages of the investigation; J. Bredin produced the TALIF results shown in figure 8.7; and I obtained and analysed all other results.

8.1 Introduction

Polypropylene (PP) is a thermoplastic with good heat, fatigue, and chemical resistance. It also remains translucent while being semi-rigid. This makes it very useful in applications such as food containment, textiles, packaging, and surgical implants [205]. The drawback, for some manufacturers that wish to adhere inks or glues to the polymer surface, is that these

polymers have low wettability. To combat this; the industries involved are operating non-thermal plasmas to improve the polymers surface properties and allow for better adhesion or biocompatibility [206, 207]. The plasma treatment only has an effect on the surface, and thus does not change the useful bulk properties of the material.

Over the years, many different plasma sources, operated under a range of conditions, have been used for surface modification of polymer films. Despite the significant differences that exist between these plasma sources, and more importantly their plasma properties, similar treatment effects can be achieved in terms of change in wettability. It has been suggested that the reason why polymer films have such low adhesion is due to a lack of surface polar groups [208]. So the plasmas increase the surface energy by either breaking polar bonds and leaving polar end groups, or by adding polar groups to the surface. This is an established general concept, however, there has been very little work that has linked the properties of the plasma with surface energy changes. Therefore, details on how the plasma breaks and adds bonds on the polymer surface are largely unknown, making optimisation of the plasma device an empirical and time-consuming process. Traditionally there have been low pressure treatments [209–212], but more recently there has been a focus on atmospheric pressure devices such as dielectric barrier discharge [213–216], coronal discharge [217], atmospheric glow discharge [218], or Atmospheric-Pressure Plasma Jets (APPJs) [219–224]. It is worth noting that all of this work has been done with devices where the plasma is in contact with the polymer surface. In this work we aim to study the mechanisms underpinning the modification of PP surface using atmospheric-pressure plasmas. For this we reduce the complexity of the plasma that is treating the sample by using the effluent of a cross-field APPJ device. Here, there is no direct contact between the active plasma and the PP surface. Only the neutral radical-rich effluent reaches the polymer, there are no charged particles or electric fields impinging on the surface. We are therefore able to isolate effects on the PP surface arising from radical species, excluding ion bombardment, charging and electric field effects.

8.2 Methods

8.2.1 Treatment of polypropylene films

The plasma device used in this investigation was an atmospheric-pressure plasma jet (APPJ) shown in figure 4.6 and generally discussed in section 4.2. It consists of two stainless steel electrodes and two quartz glass plates that form a 1 x 1 x 30 mm channel. A mixture of helium at 1 standard litre per minute, and oxygen at varying admixture percentages from 0.2 % up to 1 %, flows down the channel. One of the electrodes is driven via a matching network with radio frequency voltage of 13.56 MHz. The other electrode is grounded and plasma is formed across the channel. It is worth noting that the electric field created between the electrodes is perpendicular to the gas flow, meaning there are no significant electric fields present in the effluent of the APPJ. When the plasma leaves the end of the device and enters into open air it recombines very close to the nozzle due to the highly collisional environment at atmospheric pressure and the cross-field arrangement of the driving electric field. This leaves only a neutral, radical rich effluent for the surface treatments. For the experiments the APPJ is mounted on three axis motorised stages (Zaber T-LSM050A), and is pointed vertically downwards towards a polymer sample causing the effluent to impinge on the surface. Along with the O_2 percentage, the distance between the exit of the APPJ and the sample surface was varied, as was treatment time. The input power from the generator was kept constant at 30 W_{net}, though with losses through the matching network, the power dissipated in the plasma is much smaller, in the order of a few Watts.

The polymer films used throughout this investigation were PP with a thickness of 100 μm (Goodfellow Cambridge Ltd). A jig was constructed to hold the polymer beneath the APPJ for consistent location of treatment. For short treatment times (< 2 s) the APPJ was scanned along the surface at a calculated constant speed using the aforementioned motorised axial stages.

The density of atomic oxygen in the APPJ effluent was measured using two-photon absorption laser-induced fluorescence (TALIF) spectroscopy. The atomic oxygen TALIF scheme used for the measurements is discussed in detail by Niemi et al. [225] In short, two UV-photons at 225.65 nm are simultaneously absorbed to excite oxygen atoms from the $2p^4\ ^3P_2$ ground state into the $3p\ ^3P_{1,2,0}$ excited state. This subsequently decays, partially through optical transitions to the $3s\ ^3S$ state by emitting a near-infrared photon at 844.87 nm

as described by Niemi et al. and Knake et al. [226] The effective collisional-induced quenching rate is estimated using radiative lifetimes and quenching coefficients from [225], assuming the feedstock gases are the sole quenching partners at 300 K. This provides estimates of relative ground state atomic oxygen density.

8.2.2 Surface characterisation

The surface modification was monitored using a contact angle analyser (Dyne Technology, Theta Lite) which measures changes in wettability through the static sessile drop method. It consists of a camera that looks across the treated surface, and a needled syringe that creates controlled volume droplets which are placed onto the surface from above. The camera records images of the droplet which are used to calculate the contact angle between the liquid and the treated surface. Each recorded droplet consisted of 24 individual images which were individually analysed for their contact angles. An average result was obtained per droplet with the standard deviation. Each treatment was repeated and analysed a minimum of three times and weighted mean was calculated. The standard deviation of the mean is given as the error and is propagated through further calculations. Two liquids were used; deionised water, and diiodomethane (Sigma-Aldrich). The calculation of the surface energy was performed using the Owens-Wendt-Rabel-Kaelble (OWRK) method [227]. This method uses the difference between the polar and dispersive components of the two liquids. All liquids have a dispersive component, deionised water is a polar liquid and thus it also has available polar bonds. Diiodomethane is non-polar and thus has no available polar bonds. The dispersive component is mechanical and based around the van der Waals force. The polar component is chemical and reveals polar end bonds available for the liquid on the surface. This allows us to characterise whether the changes in contact angle being seen are due to a mechanical roughening, or a molecular scale chemical reaction on the surface.

To analyse the chemistry on the surface Attenuated Total Reflectance Fourier Transform Infrared spectroscopy (ATR-FTIR, Thermo Scientific Nicolet iS50) was used. The sample is mounted on a diamond holder and a beam of IR light is totally internally reflected within the crystal. An evanescent wave extends beyond the interface and into the sample and is attenuated by regions that absorb the energy of the wave. This is then passed into the internally reflected beam and on to an IR spectrometer for analysis.

8.3 Results

8.3.1 APPJ operational parameter variations

In order to investigate the underpinning physics of the APPJ treatment of a PP surface, we measured contact angle while varying three operational parameters of the APPJ, oxygen admixture, treatment time, and distance.

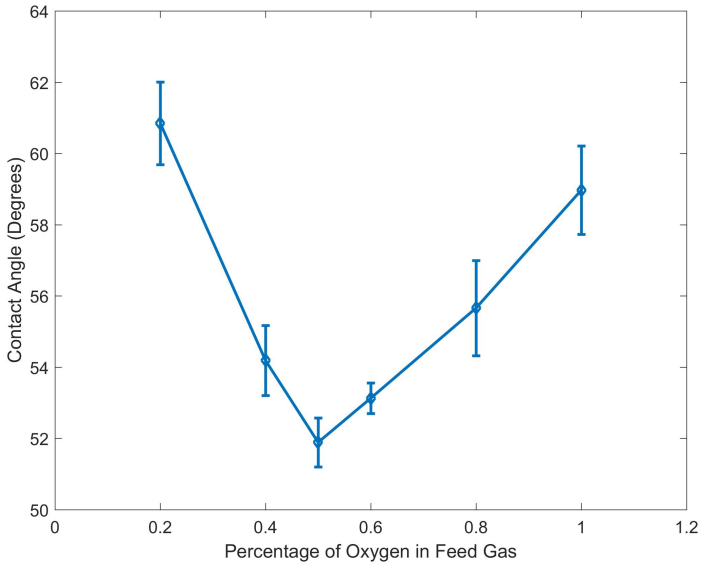

Figure 8.1: Contact angle changes as a function of percentage of O_2 admixture in the feed gas after 30 seconds of treatment time. The untreated PP was measured to have a contact angle of 93.9°

When varying the oxygen admixture in the feed gas the APPJ was placed at 15 mm above the sample surface. Figure 8.1 shows the measured contact angle after the treatment for various oxygen admixtures. For all admixtures there is a significant reduction in contact angle compared to the untreated PP, which has a contact angle of 93.9°. Despite the fact that our plasma jet only provides neutral radicals and no charged particles or electric fields, we observe changes in contact angle from 93.9° to 51.9° in 30 s. This is similar to other APPJ treatments such as the 52.0° achieved by Kostov [220]. Nevertheless, there is a clear difference in the treatment effect with the largest change in contact angle, after 30 seconds of treatment time, with 0.5 % oxygen. Increasing the oxygen percentage above 0.5 % leads to a reduced effect of the treatment.

Figure 8.2 shows the measured contact angle as a function of treatment time while keeping

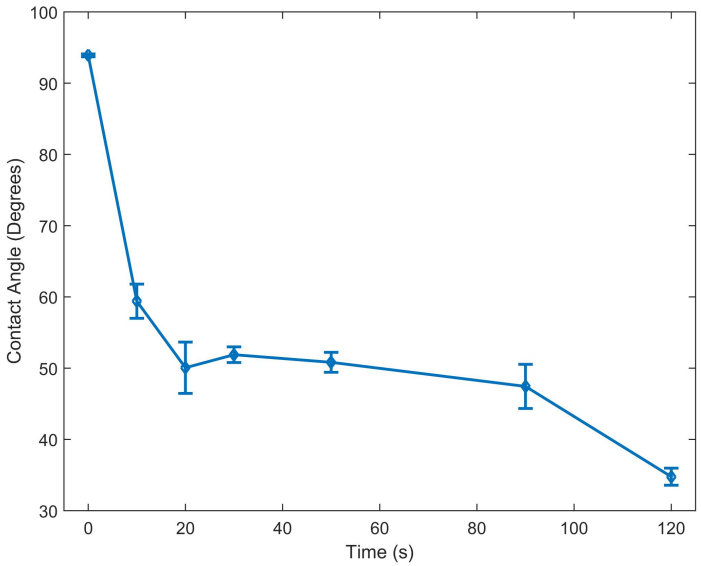

Figure 8.2: Contact angle changes with APPJ treatment time for PP with 0.5 % O_2 in the feed gas and a distance of 15 mm

the distance and oxygen percentage constant. It is clear that there is a very rapid decrease in contact angle during the first 10 seconds, with a further, much slower reduction in contact angle between 20 and 120 seconds. The decreasing trend suggests that a further reduction can be expected for treatment times beyond 120 sec. To investigate the initial, sharp decrease in contact angle further, we performed plasma treatments between 0.2 and 2 seconds as shown in figure 8.3. Here we observe a very fast drop in contact angle from 93.9° to 70.1° in only 1.5 seconds. This means 40 % of the total contact angle reduction happens in the first 1.5 seconds. It seems that there are two processes at play that both result in a reduction of contact angle. One is fast, reaching its maximum effect after 1.5 sec, while the second is much slower but continues for at least 120 seconds.

The final operational parameter that was investigated was the distance between the nozzle of the APPJ and the surface of the PP film. The O_2 admixture was kept at the optimum of 0.5 %, while for various distances we recorded the treatment effect as function of time. The results are shown in figure 8.4. For short distances, 3 to 15 mm, we again observe a two-stage decrease in contact angle, a rapid decrease $<$ 10 seconds and a more gradual, continuing decrease 20 - 120 seconds. For larger distances 30 and 50 mm, there appears to only be the slow, gradual decrease. It is interesting to note that all distances below 15 mm have a very similar effect for each treatment time while for distances larger than 15 mm

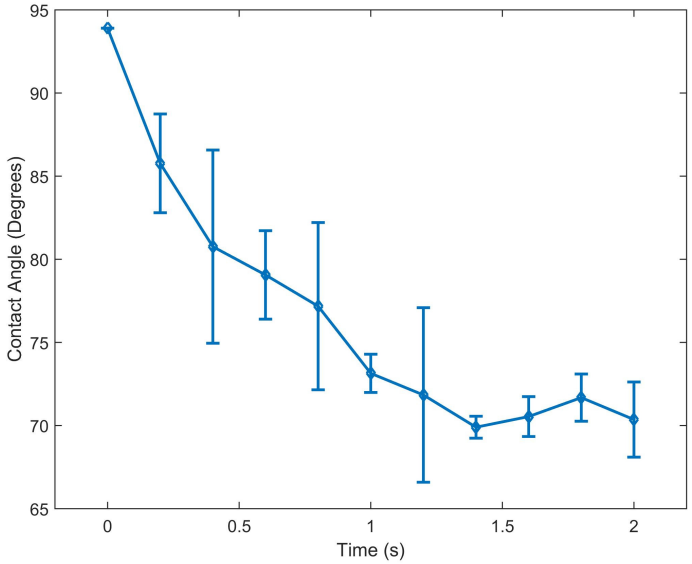

Figure 8.3: Contact angle changes with short APPJ treatment time for PP with 0.5 % O_2 in the feed gas and a distance of 15 mm between the APPJ and the PP surface

there is a clear decrease in effect for increasing distance at any given treatment time.

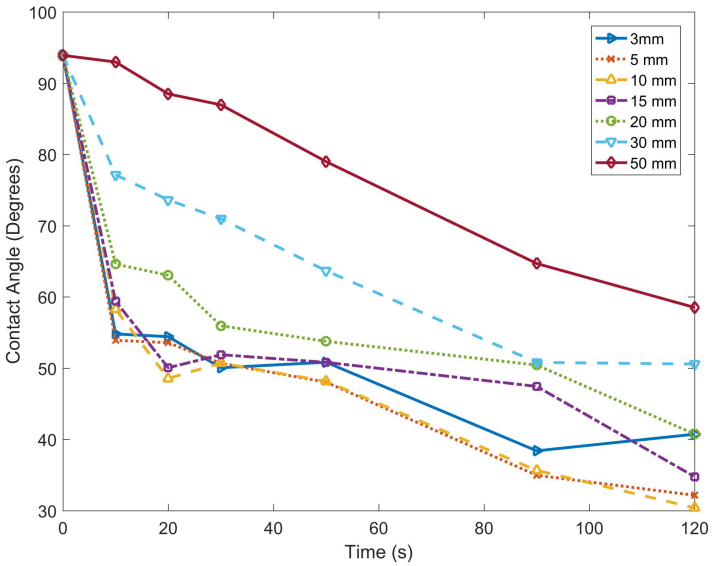

Figure 8.4: Contact angle changes with APPJ treatment time and distance. Errors are not included for clarity but are similar to those presented in previous figures

8.3.2 Surface energy

Using the aforementioned OWRK method it is possible to use contact angle measurements to calculate surface energy and split it into its two component parts. Taking contact angle measurements for the original 0.5 % O_2 admixture with diiodomethane showed a similar drop in contact angle with treatment time to that of water. However, when the OWRK method is used, the polar and dispersive elements of the surface energy of the PP are revealed. These results are shown in figure 8.5. There is a total increase in surface energy that matches the drop in contact angle previously shown in figure 8.2. The dispersive component appears invariant in time, with a value of around 30 mN/m, whereas the polar component shows an increase in energy from 10 mN/m to 55 mN/m after 30 seconds of treatment.

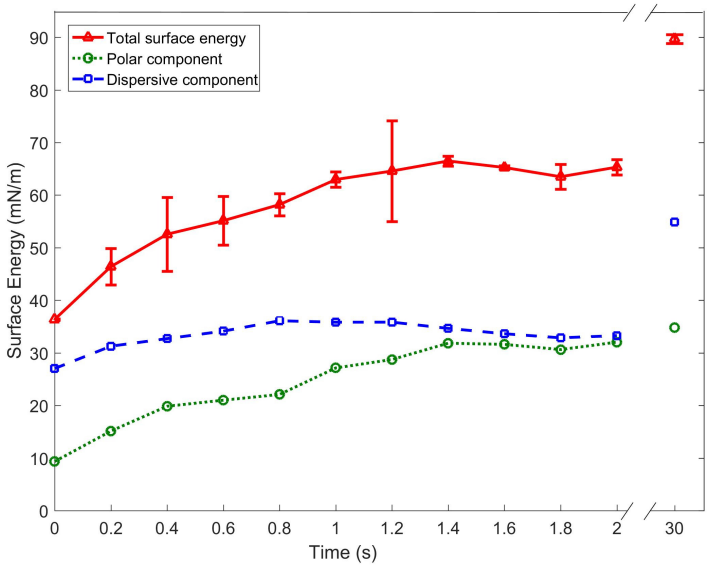

Figure 8.5: Surface energy of PP treated with an APPJ at 15 mm with 30 W_{net} power and 0.5 % O_2 admixture in the He feed gas. Errors are shown only for the total surface energy for clarity as they are propogated from original measurements

8.3.3 Surface analysis

The ATR-FTIR measurements of the surface showed an area of interest between wavenumbers 1500 and 1900 cm^{-1} shown in Figure 8.6. These could be absorption of water, however there is no corresponding peak in the data between 3000 and 4000 wavenumbers making this unlikely. Thus this area shows carbonyl stretching bands being formed on the surface of the PP. The increase in absorption with treatment time is due to a carbon oxygen double

bond (C = O), the details of which depend on the exact location of the dip [228]. The large dip on the 2 min treatment time at about 1720 cm^{-1}, that does not exist in the untreated spectrum, could be due to one of two possibilities. Either it is carboxylic acid (RC(=O)OH), or it is another similar ketone (an organic compound with a structure RC(=O)R') [229]. The dip around 1650 cm^{-1} can be attributed to conjugated ketones, which are similar to regular ketones apart from the alternating double and single bonds that allow for more freedom of movement of electrons. Another dip grows through treatment at 1670 cm^{-1} which is most likely an increase in the amide functional group. Amides can be produced from carboxylic acids, but do involve the inclusion of a nitrogen atom [230]. It is important to note, for comparison between this atmospheric method and low-pressure methods, that the increase in the amide functional group can only be achieved with the inclusion of nitrogen. This has only been possible in this work due to the nitrogen in the atmosphere.

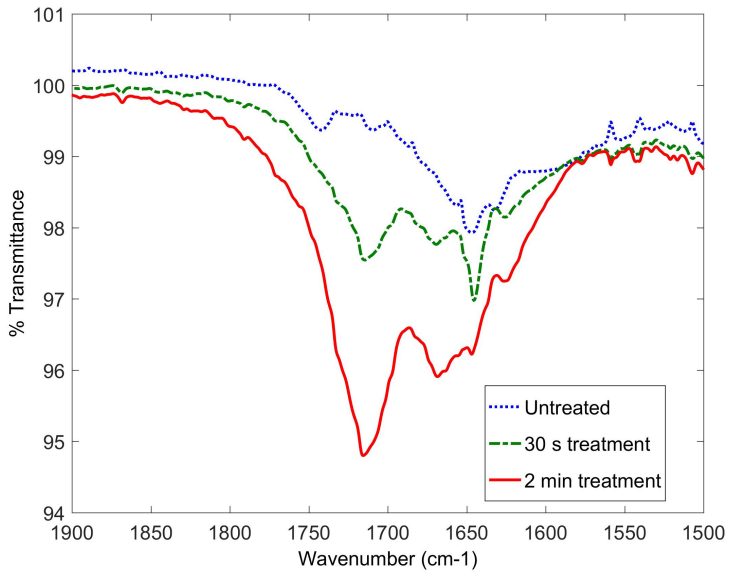

Figure 8.6: ATR-FTIR spectrum of PP before and after treatment at 15 mm, 0.5 % O_2 in the He feed gas, and an input power of 30 W_{net}

8.3.4 Surface modification pathways

From these measurements we attempt to obtain insight into the reaction pathways of the surface modification. The FTIR measurements show the well-known and well understood signs of oxidation of the PP, this suggests oxygen species from the plasma are dominant in observed modifications. However, the plasma chemistry of APPJs is well characterised and

there are several reactive oxygen species produced, e.g. atomic oxygen, singlet delta oxygen, and ozone. We performed TALIF experiments to measure the atomic oxygen densities at the exit of the APPJ as a function of oxygen admixture. The results in figure 8.7 show a strong correlation with the observed changes in contact angle. I.e. a maximum treatment effect at 0.5 % oxygen, when the concentration of O is maximum. The TALIF measurements agree with the O density measurements done by Knake [226]. Other reactive oxygen species have been measured in the same device. Sousa et al measured singlet delta oxygen [231], and Ellerweg et al ozone [232]. Singlet delta oxygen was shown to decrease with increasing oxygen admixture between 0.1 % and 0.7 %, and ozone was shown to increase over the same range. Furthermore, it is known that the density of atomic oxygen decreases exponentially with increased distance from the APPJ nozzle [225,226], whereas ozone is a long-lived radical species. All of this suggests a direct link between the production of atomic oxygen in the APPJ and the observed modification of the PP surface.

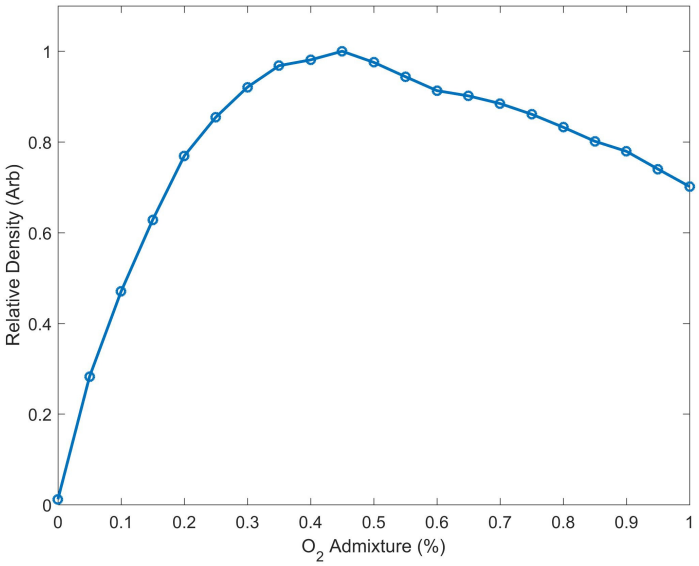

Figure 8.7: TALIF measurement of the relative densities of atomic oxygen in the effluent of the APPJ as a function of O_2 percentage in the input gas.

The results in figure 8.4 suggest that the observed fast change in contact angle is dependent on the number of reactive species at the PP surface, i.e. for large distances, the radical density is lower and therefore the observed effect is less. The slow change that is observed for all distances appears to depend on flux to the surface. The same change in contact angle can be achieved for larger distances (smaller radical concentrations) by increasing the treatment

time, resulting in similar fluxes. The pathways linked to the two observed surface processes can be explained with the FTIR measurements. The initial reaction shows production of carboxylic acid, or a similar ketone, and some conjugated ketones. The pathways of which are well understood [233]. This is a fast reaction that takes depends highly on the density of the atomic oxygen reaching the surface. The slow reaction is in part due to the inclusion of the nitrogen in the atmosphere which produces amides from the ketones created by the atomic oxygen. In addition ozone could also be involved within the slow reaction at the longer distances. It is clear that in both the fast and slow processes atomic oxygen from the APPJ plays a key role.

8.4 Conclusion

Using the radical-only effluent of an APPJ we were able to induce rapid and large increases in surface energy of PP films; a decrease in contact angle from 93.9° to 70.1° in 1.4 s and to 35° in 120 s, corresponding to an increase in surface energy from 36.4 mN/m to 66.5 mN/m in 1.4 s. These treatment effects are similar in scale to what is achieved with other devices, highlighting the importance of neutral radicals in plasma-induced PP modification. Further investigations using TALIF identify atomic oxygen as the dominant radical in these treatments. Unlike other radicals such as singlet delta oxygen and ozone, the measured O densities as a function of oxygen admixture match the observed changes in surface energy. Finally, FTIR surface analysis reveals a two stage mechanism for the production of polar bonds on the PP surface: A fast reaction producing carboxylic acid, or a similar ketone. Followed by a slower reaction which is likely to be a combination of ozone producing ketones, and nitrogen forming amides from the ketones.

Chapter 9

Conclusions and outlook

The work in this document focussed on the investigation of removal of deposits from first mirrors in a fusion device, such as ITER. The main investigation probed using the mirror as a powered electrode to form a CCP with a self bias that would attract energetic ions and sputter away the unwanted deposit. Prior to this some experimental work was conducted which was used alongside a simulation to predict trends for optimisation of the process. A Be plasma chemistry for the model was also developed to more-accurately vaticinate the conditions within ITER. In addition to this, work using an APPJ to modify polymer surfaces and investigate the mechanism has been shown.

HPEM, the model used in this work, was successfully benchmarked against published experimental work; slight variances in the results being consistent with the inclusion of the self bias that is integral to the operation of the deposition removal technique. The ion energies were shown to be controllable using the self bias which matched the experimental measurements taken within the laboratory at York; to within 10 %. The minor difference in results was shown to be due to the geometric differences in model and experiment causing a change in the grounded area to powered area ratio. This causes a change in bias required to balance the current in the reactor.

Al_2O_3, a proxy for the BeO deposits expected on ITER was etched experimentally at a rate of 0.18 nm/min at 24 mTorr with a 420 V bias. The deposit, post etching, was shown to be below the measurement threshold of the Filmetrics thin film analyser of 10 nm. Under the same conditions, at 60 mTorr the etching was found to be less successful, with significant redeposition in the centre of the mirror. This demonstrated the importance of considering redeposition when calculating etching rates. Using the SKM within HPEM to simulate these

conditions was attempted but was hampered by the use of Al_2O_3, the etching of which is poorly understood, and the simplicity of the model itself. Although good results were shown for simulating the plasma, the SKM did not give reasonable quantitative results for the surface. Comparing the modelled plasma and the experimental etching highlighted the link between the flux and energy of the ions to the surface. Also evident was the importance of the collision frequency of ions within the plasma, which needs to be minimal in order for the ions to achieve sufficient energy to etch; this is known to be optimum at lower pressures.

Moving towards ITER-relevant scenarios, the B-field chamber at Basel was modelled and briefly compared with results from the GEC reactor. Significant differences in the IEDF were noted for the geometry changes, including the shortening of the chamber to 1/3 of its original height, intended to be done experimentally in order to investigate varying magnetic fields. Geometry changes were further investigated using a simple mesh of varying volumes, although with constant powered electrode surface area. This increased the grounded area, but results for the self bias, which were expected to increase with powered to grounded ratio, showed minimal changes. This suggested that even the smallest geometry was already at maximum bias. The largest geometry gave interesting results with a complete disconnect between the electrode and the top and side walls of the reactor, instead limiting the electric field to the area immediately around the electrode, which could be considered a different geometry altogether. From this it is clear that geometrical differences are very important to consider with different energies and fluxes of ions for each change. Geometries for the first mirrors on ITER are already set, hence giving recommendations for size or shape is moot. Rather the only real recommendation can be that each individual geometry should be considered when optimising the system, which is possible, this is not an unsolvable problem. Not investigated in this work was the position of the ground in relation to the mirror and the consequences of this in relation to the IEDF and flux. This is something that can only be addressed on an individual case basis.

Voltage and frequency variations were also modelled in the smallest of the simple geometries. General trends showed that raising either resulted in an increase of ion flux to the surface. This was linked to a general increase in plasma density, but the location of the density increase is important. The flux rise with frequency was primarily in the centre of the electrode where the bulk plasma was most dense, however for the rise in voltage the edge effects became more prevalent, leaving the flux in the centre of the reactor more homogeneous.

Ultimately the homogeneity of the flux can be ignored, to an extent, if the ion energies are kept between the etching threshold of the BeO surface and the underlying mirror. Trends in the voltage and frequency changes suggested that 50 V at 60 MHz would be optimal in geometry 1. This was found to be impossible, with the plasma quenching within the simulation. The lowest voltage that sustained a plasma at 60 MHz was 75 V. The results from this did follow the trends but almost all the ions were above the Mo etching threshold of 35 eV. The frequency and voltage changes are therefore not independent and a plasma may not be sustainable at the values suggested by non-convolved trends. Again, these are issues that need to be addressed for each mirror individually, and it is possible that there is no perfect solution for every mirror. If generalisations must be made then the voltage and frequency changes are a trade off between etch homogeneity and etching rate. Increased flux of high energy ions through greater voltage or frequency will accelerate the etching, nevertheless the flux increases will always be higher in specific areas, which decreases the uniformity of the etch.

Even at low strengths magnetic fields were shown to be significant (in comparison to ITER). At the simulated strength of 100 G the flux profile change is dramatic, which is caused by large changes in the location of the bulk plasma density. The main bulk of the plasma shifts to the edge of the electrode where the edge effects create ions unable to travel easily across the magnetic field lines. It is known that at higher field strengths, within an order of magnitude of those that will be encountered on ITER, the plasma forms filamentary structures that are currently not well understood. In the B-field chamber at Basel a single filament formed that produced enhanced etching in that location and no etching anywhere else. It can therefore be concluded that these filaments will form if this deposition removal method is installed on ITER and that they will cause significant non-uniformity in the etching profile. Understanding these filaments is key in mitigating their effect, or even using them to improve the performance of the system. Further complications arise regarding the orientation of the fields in relation to the mirrors, but it seems prudent to attempt to understand the most basic case first.

Individual mirrors and their immediate environment clearly require individual solutions. This is unlikely to be achieved through an experimental campaign, as it is just not practical. General trends have been shown to not necessarily give achievable parameters for each specific case. Modelling these geometries is possible within HPEM, which has shown to give accurate

results for the plasma, leading to useful predictions regarding the etch of deposits. It is a far more reasonable endeavour to enhance the abilities of the SKM, form a working surface chemistry, and approach these individual problems in the form of simulations. This could be achieved within time frame that could give useful results for the implementation of this method prior to the predicted first plasma in ITER in 2025.

In an attempt to provide the tools, the Be plasma chemistry has been created, allowing the simulations to be closer to the working environment than when using the Al proxy. This chemistry set has shown differences between Al and Be within the plasma that are likely to have significant effects on the etching rates and results. The main difference has come from simple diffusion of the Be and Al, which has opened up the importance of the method of removing the sputtered material in order for it not to redeposit. With the Al being heavier it resides around the electrode and flows from the reactor with the outlet being nearby. However, it also ionises at a lower energy, resulting in nearly twice as much of it ionising and remaining in the bulk plasma in comparison to Be. Without a working surface model it isn't clear what effect the differences between the two will have on the surface interactions, but the differences in the plasma are significant enough to conclude that there will be some implications on the etching. With no experiments placing Al_2O_3 and BeO deposits in the same geometry it is impossible to currently conclude that experiments done with Al_2O_3 will accurately predict BeO etching.

Modelling should be the focus for further work in this area. Efforts should be made to create an accurate BeO surface chemistry for use within the SKM, which can be benchmarked against the limited experiments that have been carried out. Further experiments will be required in order to confirm the accuracy of the Be gas chemistry, which would prove useful in other areas of fusion research, where the plasma enters a lower state of ionisation and neutrals become important, such as in the divertor. The research being carried out on the effects of high-strength magnetic fields should be incorporated into the model, such that all variables could be accounted for, the goal being to investigate the individual mirror geometries and optimise the parameters on a case-by-case basis.

Although the APPJ was discarded as a possible deposition removal tool, the work carried out in the modification of polypropylene led to an understanding of the underlying mechanism and the importance of neutral radicals. Atomic oxygen is clearly responsible for the surface changes through a two-stage mechanism to create amides, which can only be possible with the inclusion of nitrogen from the atmosphere.

Appendix A

Pressures

Pressure (mTorr)	Pressure (Pa)
3.75	0.5
7.5	1
10	1.3
13	1.7
20	2.7
24	3.2
50	6.7
60	8
64	8.5
75	10
500	66.7

Table A.1: Pressures used in this work in mTorr and Pa.

Appendix B

Beryllium cross sections

The following data was provided by Dr Oleg Zatsirinney through private communication upon request in reference to his paper detailing the calculations [191].

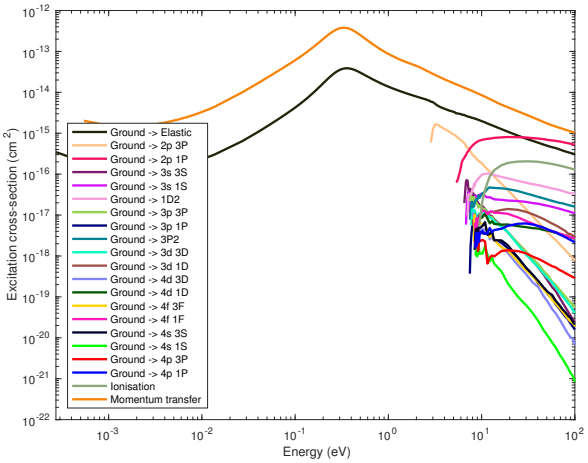

Figure B.1: Beryllium ground state excitation cross sections

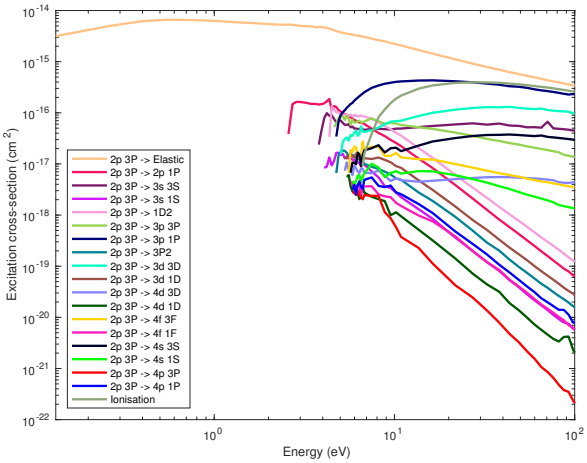

Figure B.2: Beryllium 2p 3P state excitation cross sections

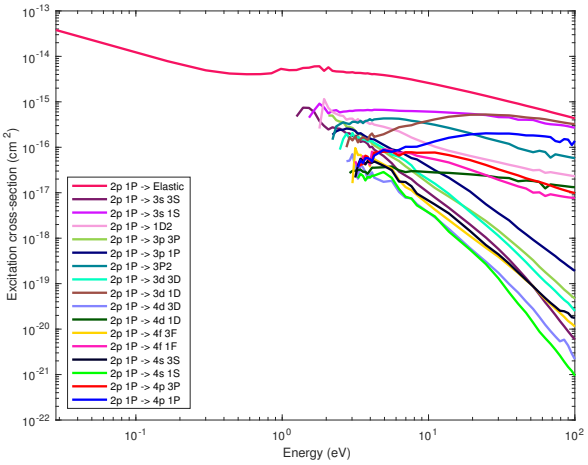

Figure B.3: Beryllium 2p 1P state excitation cross sections

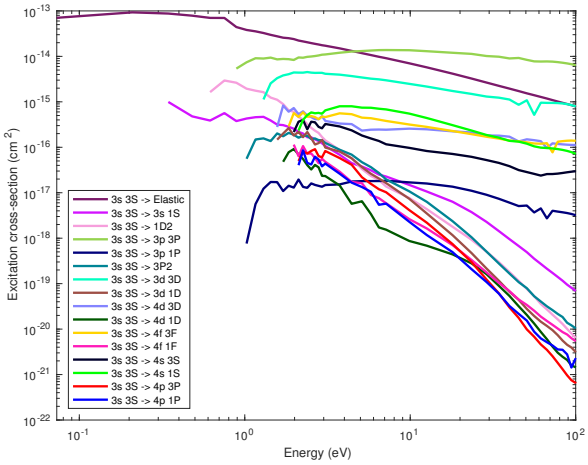

Figure B.4: Beryllium 3s 3S state excitation cross sections

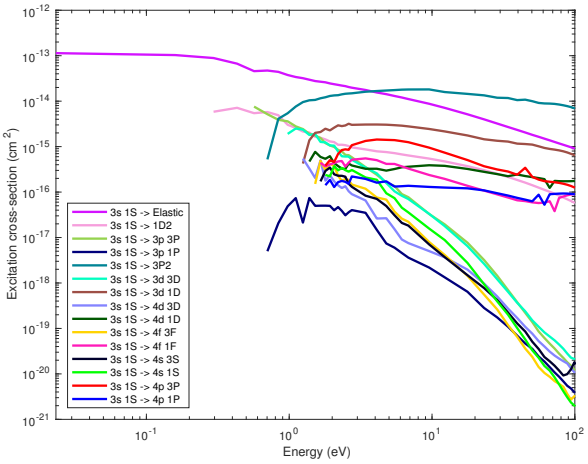

Figure B.5: Beryllium 3s 1S state excitation cross sections

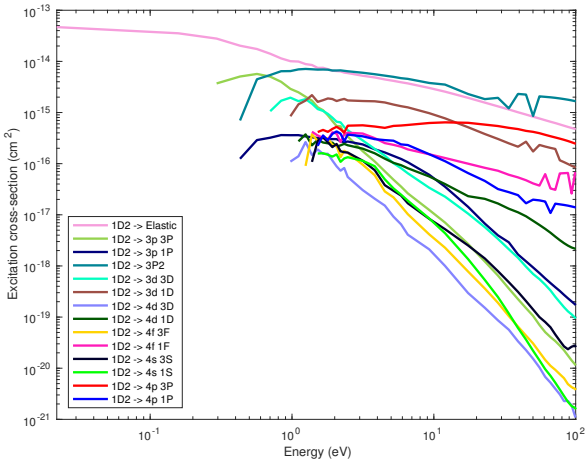

Figure B.6: Beryllium 1D2 state excitation cross sections

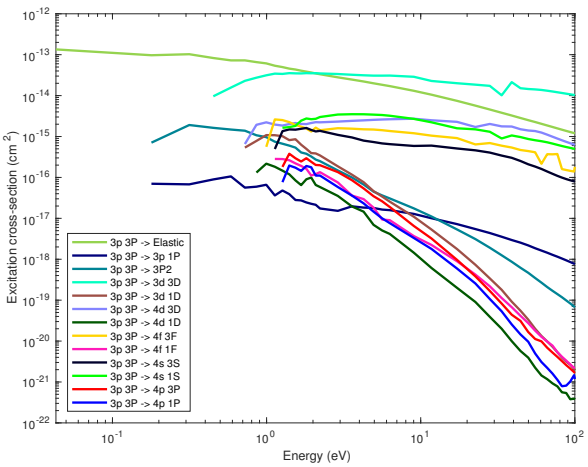

Figure B.7: Beryllium 3p 3P state excitation cross sections

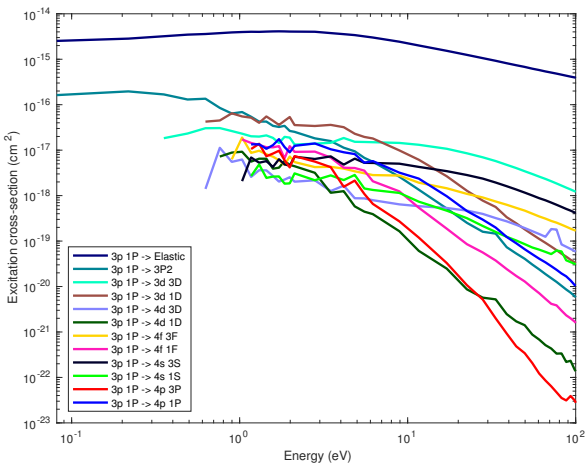

Figure B.8: Beryllium 3p 1P state excitation cross sections

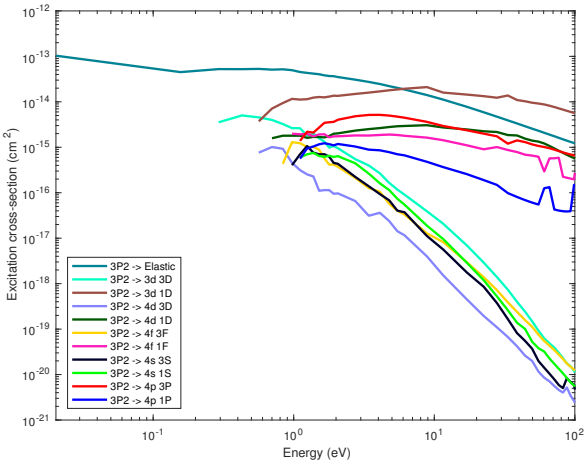

Figure B.9: Beryllium 3P2 state excitation cross sections

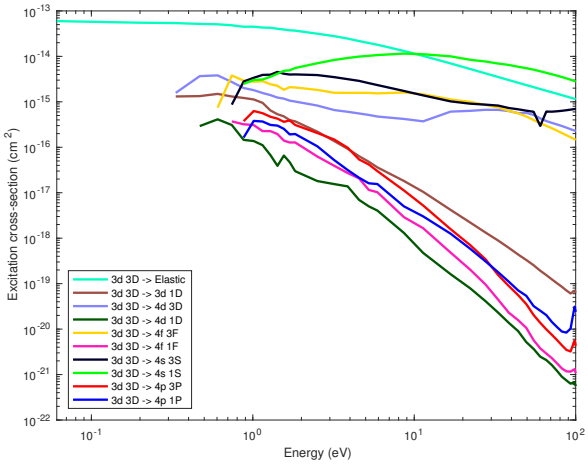

Figure B.10: Beryllium 3d 3D state excitation cross sections

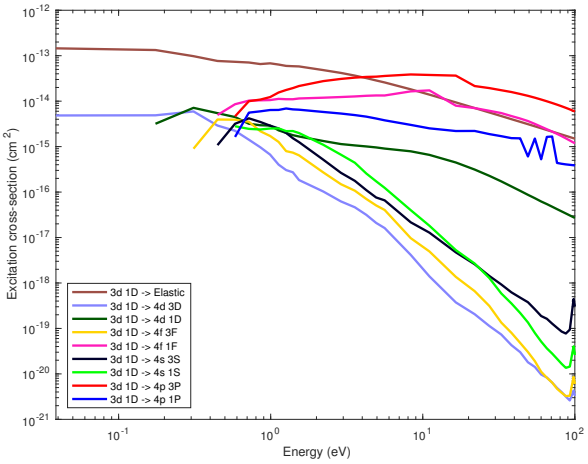

Figure B.11: Beryllium 3d 1D state excitation cross sections

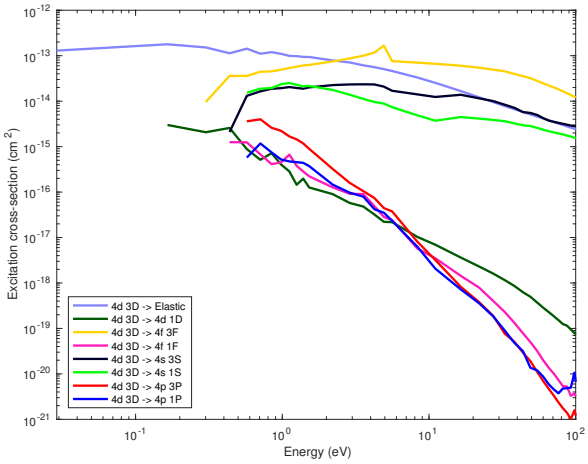

Figure B.12: Beryllium 4d 3D state excitation cross sections

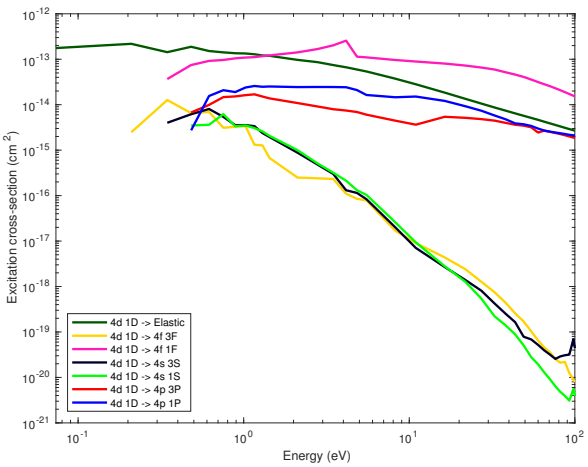

Figure B.13: Beryllium 4d 1D state excitation cross sections

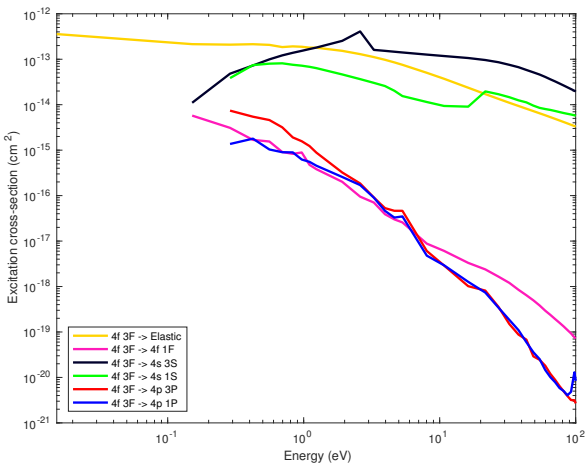

Figure B.14: Beryllium 4f 3F state excitation cross sections

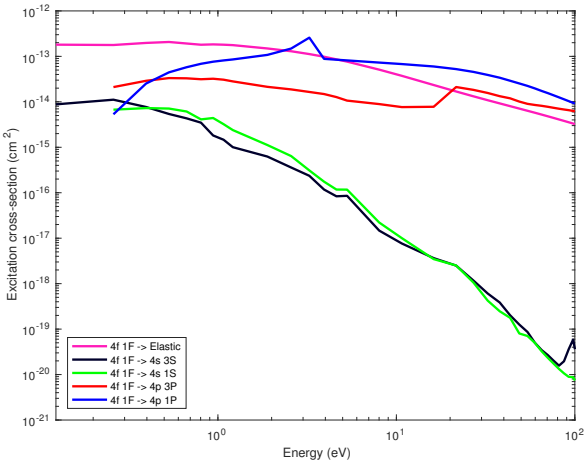

Figure B.15: Beryllium 4f 1F state excitation cross sections

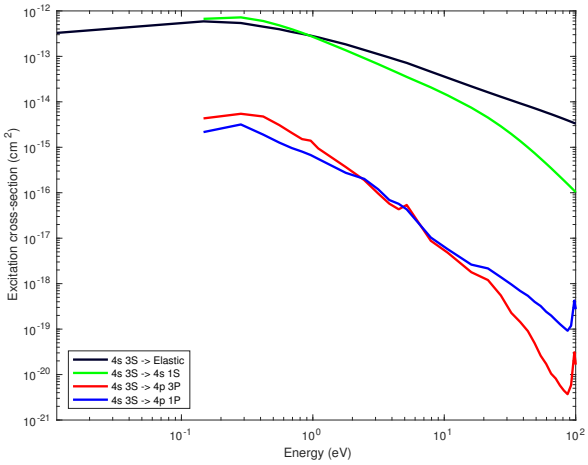

Figure B.16: Beryllium 4s 3S state excitation cross sections

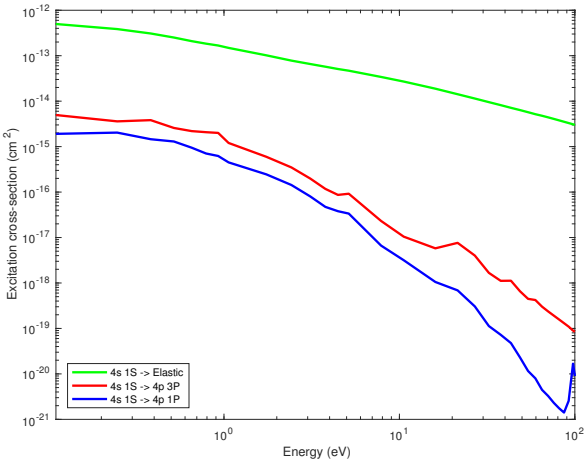

Figure B.17: Beryllium 4s 1S state excitation cross sections

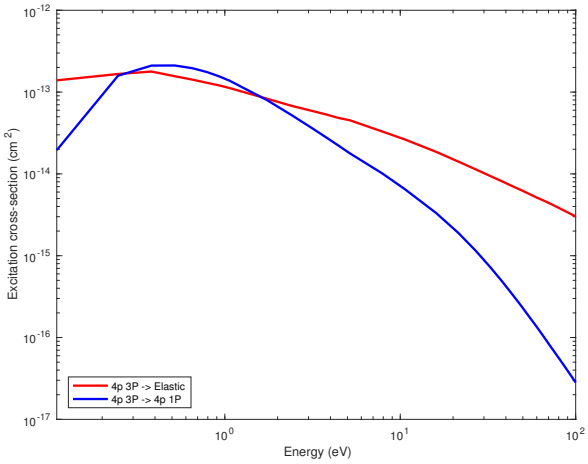

Figure B.18: Beryllium 4p 3P state excitation cross sections

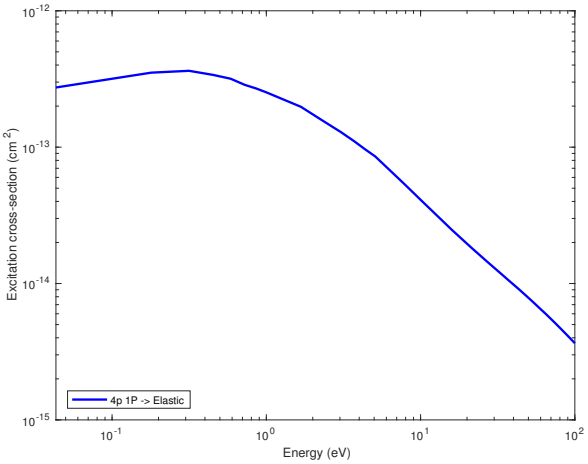

Figure B.19: Beryllium 4p 1P elastic cross section

Appendix C

List of publications and communications

Publications

- **D. Shaw**, A. Gibson, & E. Wagenaars, (2018). Low-temperature plasma removal of deposits from fusion first mirrors. *Proceedings 45th EPS*.
- **D. Shaw**, A. West, J. Bredin, & E. Wagenaars, (2016). Mechanisms behind surface modification of polypropylene film using an atmospheric-pressure plasma jet. *Plasma Sources Science and Technology*, 25(6), 065018. http://doi.org/10.1088/0963-0252/25/6/065018
- D. Shaw, P. M. Gyuk, A. West, M. Momoh, & **E. Wagenaars**, (2015). Surface modification of polymer films using an atmospheric-pressure plasma jet. *Proceedings 22nd ISPC*.

Oral presentations

- **D. Shaw**, A. Gibson, & E. Wagenaars, (2018). Low-temperature plasma removal of deposits from fusion first mirrors. *45th EPS* 2018
- **D. Shaw**, A. Gibson, M. Kushner, & E. Wagenaars, (2018). Modelling deposition removal from fusion first mirrors. *45th IOP Plasma Physics* 2018
- **D. Shaw**, A. Gibson, M. Kushner, & E. Wagenaars, (2017). Deposition removal from fusion first mirrors. *Culham Ph.D Showcase* 2017

- **D. Shaw**, A. Gibson, M. Kushner, & E. Wagenaars, (2017). Deposition removal from fusion optics. *Technological Plasma Workshop*
- **D. Shaw**, M. Kushner, & E. Wagenaars, (2017). Modelling deposition removal from fusion mirrors. *6th Workshop on Radio-frequency Plasmas*
- **D. Shaw**, A. Gibson, M. Kushner, & E. Wagenaars, (2017). Deposition removal from fusion optics. *IOP Early Career Researchers Meeting*
- **D. Shaw**, M. Kushner, & E. Wagenaars, (2016). Modelling deposition removal from fusion optics. *19th Workshop on the Exploration of Low-Temperature Plasma Physics*
- **D. Shaw**, A. West, & E. Wagenaars, (2015). Surface modification of polymer films using atmospheric-pressure plasma jet. *Technological Plasma Workshop*
- **D. Shaw**, A. West, & E. Wagenaars, (2015). Atmospheric-Pressure Plasma Jet Treatment for Polypropylene Surface Improvement. *18th Workshop on the Exploration of Low-Temperature Plasma Physics*

Poster presentations

- **D. Shaw**, P. M. Gyuk, & E. Wagenaars (2014). Surface Modification of Polymer Films Using an Atmospheric-Pressure Plasma Jet. *IOP Early Career Researchers Meeting*

Prizes

- IOP Ion and Plasma Surface Interactions Group Poster Prize (2014). *IOP Early Career Researchers Meeting*

List of References

[1] D. Shaw, A. West, J. Bredin, and E. Wagenaars. Mechanisms behind surface modification of polypropylene film using an atmospheric-pressure plasma jet. *Plasma Sources Science and Technology*, 25(6):065018, 2016.

[2] R. Aymar, P. Barabaschi, and Y. Shimomura. The ITER design. *Plasma Physics and Controlled Fusion*, 44(5):304, 2002.

[3] A. E. Costley, T. Sugie, G. Vayakis, and C. Walker. Technological challenges of ITER diagnostics. *Fusion Engineering and Design*, 74(1-4):109, 2005.

[4] M. D. Bock, et al. ITER perspective on fusion reactor diagnostics—A spectroscopic view. *Journal of Instrumentation*, 11(08):P08010, 2016.

[5] A. Donné, et al. Chapter 7: Diagnostics. *Nuclear Fusion*, 47(6):S337, 2007.

[6] V. Voitsenya, et al. Diagnostic first mirrors for burning plasma experiments (invited). *Review of Scientific Instruments*, 72(1 II):475, 2001.

[7] M. Rubel, G. D. Temmerman, P. Sundelin, J. P. Coad, a. Widdowson, D. Hole, F. L. Guern, M. Stamp, and J. Vince. An overview of a comprehensive First Mirror Test for ITER at JET. *Journal of Nuclear Materials*, 390-391(1):1066, 2009.

[8] ITER Physics Basis Editors, ITER Physics Expert Group Chairs and Co-Chairs, and ITER Joint Central Team and Physics Integration Unit. Chapter 1: Overview and summary. *Nuclear Fusion*, 39(12):2137, 2002.

[9] D. Ivanova, M. Rubel, a. Widdowson, P. Petersson, J. Likonen, L. Marot, E. Alves, a. Garcia-Carrasco, and G. Pintsuk. An overview of the comprehensive First Mirror Test in JET with ITER-like wall. *Physica Scripta*, T159:014011, 2014.

[10] D. Ivanova, a. Widdowson, J. Likonen, L. Marot, S. Koivuranta, J. P. Coad, M. Rubel, P. Petersson, and G. De Temmerman. Assessment of cleaning methods for first mirrors tested in JET for ITER. *Journal of Nuclear Materials*, 438(SUPPL):S1241, 2013.

[11] D. L. Rudakov, et al. First tests of molybdenum mirrors for ITER diagnostics in DIII-D divertor. *Review of Scientific Instruments*, 77(10), 2006.

[12] A. Litnovsky, et al. Progress in research and development of mirrors for ITER diagnostics. *Nuclear Fusion*, 49(7):075014, 2009.

[13] J. P. Coad, N. Bekris, J. D. Elder, S. K. Erents, D. E. Hole, K. D. Lawson, G. F. Matthews, R. D. Penzhorn, and P. C. Stangeby. Erosion/deposition issues at JET. *Journal of Nuclear Materials*, 290-293:224, 2001.

[14] J. Coad, J. Likonen, M. Rubel, E. Vainonen-Ahlgren, D. Hole, T. Sajavaara, T. Renvall, G. Matthews, and J. E. Contributors. Overview of material re-deposition and fuel retention studies at JET with the Gas Box divertor. *Nuclear Fusion*, 46(2):350, 2006.

[15] S. Brezinsek, et al. Residual carbon content in the initial ITER-Like Wall experiments at JET. *Journal of Nuclear Materials*, 438(SUPPL):S303, 2013.

[16] A. Widdowson, et al. Removal of beryllium-containing films deposited in JET from mirror surfaces by laser cleaning. *Journal of Nuclear Materials*, 415(1 SUPPL):S1199, 2011.

[17] L. Marot, C. Linsmeier, B. Eren, L. Moser, R. Steiner, and E. Meyer. Can aluminium or magnesium be a surrogate for beryllium: A critical investigation of their chemistry. *Fusion Engineering and Design*, 88(9-10):1718, 2013.

[18] L. Moser, L. Marot, B. Eren, R. Steiner, D. Mathys, F. Leipold, R. Reichle, and E. Meyer. Towards plasma cleaning of ITER first mirrors. *Nuclear Fusion*, 55(6):063020, 2015.

[19] L. Moser, R. Steiner, F. Leipold, R. Reichle, L. Marot, and E. Meyer. Plasma cleaning of ITER First Mirrors in magnetic field. *Journal of Nuclear Materials*, 463:940, 2015.

[20] L. Moser. *Plasma cleaning of diagnostic first mirrors for the nuclear fusion machine*. Ph.D. thesis, University of Basel, 2017.

[21] F. Leipold. RF Technique for FM Cleaning. Personal Communication, 2015.

[22] M. A. Lieberman and A. J. Lichtenberg. *Principles of Plasma Discharges and Materials Processing*. John Wiley & Sons, Inc., Hoboken, NJ, USA, 2005.

[23] F. F. Chen. *Introduction to Plasma Physics and Controlled Fusion*. Springer US, Boston, MA, 1984.

[24] V. M. Donnelly and A. Kornblit. Plasma etching: Yesterday, today, and tomorrow. *Journal of Vacuum Science & Technology A: Vacuum, Surfaces, and Films*, 31(5):050825, 2013.

[25] R. Behrisch and W. Eckstein, editors. *Sputtering by Particle Bombardment*, volume 110 of *Topics in Applied Physics*. Springer Berlin Heidelberg, Berlin, Heidelberg, 2007.

[26] T. C. Penn. Forecast of VLSI Processing—A Historical Review of the First Dry-Processed IC. *IEEE Transactions on Electron Devices*, 26(4):640, 1979.

[27] S. Irving. A plasma oxidation process for removing photoresist films. *Solid State Technology*, 14(6):47, 1971.

[28] A. Reinberg. Radial flow reactor, US Patent US3757733 A, 1973.

[29] N. Hosokawa, R. Matsuzaki, and T. Asamaki. RF Sputter-Etching by Fluoro-Chloro-Hydrocarbon Gases. *Japanese Journal of Applied Physics*, 13(S1):435, 1974.

[30] M. Lieberman. Analytical solution for capacitive RF sheath. *IEEE Transactions on Plasma Science*, 16(6):638, 1988.

[31] H. S. Butler and G. S. Kino. Plasma Sheath Formation by Radio-Frequency Fields. *Physics of Fluids*, 6(9):1346, 1963.

[32] J. T. Gudmundsson, E. Kawamura, and M. A. Lieberman. A benchmark study of a capacitively coupled oxygen discharge of the oopd1 particle-in-cell Monte Carlo code. *Plasma Sources Science and Technology*, 22(3):035011, 2013.

[33] K. Matyash, R. Schneider, F. Taccogna, A. Hatayama, S. Longo, M. Capitelli, D. Tskhakaya, and F. X. Bronold. Particle in cell simulation of low temperature laboratory plasmas. *Contributions to Plasma Physics*, 47(8-9):595, 2007.

[34] I. G. Kouznetsov, A. J. Lichtenberg, and M. A. Lieberman. Modelling electronegative discharges at low pressure. *Plasma Sources Science and Technology*, 5(4):662, 1996.

[35] M. M. Turner. Collisionless heating in radio-frequency discharges: a review. *Journal of Physics D: Applied Physics*, 42(19):194008, 2009.

[36] E. Kawamura, C. K. Birdsall, and V. Vahedi. Physical and numerical methods of speeding up particle codes and paralleling as applied to RF discharges. *Plasma Sources Science and Technology*, 9(3):413, 2000.

[37] P. Meyer and G. Wunner. Asynchronous cycling as a convergence acceleration method in particle simulation of direct current glow discharges. *Physics of Plasmas*, 4(9):3152, 1997.

[38] C. H. Shon, H. J. Lee, and J. K. Lee. Method to increase the simulation speed of particle-in-cell (PIC) code. *Computer Physics Communications*, 141(3):322, 2001.

[39] R. W. Hockney and J. W. Eastwood. *Computer Simulation Using Particles*. IOP Publishing, London, 1988.

[40] N. Hanzlikova. *Particle-In-Cell Simulations Of Highly Collisional Plasmas On The GPU In 1 And 2*. Ph.D. thesis, Dublin City University, 2015.

[41] J. Teunissen and U. Ebert. 3D PIC-MCC simulations of discharge inception around a sharp anode in nitrogen/oxygen mixtures. *Plasma Sources Science and Technology*, 25(4), 2016.

[42] S. H. Lee, F. Iza, and J. K. Lee. Particle-in-cell Monte Carlo and fluid simulations of argon-oxygen plasma: Comparisons with experiments and validations. In *Physics of Plasmas*, volume 13. 2006.

[43] J. Waskoenig, K. Niemi, N. Knake, L. M. Graham, S. Reuter, V. S.-v. der Gathen, and T. Gans. Atomic oxygen formation in a radio-frequency driven micro-atmospheric pressure plasma jet. *Plasma Sources Science and Technology*, 19(4):045018, 2010.

[44] E. Kawamura, A. J. Lichtenberg, and M. A. Lieberman. Electronegative plasma equilibria with spatially varying ionization. *Journal of Physics D: Applied Physics*, 45(49):495201, 2012.

[45] N. Nakano and T. Makabe. Influence of driving frequency on narrow-gap reactive-ion etching in SF 6. *Journal of Physics D: Applied Physics*, 28(1):31, 1995.

[46] Y. Sakiyama and D. B. Graves. Finite element analysis of an atmospheric pressure RF-excited plasma needle. *Journal of Physics D: Applied Physics*, 39(16):3451, 2006.

[47] J. Waskoenig, K. Niemi, N. Knake, L. M. Graham, S. Reuter, V. Schulz-von der Gathen, and T. Gans. Diagnostic-based modeling on a micro-scale atmospheric-pressure plasma jet. *Pure and Applied Chemistry*, 82(6):1209, 2010.

[48] M. J. Kushner. Hybrid modelling of low temperature plasmas for fundamental investigations and equipment design. *Journal of Physics D: Applied Physics*, 42(19):194013, 2009.

[49] M. J. Kushner. Modeling of magnetically enhanced capacitively coupled plasma sources: Ar discharges. *Journal of Applied Physics*, 94(3):1436, 2003.

[50] R. L. Kinder and M. J. Kushner. Wave propagation and power deposition in magnetically enhanced inductively coupled and helicon plasma sources. *Journal of Vacuum Science & Technology A: Vacuum, Surfaces, and Films*, 19(1):76, 2001.

[51] J. Lu and M. J. Kushner. Trench filling by ionized metal physical vapor deposition. *Journal of Vacuum Science & Technology A: Vacuum, Surfaces, and Films*, 19(5):2652, 2001.

[52] D. Zhang and M. J. Kushner. Investigations of surface reactions during C2F6 plasma etching of SiO2 with equipment and feature scale models. *Journal of Vacuum Science & Technology A: Vacuum, Surfaces, and Films*, 19(2):524, 2001.

[53] V. A. Godyak and R. B. Piejak. Abnormally low electron energy and heating-mode transition in a low-pressure argon rf discharge at 13.56 MHz. *Physical Review Letters*, 65(8):996, 1990.

[54] I. D. Kaganovich, V. I. Demidov, S. F. Adams, and Y. Raitses. Non-local collisionless and collisional electron transport in low-temperature plasma. *Plasma Physics and Controlled Fusion*, 51(12), 2009.

[55] R. J. Hoekstra and M. J. Kushner. Predictions of ion energy distributions and radical fluxes in radio frequency biased inductively coupled plasma etching reactors. *Journal of Applied Physics*, 79(5):2275, 1996.

[56] D. Zhang and M. J. Kushner. Surface kinetics and plasma equipment model for Si etching by fluorocarbon plasmas. *Journal of Applied Physics*, 87(3):1060, 2000.

[57] D. Zhang. *Surface reaction mechanisms in plasma etching processes.* Ph.D. thesis, 2000.

[58] A. Donné, et al. Chapter 7: Diagnostics. *Nuclear Fusion*, 47(6):S337, 2007.

[59] A. Razdobarin, et al. RF discharge for in situ mirror surface recovery in ITER. *Nuclear Fusion*, 55(9):093022, 2015.

[60] S. Huang, V. Volynets, J. R. Hamilton, S. Lee, I.-C. Song, S. Lu, J. Tennyson, and M. J. Kushner. Insights to scaling remote plasma sources sustained in NF 3 mixtures. *Journal of Vacuum Science & Technology A: Vacuum, Surfaces, and Films*, 35(3):031302, 2017.

[61] S. Huang, V. Volynets, J. R. Hamilton, S. K. Nam, I.-C. Song, S. Lu, J. Tennyson, and M. J. Kushner. Downstream etching of silicon nitride using continuous-wave and pulsed remote plasma sources sustained in Ar/NF3/O2 mixtures. *Journal of Vacuum Science & Technology A: Vacuum, Surfaces, and Films*, 36(2):021305, 2018.

[62] D. S. Stafford and M. J. Kushner. O2(1Δ) production in He/O2mixtures in flowing low pressure plasmas. *Journal of Applied Physics*, 96(5):2451, 2004.

[63] J. Lu and M. J. Kushner. Effect of sputter heating in ionized metal physical vapor deposition reactors. *Journal of Applied Physics*, 87(10):7198, 2000.

[64] M. Hayashi. Report No. IPPJ-AM-19. Technical report, Nagoya Institute of Technology, 1981.

[65] G. M. Petrov, J. L. Giuliani, and A. Dasgupta. Electron energy deposition in an electron-beam pumped KrF amplifier: Impact of beam power and energy. *Journal of Applied Physics*, 91(5):2662, 2002.

[66] D. Rapp and P. Englander-Golden. Total Cross Sections for Ionization and Attachment in Gases by Electron Impact. I. Positive Ionization. *The Journal of Chemical Physics*, 43(5):1464, 1965.

[67] A. Bogaerts, R. Gijbels, and J. Vlcek. Collisional-radiative model for an argon glow discharge. *Journal of Applied Physics*, 84(1):121, 1998.

[68] J. Vlcek. A collisional-radiative model applicable to argon discharges over a wide range of conditions. I. Formulation and basic data. *Journal of Physics D: Applied Physics*, 22(5):623, 1989.

[69] L. Vriens. Calculation of absolute ionisation cross sections of He, He*, He+, Ne, Ne*, Ne+, Ar, Ar*, Hg and Hg*. *Physics Letters*, 8(4):260, 1964.

[70] F. Kannari, M. Obara, and T. Fujioka. An advanced kinetic model of electron-beam-excited KrF lasers including the vibrational relaxation in KrF*(B) and collisional mixing of KrF*(B,C). *Journal of Applied Physics*, 57(9):4309, 1985.

[71] P. Lukáč, O. Mikuš, I. Morva, Z. Zábudlá, J. Trnovec, and M. Morvová. Electron and gas temperature dependences of the dissociative recombination coefficient of molecular ions Ar2+ with electrons. *Plasma Sources Science and Technology*, 20(5):055012, 2011.

[72] A. V. Phelps. Tabulations of collision cross sections and calculated transport and rection coefficients for electron collisions with O2. Technical report, University of Colorado, 1985.

[73] E. Krishnakumar and S. Srivastava. Cross-sections for electron impact ionization of O2. *International Journal of Mass Spectrometry and Ion Processes*, 113(1):1, 1992.

[74] M. Tashiro, K. Morokuma, and J. Tennyson. R-matrix calculation of electron collisions with electronically excited O2 molecules. *Physical Review A - Atomic, Molecular, and Optical Physics*, 73(5):1, 2006.

[75] P. D. Burrow. Dissociative attachment from the O2(a1Δg) state. *The Journal of Chemical Physics*, 59(9):4922, 1973.

[76] R. I. Hall and S. Trajmar. Scattering of 4.5 eV electrons by ground (X3Σg-) state and metastable (a1Δg) oxygen molecules. *Journal of Physics B: Atomic and Molecular Physics*, 8(12):L293, 1975.

[77] Y. Itikawa and A. Ichimura. Cross Sections for Collisions of Electrons and Photons with Atomic Oxygen. *Journal of Physical and Chemical Reference Data*, 19(3):637, 1990.

[78] R. R. Laher and F. R. Gilmore. Updated Excitation and Ionization Cross Sections for Electron Impact on Atomic Oxygen. *Journal of Physical and Chemical Reference Data*, 19(1):277, 1990.

[79] M. Gryziński. Classical theory of electronic and ionic inelastic collisions. *Physical Review*, 115(2):374, 1959.

[80] S. Matejcik and Others. Electron attachment to molecules and clusters of atmospheric relevence: oxygen and ozone. *Plasma Sources Sci. Technol.*, 6:140, 1997.

[81] H. Jacobs, F. Miethke, A. Rutscher, and H.-E. Wagner. Reaction Kinetics and Chemical Quasi-Equilibria of the Ozone Synthesis in Oxygen DC Discharges. *Contributions to Plasma Physics*, 36(4):471, 1996.

[82] B. Eliasson and U. Kogelschatz. *Basic data for modelling of electrical discharges in gases: oxygen.* ABB Asea Brown Boveri, Baden, 1986.

[83] M. Biondi. *Principles of laser plasmas.* Wiley, 1976.

[84] H. Deutsch, P. Scheier, K. Becker, and T. D. Märk. Calculated cross-sections for the electron-impact detachment from negative ions using the Deutsch-Märk (DM) formalism. *Chemical Physics Letters*, 382(1-2):26, 2003.

[85] E. Meeks, R. S. Larson, P. Ho, C. Apblett, S. M. Han, E. Edelberg, and E. S. Aydil. Modeling of SiO2 deposition in high density plasma reactors and comparisons of model predictions with experimental measurements. *Journal of Vacuum Science & Technology A: Vacuum, Surfaces, and Films*, 16(2):544, 1998.

[86] G. M. Lawrence and H. S. Liszt. Radiative lifetimes in the resonance series of Ne. *Physical Review*, 178(1):122, 1969.

[87] N. A. Dyatko, Y. Z. Ionikh, I. V. Kochetov, D. L. Marinov, A. V. Meshchanov, A. P. Napartovich, F. B. Petrov, and S. A. Starostin. Experimental and theoretical study of the transition between diffuse and contracted forms of the glow discharge in argon. *Journal of Physics D: Applied Physics*, 41(5), 2008.

[88] P. M. Becker and F. W. Lampe. Mass-spectrometric study of the bimolecular formation of diatomic argon ion. *Journal of Chemical Physics*, 42:3857, 1965.

[89] R. Atkinson, D. L. Baulch, R. A. Cox, R. F. Hampson, J. A. Kerr, M. J. Rossi, and J. Troe. Evaluated Kinetic, Photochemical and Heterogeneous Data for Atmospheric Chemistry: Supplement V. IUPAC Subcommittee on Gas Kinetic Data Evaluation for Atmospheric Chemistry. *Journal of Physical and Chemical Reference Data*, 26(3):521, 1997.

[90] R. Atkinson, D. L. Baulch, R. A. Cox, R. F. Hampson, J. A. Kerr, M. J. Rossi, and J. Troe. Evaluated Kinetic and Photochemical Data for Atmospheric Chemistry: Supplement VI. IUPAC Subcommittee on Gas Kinetic Data Evaluation for Atmospheric Chemistry. *Journal of Physical and Chemical Reference Data*, 26(6):1329, 1997.

[91] J. A. Kerr and S. J. Moss. *CRC Handbook of Bimolecular and Termolecular Gas Reactions*. CRC Press, Boca Raton, Folrida, 1981.

[92] M. Touzeau, G. Gousset, J. Jolly, D. Pagnon, M. Vialle, C. M. Ferreira, J. Loureiro, M. Pinheiro, and P. A. Sà. *Spectroscopy and Kinetics of an Oxygen Glow Discharge*. Springer US, 1990.

[93] B. F. Gordiets, C. M. Ferreira, V. L. Guerra, J. M. Loureiro, J. Nahorny, D. Pagnon, M. Touzeau, and M. Vialle. Kinetic Model of a Low-Pressure N2–O2 Flowing Glow Discharge. *IEEE Transactions on Plasma Science*, 23(4):750, 1995.

[94] J. T. Herron and D. S. Green. Chemical kinetics database and predictive schemes for nonthermal humid air plasma chemistry. Part II. Neutral species reactions. *Plasma Chemistry and Plasma Processing*, 21(3):459, 2001.

[95] A. V. Vasenkov, X. Li, G. S. Oehrlein, and M. J. Kushner. Properties of c-C4F8 inductively coupled plasmas. II. Plasma chemistry and reaction mechanism for modeling of Ar/c-C4F 8O2 discharges. *Journal of Vacuum Science & Technology A: Vacuum, Surfaces, and Films*, 22(3):511, 2004.

[96] E. Meeks. Modeling Chemical Downstream Etch Systems for NF3/O2 Mixtures. *Journal of The Electrochemical Society*, 144(1):357, 1997.

[97] S. W. Benson and A. E. Axworthy. Mechanism of the Gas Phase, Thermal Decomposition of Ozone. *The Journal of Chemical Physics*, 26(6):1718, 1957.

[98] W. Van Gaens and A. Bogaerts. Erratum: Kinetic modelling for an atmospheric pressure argon plasma jet in humid air (J. Phys. D: Appl. Phys. 46 (2013) 275201)). *Journal of Physics D: Applied Physics*, 47(7), 2014.

[99] F. Westley, J. T. Herron, and R. J. Cvetanovic. *Compilation of Chemical Kinetic Data for Combustion Chemistry (NSRDS-NBS 73, Parts 1 and 2)*. US Government Printing Office, Washington, 1987.

[100] V. N. Kondratiev. *Rate constants of gas phase reactions: Reference book*. Office of Standard Reference Data, National Bureau of Standards, U.S. Dept. of Commerce; distributed by National Technical Information Service, Washington, 1972.

[101] A. Mellouki, G. Poulet, and G. Le Bras. Upper limit of the rate constants for the reactions of N2O5 with OH, HO2 , Cl, and ClO at 293 K. *Journal of Geophysical Research*, 92(D4):4217, 1987.

[102] H. W. Ellis, R. Y. Pai, and E. W. McDaniel. Transport Properties of Gaseous Ions Over a Wide Energy Range. *Atomic Data and Nuclear Data Tables*, 17(3):177, 1976.

[103] P. Tian and M. J. Kushner. Controlling VUV photon fluxes in low-pressure inductively coupled plasmas. *Plasma Sources Science and Technology*, 24(3), 2015.

[104] Y. Ikezoe and A. Viggiano. *Gas phase ion-molecule reaction rate constants through 1986*. Ion Reaction Research Group of the Mass Spectrscopy Society of Japan, Tokyo, 1987.

[105] R. Johnsen, A. Chen, and M. A. Biondi. Three-body association reactions of He+, Ne+, and Ar+ ions in their parent gases from 78 to 300 K. *The Journal of Chemical Physics*, 73(4):1717, 1980.

[106] V. G. Anicich. Evaluated Bimolecular Ion-Molecule Gas Phase Kinetics of Positive Ions for Use in Modeling Planetary Atmospheres, Cometary Comae, and Interstellar Clouds. *Journal of Physical and Chemical Reference Data*, 22(6):1469, 1993.

[107] R. M. Snuggs, D. J. Volz, I. R. Gatland, J. H. Schummers, D. W. Martin, and E. W. McDaniel. Ion-Molecule Reactions between O- and O2 at Thermal Energies and Above. *Physical Review A*, 3(1):487, 1971.

[108] J. I. Steinfeld, S. M. Adler-Golden, and J. W. Gallagher. Critical Survey of Data on the Spectroscopy and Kinetics of Ozone in the Mesosphere and Thermosphere. *Journal of Physical and Chemical Reference Data*, 16(4):911, 1987.

[109] C. Lifshitz, R. L. C. Wu, T. O. Tiernan, and D. T. Terwilliger. Negative ion–molecule reactions of ozone and their implications on the thermochemistry of O3-. *The Journal of Chemical Physics*, 68(1):247, 1978.

[110] F. C. Fehsenfeld, D. L. Albritton, J. A. Burt, and H. I. Schiff. Associative-detachment reactions of O- and O2- by O2 ($1\Delta g$). *Canadian Journal of Chemistry*, 47(10):1793, 1969.

[111] A. P. Hickman. Approximate scaling formula for ion-ion mutual neutralization rates. *The Journal of Chemical Physics*, 70(11):4872, 1979.

[112] J. Moseley, R. Olson, and J. Peterson. Ion-ion mutual neutralization. *Case Studies in Atomic Physics*, 5(1):1, 1975.

[113] S. Norberg. *Modelling Atmospheric Pressure Plasma Jets: Plasma Dynamics, Interaction with Dielectric Surfaces, Liquid Layers and Cells*. Doctor of philosophy, University of Michigan, 2015.

[114] C. F. Abrams and D. B. Graves. Cu sputtering and deposition by off-normal, near-threshold Cu+ bombardment: molecular dynamics simulations. *Journal of Applied Physics*, 86(4):2263, 1999.

[115] R. Kelly. The surface binding energy in slow collisional sputtering. *Nuclear Inst. and Methods in Physics Research, B*, 18(1-6):388, 1986.

[116] J. Malherbe, S. Hofmann, and J. Sanz. Preferential sputtering of oxides: A comparison of model predictions with experimental data. *Applied Surface Science*, 27:355, 1986.

[117] T. Kubart, T. Nyberg, and S. Berg. Modelling of low energy ion sputtering from oxide surfaces. *Journal of Physics D: Applied Physics*, 43(20):205204, 2010.

[118] A. Sulyok, M. Menyhard, and J. B. Malherbe. Stability of ZnO{0 0 0 1} against low energy ion bombardment. *Surface Science*, 601(8):1857, 2007.

[119] J. Goschnick, J. Schuricht, a. Schweiker, and H. Ache. Sputter yields and erosion rates for low energy ion bombardment of multielemental powders. *Nuclear Instruments and Methods in Physics Research Section B: Beam Interactions with Materials and Atoms*, 83(3):339, 1993.

[120] Y. H. Lee, Z. H. Zhou, D. A. Danner, P. M. Fryer, and J. M. Harper. Chemical sputtering of Al2O3 by fluorine-containing plasmas excited by electron cyclotron resonance. *Journal of Applied Physics*, 68(10):5329, 1990.

[121] M. E. Day, M. Delfino, and S. Salimian. Low energy ion etching of aluminum oxide films and native aluminum oxide. *Journal of Applied Physics*, 72(11):5467, 1992.

[122] Y. Yamamura and H. Tawara. Energy dependence of ion-induced sputtering yields from monatomic solids at normal incidence. *Atomic Data and Nuclear Data Tables*, 62(2):149, 1996.

[123] N. Laegreid and G. K. Wehner. Sputtering yields of metals for ar+ and ne+ ions with energies from 50 to 600 ev. *Journal of Applied Physics*, 32(3):365, 1961.

[124] C. Steinbrüchel. On the sputtering yield of molecular ions. *Journal of Vacuum Science & Technology A: Vacuum, Surfaces, and Films*, 3(5):1913, 1985.

[125] T. Tondu, J.-p. Chardon, and S. Zurbach. Sputtering yield of potential ceramics for Hall Effect. *Iepc*, pages 1–7, 2011.

[126] W. H. Hayward and A. R. Wolter. Sputtering Yield Measurements with Low-Energy Metal Ion Beams. *Journal of Applied Physics*, 40(7):2911, 1969.

[127] T. Kubart, O. Kappertz, T. Nyberg, and S. Berg. Dynamic behaviour of the reactive sputtering process. *Thin Solid Films*, 515(2 SPEC. ISS.):421, 2006.

[128] W. P. Leroy, S. Mahieu, R. Persoons, and D. Depla. Method to Determine the Sticking Coefficient of O2 on Deposited Al During Reactive Magnetron Sputtering, Using Mass Spectrometry. *Plasma Processes and Polymers*, 6:S342, 2009.

[129] W. P. Leroy, S. Mahieu, R. Persoons, and D. Depla. Quantification of the incorporation coefficient of a reactive gas on a metallic film during magnetron sputtering: The method and results. *Thin Solid Films*, 518(5):1527, 2009.

[130] A. Bogaerts, E. Wagner, B. Smith, J. Winefordner, D. Pollmann, W. Harrison, and R. Gijbels. Three-dimensional density profiles of sputtered atoms and ions in a direct current glow discharge: experimental study and comparison with calculations. *Spectrochimica Acta Part B: Atomic Spectroscopy*, 52(2):205, 1997.

[131] J. K. Olthoff and K. E. Greenberg. The Gaseous Electronics Conference RF Reference Cell—An Introduction. *Journal of Research of the National Institute of Standards and Technology*, 100(4):327, 1995.

[132] A. K. Rossall, J. A. van den Berg, D. Meehan, S. Rajendiran, and E. Wagenaars. Analysis of plasma enhanced pulsed laser deposition of transition metal oxide thin films using medium energy ion scattering. *Nuclear Instruments and Methods in Physics Research Section B: Beam Interactions with Materials and Atoms*, (May), 2018.

[133] S. Rajendiran. *Plasma enhanced pulsed laser deposition.* Ph.D. thesis, University of York, 2017.

[134] A. M. Howatson. *An Introduction to Gas Discharges.* Elsevier, 1965.

[135] A. Maffini, L. Moser, L. Marot, D. Dellasega, A. Uccello, and M. Passoni. Cleaning of ITER-like First Mirrors : an experimental comparison between plasma and laser cleaning techniques. 52(2012):63020, 2015.

[136] A. Maffini, A. Uccello, D. Dellasega, and M. Passoni. Laser cleaning of diagnostic mirrors from tungsten-oxygen tokamak-like contaminants. *Nuclear Fusion*, 56(8), 2016.

[137] V. Schulz-Von Der Gathen, V. Buck, T. Gans, N. Knake, K. Niemi, S. Reuter, L. Schaper, and J. Winter. Optical diagnostics of micro discharge jets. *Contributions to Plasma Physics*, 47(7):510, 2007.

[138] V. Schulz-von der Gathen, L. Schaper, N. Knake, S. Reuter, K. Niemi, T. Gans, and J. Winter. Spatially resolved diagnostics on a microscale atmospheric pressure plasma jet. *Journal of Physics D: Applied Physics*, 41(19):194004, 2008.

[139] J. Winter, R. Brandenburg, and K.-D. Weltmann. Atmospheric pressure plasma jets: an overview of devices and new directions. *Plasma Sources Science and Technology*, 24(6):064001, 2015.

[140] J. Reece Roth. *Industrial Plasma Engineering*. Taylor & Francis, 2001.

[141] M. Chichina, Z. Hubicka, O. Churpita, and M. Tichy. Measurement of the parameters of atmospheric-pressure barrier-torch discharge. *Plasma Processes and Polymers*, 2(6):501, 2005.

[142] X. P. Lu, Q. Xiong, Z. Y. Tang, Z. H. Jiang, and Y. Pan. A cold plasma jet device with multiple plasma plumes merged. *IEEE Transactions on Plasma Science*, 36(4 PART 1):990, 2008.

[143] Q. Y. Nie, Z. Cao, C. S. Ren, D. Z. Wang, and M. G. Kong. A two-dimensional cold atmospheric plasma jet array for uniform treatment of large-area surfaces for plasma medicine. *New Journal of Physics*, 11, 2009.

[144] Z. Cao, J. L. Walsh, and M. G. Kong. Atmospheric plasma jet array in parallel electric and gas flow fields for three-dimensional surface treatment. *Applied Physics Letters*, 94(2):021501, 2009.

[145] Z. Cao, Q. Nie, D. L. Bayliss, J. L. Walsh, C. S. Ren, D. Z. Wang, and M. G. Kong. Spatially extended atmospheric plasma arrays. *Plasma Sources Science and Technology*, 19(2):025003, 2010.

[146] X. Pei, Z. Wang, Q. Huang, S. Wu, and X. Lu. Dynamics of a plasma jet array. *IEEE Transactions on Plasma Science*, 39(11 PART 1):2276, 2011.

[147] Q. Q. Fan, M. Y. Qian, C. S. Ren, D. Wang, and X. Wen. Discharge characteristics of a cold-atmospheric-plasma jet array generated with single-electrode configuration. *IEEE Transactions on Plasma Science*, 40(6 PART 2):1724, 2012.

[148] X. Zhang, D. Liu, H. Wang, L. Liu, S. Wang, and S. Z. Yang. Highly effective inactivation of Pseudomonas sp HB1 in water by atmospheric pressure microplasma jet array. *Plasma Chemistry and Plasma Processing*, 32(5):949, 2012.

[149] S. Liao, N. Gopalsami, E. R. Koehl, T. W. Elmer, A. Heifetz, H. T. Chien, and A. C. Raptis. Nuclear radiation-induced atmospheric air breakdown in a spark gap. *IEEE Transactions on Plasma Science*, 40(4):990, 2012.

[150] S. O. Kim, J. Y. Kim, D. Y. Kim, and J. Ballato. Intense plasma emission induced by jet-to-jet coupling in atmospheric pressure plasma arrays. *Applied Physics Letters*, 101(17), 2012.

[151] J.-C. Wang, N. Leoni, H. Birecki, O. Gila, and M. J. Kushner. Characteristics of a radio-frequency micro-dielectric barrier discharge array. *Plasma Sources Science and Technology*, 22(2):025015, 2013.

[152] M. Ghasemi, P. Olszewski, J. W. Bradley, and J. L. Walsh. Interaction of multiple plasma plumes in an atmospheric pressure plasma jet array. *Journal of Physics D: Applied Physics*, 46(5):052001, 2013.

[153] C. Qian, Z. Fang, J. Yang, and M. Kang. Investigation on atmospheric pressure plasma jet array in ar. *IEEE Transactions on Plasma Science*, 42(10):2438, 2014.

[154] C. Zhang, T. Shao, Y. Zhou, Z. Fang, P. Yan, and W. Yang. Effect of O2 additive on spatial uniformity of atmospheric-pressure helium plasma jet array driven by microsecond-duration pulses. *Applied Physics Letters*, 105(4):2, 2014.

[155] M. Thomas and K. Mittal, editors. *Atmospheric Pressure Plasma Treatment of Polymers*. John Wiley & Sons, Inc., Hoboken, NJ, USA, 2013.

[156] R. A. Wolf. *Atmospheric Pressure Plasma for Surface Modification*. John Wiley & Sons, Inc., Hoboken, NJ, USA, 2012.

[157] S. Kubinova, K. Zaviskova, L. Uherkova, V. Zablotskii, O. Churpita, O. Lunov, and A. Dejneka. Non-thermal air plasma promotes the healing of acute skin wounds in rats. *Scientific Reports*, 7:45183, 2017.

[158] B. Haertel, T. von Woedtke, K.-D. Weltmann, and U. Lindequist. Non-Thermal Atmospheric-Pressure Plasma Possible Application in Wound Healing. *Biomolecules & Therapeutics*, 22(6):477, 2014.

[159] S. Bekeschus, A. Schmidt, K.-D. Weltmann, and T. von Woedtke. The plasma jet kINPen – A powerful tool for wound healing. *Clinical Plasma Medicine*, 4(1):19, 2016.

[160] A. M. Hirst, F. M. Frame, N. J. Maitland, and D. O'Connell. Low Temperature Plasma: A Novel Focal Therapy for Localized Prostate Cancer? *BioMed Research International*, 2014:1, 2014.

[161] A. M. Hirst, F. M. Frame, M. Arya, N. J. Maitland, and D. O'Connell. Low temperature plasmas as emerging cancer therapeutics: the state of play and thoughts for the future. *Tumor Biology*, 37(6):7021, 2016.

[162] A. R. Gibson, H. O. McCarthy, A. A. Ali, D. O'Connell, and W. G. Graham. Interactions of a non-thermal atmospheric pressure plasma effluent with PC-3 prostate cancer cells. *Plasma Processes and Polymers*, 11(12):1142, 2014.

[163] D. O'Connell, L. J. Cox, W. B. Hyland, S. J. McMahon, S. Reuter, W. G. Graham, T. Gans, and F. J. Currell. Cold atmospheric pressure plasma jet interactions with plasmid DNA. *Applied Physics Letters*, 98(4):98, 2011.

[164] W. A. Davis. *Radio Frequency Circuit Design.* John Wiley & Sons, Inc., Hoboken, NJ, USA, 2010.

[165] J. Waskoenig. *Numerical simulations of the electron dynamics in single and duel radio-frequency driven atmospheric plasmas and associated plasma chemistry in electronegative He-O2 mixtures.* Ph.D. thesis, Queen's University Belfast, 2011.

[166] J. Golda, et al. Concepts and characteristics of the 'COST Reference Microplasma Jet'. *Journal of Physics D: Applied Physics*, 49(8):084003, 2016.

[167] R. Massarczyk, P. Chu, C. Dugger, S. Elliott, K. Rielage, and W. Xu. Paschen's law studies in cold gases. *Journal of Instrumentation*, 12(06):P06019, 2017.

[168] M. S. Naidu and V. Kamaraju. *High Voltage Engineering.* Tata McGraw-Hill Education, 2nd edition, 1995.

[169] F. Paschen. Ueber die zum Funkenübergang in Luft, Wasserstoff und Kohlensäure bei verschiedenen Drucken erforderliche Potentialdifferenz. *Annalen der Physik*, 273(5):69, 1889.

[170] R. V. Stuart and G. K. Wehner. Sputtering Yields at Very Low Bombarding Ion Energies. *Journal of Applied Physics*, 33(7):2345, 1962.

[171] J. Liu, G. L. Huppert, and H. H. Sawin. Ion bombardment in rf plasmas. *Journal of Applied Physics*, 68(8):3916, 1990.

[172] A. Maffini, L. Moser, L. Marot, R. Steiner, D. Dellasega, A. Uccello, E. Meyer, and M. Passoni. In situ cleaning of diagnostic first mirrors : an experimental comparison between plasma and laser cleaning in ITER-relevant conditions. *Nuclear Fusion*, 046014, 2016.

[173] F. Leipold, et al. Cleaning of first mirrors in ITER by means of radio frequency discharges. *Review of Scientific Instruments*, 87(11):11D439, 2016.

[174] E. Kawamura, V. Vahedi, M. A. Lieberman, and C. K. Birdsall. Ion energy distributions in rf sheaths ; review , analysis and simulation. *Plasma Sources Science and Technology*, 45, 1999.

[175] E. B. Macak, W. D. Münz, and J. M. Rodenburg. Plasma-surface interaction at sharp edges and corners during ion-assisted physical vapor deposition. Part II: Enhancement of the edge-related effects at sharp corners. *Journal of Applied Physics*, 94(5):2837, 2003.

[176] L. Stafford, J. Margot, S. Delprat, M. Chaker, and S. J. Pearton. Influence of redeposition on the plasma etching dynamics. *Journal of Applied Physics*, 101(8), 2007.

[177] S. Delprat, M. Chaker, and J. Margot. Investigation of the gas pressure influence on patterned platinum etching characteristics using a high-density plasma. *Journal of Applied Physics*, 89(1):29, 2001.

[178] C. M. Horwitz. Radio-frequency Ar sputter etch rates: Theory and experiment. *Journal of Vacuum Science & Technology B: Microelectronics and Nanometer Structures*, 11(5):1895, 1993.

[179] C. Y. Chang, J. P. McVittie, K. C. Saraswat, and K. K. Lin. Backscattered deposition in Ar sputter etch of silicon dioxide. *Applied Physics Letters*, 63(16):2294, 1993.

[180] J. Bodhansky, J. Roth, and F. Brossa. Formation of various coatings and their behaviour under particle bombardment. *Journal of Nuclear Materials*, 85-86:1145, 1979.

[181] L. Moser, et al. Investigation and plasma cleaning of first mirrors coated with relevant ITER contaminants: beryllium and tungsten. *Nuclear Fusion*, 57(8):086019, 2017.

[182] M. Surendra and D. B. Graves. Capacitively coupled glow discharges at frequencies above 13.56 MHz. *Applied Physics Letters*, 59(17):2091, 1991.

[183] R. D. Kolasinski, J. E. Polk, D. Goebel, and L. K. Johnson. Sputtering yield measurements at glancing incidence using a quartz crystal microbalance. *Journal of Vacuum Science & Technology A: Vacuum, Surfaces, and Films*, 25(2):236, 2007.

[184] M. Schwabe, U. Konopka, P. Bandyopadhyay, and G. E. Morfill. Pattern formation in a complex plasma in high magnetic fields. *Physical Review Letters*, 106(21):2, 2011.

[185] U. Konopka. Complex Plasmas in Strong Magnetic Field Environments. In *AIP Conference Proceedings*, volume 799, pages 181–184. AIP, 2005.

[186] E. Thomas, U. Konopka, R. L. Merlino, and M. Rosenberg. Initial measurements of two- and three-dimensional ordering, waves, and plasma filamentation in the Magnetized Dusty Plasma Experiment. *Physics of Plasmas*, 23(5), 2016.

[187] K. A. Berrington and R. E. H. Clark. Recommended data for electron impact excitation of Be+ and B+ ions. *Nuclear Fusion (Suppl.)*, 3:87, 1992.

[188] K. Bartschat, P. Burke, and M. Scott. Electron impact excitation of beryllium. *Journal of Physics B: Atomic, Molecular and Optical Physics*, 29(20), 1996.

[189] C. Ballance, D. Griffin, J. Colgan, S. Loch, and M. Pindzola. Electron-impact excitation of beryllium and its ions. *Physical Review A - Atomic, Molecular, and Optical Physics*, 68(6):062705/1, 2003.

[190] R. Clark and J. Abdallah. Electron impact excitation cross sections for beryllium and boron. *Physica Scripta*, T62:7, 1996.

[191] O. Zatsarinny, K. Bartschat, D. V. Fursa, and I. Bray. Calculations for electron-impact excitation and ionization of beryllium. *Journal of Physics B: Atomic, Molecular and Optical Physics*, 49(23):1, 2016.

[192] T. Maihom, I. Sukuba, R. Janev, K. Becker, T. Märk, A. Kaiser, J. Limtrakul, J. Urban, P. Mach, and M. Probst. Electron impact ionization cross sections of beryllium and beryllium hydrides. *The European Physical Journal D*, 67(1):2, 2013.

[193] J. R. Fuhr and W. L. Wiese. Tables of atomic transition probabilities for Beryllium and Boron. *Journal of Physical and Chemical Reference Data*, 39(1):1, 2010.

[194] M. Gryziński. Classical theory of atomic collisions. I. Theory of Inelestic collisions. *Physical Review*, 138(2):336, 1965.

[195] M. Gryziński. Two-particle collisions. II. Coulomb collisions in the laboratory system of coordinates. *Physical Review*, 138(2A), 1965.

[196] M. Gryziński. Two-particle collisions. I. General relations for collisions in the laboratory system. *Physical Review*, 138(2A), 1965.

[197] E. Bauer and C. D. Bartky. Calculation of inelastic electron-molecule collision cross sections by classical methods. *The Journal of Chemical Physics*, 43(7):2466, 1965.

[198] B. Moiseiwitsch and S. Smith. Electron impact excitation of atoms. *Review of Modern Physics*, 40(2):238, 1968.

[199] J. A. Manion, et al. NIST Chemical Kinetics Database.

[200] Quantemol. Quantemol DB.

[201] P. Politzer, P. Jin, and J. S. Murray. Atomic polarizability, volume and ionization energy. *Journal of Chemical Physics*, 117(18):8197, 2002.

[202] B. R. Eichelberger, T. P. Snow, and V. M. Bierbaum. Collision rate constants for polarizable ions. *Journal of the American Society for Mass Spectrometry*, 14(5):501, 2003.

[203] H. Hotop and a. Niehaus. Reactions of excited atoms and molecules with atoms and molecules. *International Journal of Mass Spectrometry and Ion Physics*, 5:415, 1970.

[204] K. A. Temelkov, N. K. Vuchkov, R. P. Ekov, and N. V. Sabotinov. Determination of characteristic constants for some basic processes in plasma-diffusion, Penning ionization, asymmetric charge transfer. *Journal of Physics D: Applied Physics*, 41(10), 2008.

[205] J. F. Friedrich, L. Wigant, W. Unger, A. Lippitz, H. Wittrich, D. Prescher, J. Erdmann, H. V. Gorsler, and L. Nick. Barrier properties of plasma-modified polypropylene and

polyethyleneterephthalate. *Journal of Adhesion Science and Technology*, 9(9):1165, 1995.

[206] C.-m. Chan. *Polymer Surface Modification and Characterization.* Carl Hanser, GmbH and Co., New York, 1994.

[207] A. Kuzminova, M. Vandrovcová, A. Shelemin, O. Kylián, A. Choukourov, J. Hanuš, L. Bačáková, D. Slavínská, and H. Biederman. Treatment of poly(ethylene terephthalate) foils by atmospheric pressure air dielectric barrier discharge and its influence on cell growth. *Applied Surface Science*, 357:689, 2015.

[208] A. Salimi. Characterization of nano scale adhesion at solid surface of oxidized PP wax/PP blends. *International Journal of Adhesion and Adhesives*, 33:61, 2012.

[209] C. Muhlhan, S. Weidner, J. Friedrich, and H. Nowack. Improvement of bonding properties of polypropylene by low- pressure plasma treatment. *Surface and Coatings Technology*, 119:783, 1999.

[210] D. Hegemann, H. Brunner, and C. Oehr. Plasma treatment of polymers for surface and adhesion improvement. *Nuclear Instruments and Methods in Physics Research Section B: Beam Interactions with Materials and Atoms*, 208:281, 2003.

[211] N. Shahidzadeh-Ahmadi, M. Chehimi, F. Arefi-Khonsari, N. Foulon-Belkacemi, J. Amouroux, and M. Delamar. A physicochemical study of oxygen plasma-modified polypropylene. *Colloids and Surfaces A: Physicochemical and Engineering Aspects*, 105(2-3):277, 1995.

[212] K. N. Pandiyaraj, V. Selvarajan, R. Deshmukh, and C. Gao. Modification of surface properties of polypropylene (PP) film using DC glow discharge air plasma. *Applied Surface Science*, 255(7):3965, 2009.

[213] K. G. Kostov, T. M. C. Nishime, L. R. O. Hein, and a. Toth. Study of polypropylene surface modification by air dielectric barrier discharge operated at two different frequencies. *Surface and Coatings Technology*, 234:60, 2013.

[214] N. De Geyter, R. Morent, C. Leys, L. Gengembre, and E. Payen. Treatment of polymer films with a dielectric barrier discharge in air, helium and argon at medium pressure. *Surface and Coatings Technology*, 201(16-17):7066, 2007.

[215] F. Massines and G. Gouda. A comparison of polypropylene-surface treatment by filamentary, homogeneous and glow discharges in helium at atmospheric pressure. *Journal of Physics D: Applied Physics*, 31:3411, 1999.

[216] N.-Y. Cui and N. M. Brown. Modification of the surface properties of a polypropylene (PP) film using an air dielectric barrier discharge plasma. *Applied Surface Science*, 189(1-2):31, 2002.

[217] M. Zenkiewicz. Investigation on the oxidation of surface layers of polyolefins treated with corona discharge. *Journal of Adhesion Science and Technology*, 15(1):63, 2001.

[218] A. C. Ruddy. The Effect of Atmospheric Glow Discharge (APGD) Treatment on Polyetherimide, Polybutyleneterephthalate, and Polyamides. *Journal of Plastic Film and Sheeting*, 22(2):103, 2006.

[219] A. Van Deynse, P. Cools, C. Leys, N. De Geyter, and R. Morent. Surface activation of polyethylene with an argon atmospheric pressure plasma jet: Influence of applied power and flow rate. *Applied Surface Science*, 328:269, 2015.

[220] K. Kostov, T. Nishime, A. Castro, A. Toth, and L. Hein. Surface modification of polymeric materials by cold atmospheric plasma jet. *Applied Surface Science*, 314(1-4):367, 2014.

[221] J. A. Jofre-Reche, J. Pulpytel, H. Fakhouri, F. Arefi-Khonsari, and J. M. Martín-Martínez. Surface Treatment of Polydimethylsiloxane (PDMS) with Atmospheric Pressure Rotating Plasma Jet. Modeling and Optimization of the Surface Treatment Conditions. *Plasma Processes and Polymers*, 13(4):459, 2016.

[222] J. Sun and Y. Qiu. The Effects of Gas Composition on the Atmospheric Pressure Plasma Jet Modification of Polyethylene Films. *Plasma Science and Technology*, 17(5):402, 2015.

[223] G.-L. Chen, X. Zheng, J. Huang, X.-L. Si, Z.-L. Chen, F. Xue, and S. Massey. Three different low-temperature plasma-based methods for hydrophilicity improvement of polyethylene films at atmospheric pressure. *Chinese Physics B*, 22(11):115206, 2013.

[224] U. Lommatzsch, D. Pasedag, A. Baalmann, G. Ellinghorst, and H. E. Wagner. Atmospheric pressure plasma jet treatment of polyethylene surfaces for adhesion improvement. *Plasma Processes and Polymers*, 4(SUPPL.1):1041, 2007.

[225] K. Niemi, V. Schulz-von der Gathen, and H. F. Dobele. Absolute atomic oxygen density measurements by two-photon absorption laser-induced fluorescence spectroscopy in an RF-excited atmospheric pressure plasma jet. *Plasma Sources Science and Technology*, 14(2):375, 2005.

[226] N. Knake, K. Niemi, S. Reuter, V. Schulz-von der Gathen, and J. Winter. Absolute atomic oxygen density profiles in the discharge core of a microscale atmospheric pressure plasma jet. *Applied Physics Letters*, 93(13):131503, 2008.

[227] D. K. Owens and R. C. Wendt. Estimation of the surface free energy of polymers. *Journal of Applied Polymer Science*, 13(8):1741, 1969.

[228] J. Coates. *Encyclopedia of Analytical Chemistry*. John Wiley & Sons, Ltd, Chichester, UK, 2006.

[229] G. P. Moss, P. S. Smith, and D. Tavernier. Glossary of class names of organic compounds and reactivity intermediates based on structure (IUPAC Recommendations 1995). *Pure and Applied Chemistry*, 67(8-9):1307, 1995.

[230] J. Deruiter. Amides and related functional groups, 2005.

[231] J. S. Sousa, K. Niemi, L. J. Cox, Q. T. Algwari, T. Gans, and D. O'Connell. Cold atmospheric pressure plasma jets as sources of singlet delta oxygen for biomedical applications. *Journal of Applied Physics*, 109(12):123302, 2011.

[232] D. Ellerweg, J. Benedikt, A. von Keudell, N. Knake, and V. Schulz-von der Gathen. Characterization of the effluent of a He/O 2 microscale atmospheric pressure plasma jet by quantitative molecular beam mass spectrometry. *New Journal of Physics*, 12(1):013021, 2010.

[233] R. Dorai and M. J. Kushner. A model for plasma modification of polypropylene using atmospheric pressure discharges. *Journal of Physics D: Applied Physics*, 36(6):666, 2003.